Ultrafast Desorption by Impulsive Vibrational Excitation (DIVE): Applications in Laser Surgery, Mass Spectrometry and Towards Ultimate Limits in Biodiagnosis

Dissertation with the aim of achieving a doctoral degree
at the Faculty of Mathematics, Informatics and Natural Sciences
Department of Physics
of Universität Hamburg
submitted by Ling Ren
2015 in Hamburg

Hiermit erkäre ich an Eides statt, dass ich die vorliegende Dissertationsschrift selbst verfasst und keine anderen als die angegebenen Quellen und Hilfsmittel benutzt habe.

I hereby declare, on oath, that I have written the present dissertation by my own and have not used other than the acknowledged resources and aids.

Hamburg, 7th July 2015   _____

The date of the oral doctoral defense: 29 June 2015

The following evaluators recommend the acceptance of the dissertation:
Prof. Dr. R. J. Dwayne Miller
Prof. Dr. Franz X. Kärtner

Zusammenfassung

Die Weiterentwicklung minimal-invasiver chirurgischer Eingriffe, räumlich aufgelöster Massenspektrometrie und von Bioanalysen mit hohem Durchsatz, bedürfen neuartiger Methoden um Gewebe zu schneiden und zur Extraktion von biologischen Molekülen ohne Veränderung der molekularen Struktur. In dieser Arbeit wird ein lasergestützer Ablationsprozess verwandt, der in der Lage ist präzise Gewebeschnitte mit minimalem Kollateralschaden auszuführen und außerdem biologische Komplexe unter Erhalt der biologischen Funktionalität aus dem Gewebe extrahiert. Die Methode basiert auf dem erst kürzlich entwickelten Picosekunden Infrarotlaser (PIRL). Dieser ist speziell dazu entwickelt worden um selektiv die Vibrationsmoden von Wasser anzuregen und dabei die Bedingung von ultraschneller Desorption durch stoßartige Vibrationsanregung (DIVE) zu erfüllen. Die grundlegende Funktionsweise ist, dass die selektiv angeregten Wassermoleküle als Treibmittel dienen um ganze biologische Strukturen aus der Oberfläche herauszulösen. Der Extraktionsprozess verläuft dabei schneller als alle thermischen schädlichen Effekte oder Fragmentation welche die Eigenschaften der Moleküle verändern würden.

Die Ablation unter der DIVE Bedingung wird erstmals auf sechs verschiedene Gewebe des Auges angewandt und erzielt dabei präzise, gut kontrollierbare, reproduzierbare und minimal-invasive Schnitte. Unter anderem konnte die berührungslose und aplanationsfreie Hornhauttrepanation gezeigt werden. Massenspektrometrie und andere analytische Methoden zeigen, dass eine große Anzahl von Proteinen unterschiedlichster molekularer Massen durch die PIRL Ablation aus dem Gewebe extrahiert wird und dass diese Proteine in der Ablationswolke weder durch Fragmentation noch durch andere chemische Prozesse verändert sind. Mit unterschichten Mikroskopie- und biochemischen Analysemethoden wird gezeigt, dass nanoskalige Einzelmolekülproteine, Viren und Zellen in der Ablationswolke morphologisch und funktional identisch mit ihren Kontrollproben sind.

Die PIRL Ablation eröffnet neue Wege für die Laserbehandlung in der Ophtamologie und kann dazu verwendet werden die chemische Aktivität *in situ* und *in vivo* zu erfassen. Das wichtigste Ergebnis ist die zerstörungsfreie Extraktion von biologischen Komplexen, was eine räumliche kompositorische Rekonstruktion ermöglicht, die nur durch die Größe des Laserfokusses begrenzt ist. Dies bietet enorme Entwicklungsmöglichkeiten für schnelle Hochdurchsatz-Biodiagnosen.

Abstract

The prospects for minimally invasive surgery, spatial imaging with mass spectrometry and rapid high throughput biodiagnosis require new means of tissue incision and biomolecule extraction with conserved molecular structure. Towards this aim, a laser ablation process is utilized in this dissertation, which is capable of performing precise tissue incision with minimal collateral damage and extracting intact biological entities with conserved biological functions. The method is based on the recently developed Picosecond Infrared Laser (PIRL) designed to excite selectively the water vibrational modes under the condition of ultrafast Desorption by Impulsive Vibrational Excitation (DIVE). The basic concept is that the selectively excited water molecules act as propellant to ablate whole biological complexes into the plume, faster than any thermal deleterious effect or fragmentation that would mask molecular identities.

The PIRL ablation under DIVE condition is applied for the first time to six types of ocular tissues, rendering precise and minimally invasive incisions in a well-controlled and reproducible way. An eminent demonstration is the contact-free and applanation-free corneal trephination with the PIRL. Mass spectrometry and other analytical techniques show that great abundance of proteins with various molecular weights are extracted from the tissue by the PIRL ablation, and that fragmentation or other chemical alternation does not occur to the proteins in the ablation plume. With various microscope imaging and biochemical analysis methods, nano-scale single protein molecules, viruses and cells in the ablation plume are found to be morphologically and functionally identical to their corresponding controls.

The PIRL ablation provides a new means to push the frontiers of laser surgery in ophthalmology and can be applied to resolve chemical activities *in situ* and *in vivo*. The most important finding is the conserved nature of the extracted biological entities, rendering compositional reconstruction possible at the spatial limit of the laser focus, which has conspicuous potential in advancing rapid high-throughput biodiagnosis.

Contents

1 Introduction

1.1 The DIVE principle

Water, the hub of life, the driver of nature (Albert Szent-Gyorgyi). *Life is water dancing to the tunes of solids* (Leonado da Vinci). The unique properties of water, essential to sustain life, have been fascinating research through the ages. Amongst its many features of dynamics, water possesses one especially interesting peculiarity, the ultrafast relaxation of the vibrationally excited stretching mode of the hydrogen-oxygen bond at the wave number of $3400\,\mathrm{cm}^{-1}$ [1, 2]. This intrinsic physical phenomenon has led to investigations on the condition of ultrafast Desorption by Impulsive Vibrational Excitation (DIVE) [3, 4] in recent years. The theoretical foundation of the studies in this dissertation is the DIVE condition. Thorough assays on the DIVE condition can be found in the studies of Cowan, Franjic, and colleagues [2, 3, 4]. The following is an overview of the DIVE principle. More specific background knowledge is provided in the subsequent chapters, corresponding to the different application scenarios of the DIVE principle therein.

The energy of the vibrationally excited stretching mode of the OH bond is redistributed to the intermolecular librations of the hydrogen bond network within $200\,\mathrm{fs}$. The thermalization of individual vibrational excitation is completed within $1\,\mathrm{ps}$. This ultrafast relaxation can be exploited to transfer optical energy to heat. That is, a mid-infrared laser pulse could be carefully selected to excite the vibrational stretching mode of the OH bond. After the ultrafast transition from optical energy to heat, thermally induced phase transitions of water molecules occur, which leads to desorption, in other words ablation. As the primary component in biological systems, liquid water has the fastest vibrational relaxation dynamics due to strong vibrational-librational coupling, and very high density of low frequency modes in the hydrogen bond networks [2, 5, 6]. The large infrared absorption coefficient of liquid water leads to the absorption of the incident optical energy within several micrometers at the wave number of $3400\,\mathrm{cm}^{-1}$. This fact eliminates scattering, in that the absorption length is

comparable to the wavelength and that the incident radiation is absorbed in the same volume as the one excited. As the backbone molecule, water is the most important target for the DIVE principle.

The wavelength and the pulse duration are the most crucial parameters of the laser pulse as the means of vibrational excitation. The wavelength of the laser pulse should be chosen such that the corresponding wave number targets the absorption peak of the OH stretching mode at $3400\,\mathrm{cm}^{-1}$ or its vicinity. The duration of the laser pulse should be on the order of ten to a few hundred picoseconds, in order to satisfy two criteria. Firstly, the duration of the laser pulse should allow complete thermalization of individual vibrational excitation of the OH stretching mode, which takes $1\,\mathrm{ps}$ at room temperature, or a few picoseconds at higher temperatures. If the laser pulse is too short to permit this complete thermalization process, a series of further excitations would take place, including vibrational ladder climbing, occurrence of highly excited vibrational overtones, localized coherent motions of atomic nuclei, and eventually breaking of weaker molecular bonds [7]. Therefore, it is necessary to choose a duration of the laser pulse longer than a few picoseconds in order to avoid deleterious bond-breaking of fragile biological molecules and undesirable molecular perturbations caused by additional nonlinear effects. Secondly, the duration of the laser pulse should be shorter than the thermal and acoustic relaxation time spans of the excited volume, several microseconds and approximately $1\,\mathrm{ns}$, respectively. Otherwise, the thermoelastic stress field would not be confined, and the thermal and acoustic transients would leak out of the excited volume, rendering thermal and shock wave damage to the collateral region.

If the two criteria for the pulse duration are met, together with heterogeneous distribution of vibrational chromophores, microscopic stress confinement in the excited volume induces the spread of thermoelastic energy into a broadband acoustic spectrum containing high frequencies. The acoustic transients, especially those of high frequencies, are strongly localized due to strong attenuation during the propagation outward. Positive and negative spikes of stress, of large amplitudes, render strong photomechanical effects under moderate laser energy. The negative tensile stress in the incident volume leads to fractures therein, and the ablation plume is released through the front surface. The process is made to occur faster than nucleation growth to keep nucleation sizes to a few molecules or nano-scale volumes, in order to eliminate cavitation induced shock waves and associated damage to adjacent tissue or regions. Therefore, ablation is achieved in the DIVE process with the most efficient coupling of optical energy to translation motions. Energy loss is avoided in the

absence of thermal and acoustic transients leaking out of the excited volume, interactions between laser pulse and ablation plume, and evaporative surface cooling. At the same time, the occurrence of highly excited intramolecular vibrational or electronic states is also eliminated.

In the DIVE process, the water molecules undergo a direct transition from the condensed phase to the gas phase, and thus act as propellant for their surrounding biological complexes in biological systems. As a well confined process with minimal shock wave damage and thermal degradation outside of the incident volume, the DIVE principle introduces a laser based ablation mechanism, where the biological complexes are ablated in an intact manner and the procedure is minimally invasive to the surrounding tissue [8]. As a practical approach, Picosecond Infrared Lasers (PIRL) are utilized to realize the DIVE principle. The radiation of PIRL at the wavelength of $3\,\mu m$ renders an absorption coefficient of $11\,394\,cm^{-1}$ [9, 10] and is thus efficiently absorbed within the first few micrometers of the incident volume. This absorption depth is comparable to the thickness of a single cell. Thus, it is possible to laterally and longitudinally confine the absorbed laser energy to remove a single cell - the fundamental (single cell) limit to surgery. The pulse durations of the PIRL models are on the order of ten to a few hundred picoseconds, sufficient to fulfill the DIVE condition. The PIRL has recently been successfully applied as a scalpel to numerous surgical scenarios, including phonomicrosurgery [11], laryngeal surgery [12, 13], porcine skin [14], chicken humeral cortex [15], porcine and human corneas [16, 17] and other ocular tissues (elaborated in Chap. 2), demonstrating minimal collateral tissue damage and most importantly the absence of scar tissue formation [8].

1.2 Comparison with other laser-tissue interaction mechanisms

Various types of lasers have been utilized to interact with biological systems, tissues being the target in most cases. Mainly five types of laser-tissue interactions are categorized according to Niemz [18] and the references therein, namely photochemical interactions, thermal interactions, ultraviolet light (UV)-induced photoablation, plasma-induced ablation and photodisruption [18]. The exposure time can serve as a rough distinguishing factor amongst the interaction mechanisms [18], as shown in Fig. 1.1. If a more sophisticated depiction of the categorized interaction mechanisms is desired, a modified Boulnois [19] diagram [18] can be employed, which incorperates parameters such as the optical

power density and the exposure time. In order to differentiate and understand the DIVE process better, a comparison between the PIRL ablation employing the DIVE principle and the other types of laser-tissue interaction mechanisms is presented in the following paragraphs.
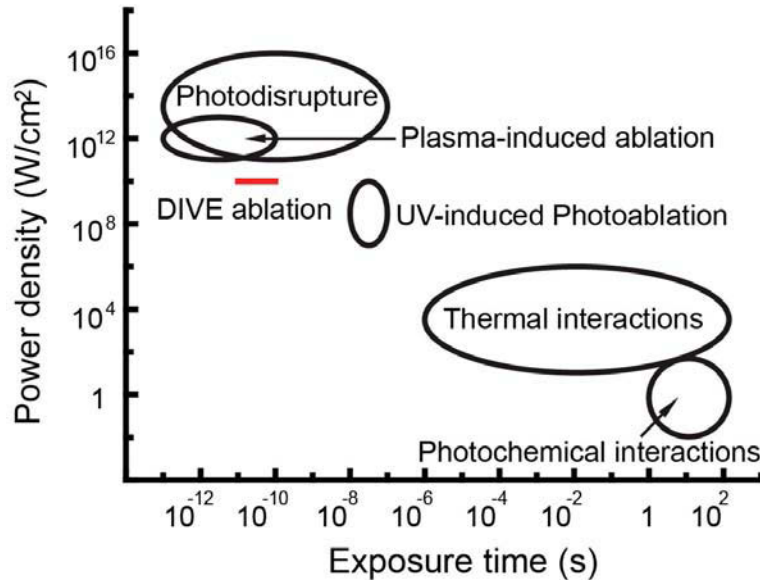

Figure 1.1: Laser-tissue interaction mechanisms categorized according to Ref. [18]. The exposure time serves as a rough distinguishing factor amongst the interaction mechanisms. The red solid line represents the DIVE process as a comparison to the established interaction mechanisms.

Photochemical interactions

Most photochemical interaction mechanisms comprise chemical effects and reactions, which are induced by lasers with wavelengths in the visible range [18]. Injection of chromophores into tissues is required in certain scenarios, in order to catalyze the reactions of macromolecules or tissues to the laser radiation. An example is the photodynamic therapy to treat cancer [20], where a photosensitizer such as hematoporphyrin derivative is injected into the patient and cytotoxic transfer reactions are induced by the laser light. Consequently, necrosis occurs in the tumor cells where the photosensitizer accumulates, and the tumor cells are specifically treated. No tissue removal is observed macroscopically during photochemical interactions. In this type of interaction mechanism, the optical power densities are very low, typically around $1\,\mathrm{W\,cm^{-2}}$, and the exposure can be delivered by continuous wave or pulsed lasers with a pulse duration of at least $1\,\mathrm{s}$. The long exposure time ensures sufficient bleaching of

4

the photosensitizers [21]. The most significant differences between the PIRL ablation under DIVE condition and the photochemical interactions are the necessity of catalyzer, exposure times, and interaction mechanisms. The lasers employed in the two interaction mechanisms also differ in wavelengths and optical power densities.

Thermal interactions

Thermal interactions utilize the heat produced by the laser radiation to achieve temperature dependent effects on tissues, such as coagulation starting at $60\,°C$, vaporization at $100\,°C$, carbonization above $100\,°C$, and melting above $300\,°C$ [18, 19]. Both continuous wave and pulsed lasers are employed, including carbon dioxide (CO_2) and Er:YAG lasers, with power densities between $10\,W\,cm^{-2}$ and $10^6\,W\,cm^{-2}$. In order to produce the desired thermal effects, pulse durations between $1\,\mu s$ and $1\,ms$ are usually chosen for pulsed lasers. The intense heat present in thermal interactions often causes collateral tissue damage, induces overt scar formation, and limits the precision of tissue removal [3]. The output wavelength of Er:YAG lasers at $2.94\,\mu m$ resides in the vicinity of the absorption peak of water at approximately $3\,\mu m$ and thus excites the vibrational modes of the OH bond as well. However, the tissue removal originated from Er:YAG laser radiation is different from that generated by the PIRL ablation under DIVE condition. The differences are elaborated as follows based on the works of Franjic *et al.* [3] and Niemz [18]. The thermal relaxation time of the excited microliter volumes of water is on the order of several microseconds [4]. When the pulse duration is longer than several microseconds, the absorbed energy dissipates into heat and leaks out of the excited volume [9]. Even when the pulse duration is compressed to $10\,ns$, thermal confinement is achieved in the excited volume but stress confinement is still absent [4, 9]. On the contrary, the PIRL ablation under DIVE condition removes the excited volume of tissue with both thermal and stress confinement, again most importantly on time scales too short to allow nucleation growth and associated cavitation induced shock waves. The whole process of ablation into the gas phase can be made to occur faster than even collisional exchange of the excited hot water molecules with the constituent proteins of the target tissue. This latter feature enables the dissection of biological agents with completely intact functions as will be illustrated in this dissertation.

UV-induced photoablation

Absorption of photons with high energies ($E \geq 3.1\ eV$) in the UV wavelength range induces direct molecular bond cleavages, accompanied with heat generation, weakening and fracturing the targeted tissue [9]. Excimer lasers are frequently employed to perform this photo-chemically driven ablation process. An example is the ArF Excimer laser emitting at the wavelength of $193\,\mathrm{nm}$ to remove corneal tissue during refractive sugeries, where the chemical bonds of corneal collagen, namely the peptide bonds (O=C-N-H), are directly cleaved [9]. This example also shines light on the characteristic dissociation mechanism of the UV-induced photoablation, which is the tissue decomposition through molecular bond breaking [18]. Typical pulse durations and power densities are $10\,\mathrm{ns}$ to $100\,\mathrm{ns}$ and $10^7\,\mathrm{W\,cm^{-2}}$ to $10^{10}\,\mathrm{W\,cm^{-2}}$, respectively [18]. The differences between the UV-induced photoablation and the PIRL ablation under DIVE condition include the dissociation mechanisms, the wavelengths, and the pulse durations. Although the UV-induced photoablation excises tissues neatly and precisely without apparent thermal damage, several adverse effects should be considered in this laser-tissue interaction mechanism. When the ArF Excimer laser is utilized above its ablation threshold, the recoil of the ablation products generates stress transients beyond the stress confinement, which lead to subtle forms of collateral tissue damage [9]. In addition, since DNA strongly absorbs the UV radiation, mutagenic effects could occur, which includes dimer formation of DNA pyrimidine bases [18].

Plasma-induced ablation

At optical power densities between $10^{11}\,\mathrm{W\,cm^{-2}}$ and $10^{13}\,\mathrm{W\,cm^{-2}}$, the strong electric field of the laser radiation leads to ionization of molecules and atoms, and then to the optical breakdown in the tissue [18]. The plasma ionization is the primary cause and intrinsic feature of this type of tissue ablation. The plasma significantly increases absorption of the incident light. Hence, lasers with wavelengths off the absorption peaks of tissues can still be utilized, such as Nd:YAG, Nd:YLF and Ti:Sapphire lasers, as long as the optical power densities suffice for plasma generation. The typical pulse duration ranges from $100\,\mathrm{fs}$ to $500\,\mathrm{ps}$. The plasma-induced ablation renders precise incisions with minimal thermal damage to collateral tissues. However, the free electrons of high densities e.g. $10^{21}\,\mathrm{cm^{-3}}$, generated in the plasma ionization, can lead to cumulative chemical damage [22]. During plasma generation, transient molecular species are created, free but toxic radicals are formed, and thus neighboring

cells can suffer from biochemical damage [9]. Therefore, despite the structural neatness of the ablation site, the biochemical pathways of cells are demolished and the healing time is prolonged [23]. The plasma-induced ablation differs from the PIRL ablation under DIVE condition in the dissociation mechanisms, the optical power densities, and the wavelengths. There are two fundamental differences regarding the dissociation mechanisms, the pathway of energy conversion, and the homogeneity of stress field [3]. The photon energy from the PIRL is directly utilized to generate mechanical freedom and lattice motions in the incident volume. As a result, the DIVE-driven ablation is a highly efficient process and the ablated biological entities remain intact. In the plasma-induced ablation, the photon energy is indirectly used to achieve mechanical effects that lead to ablation, which involves first the creation of free electrons via ionization and then the recombination and inelastic scattering of these free electrons. The initial stress field is inhomogeneous in the DIVE-driven process owing to non-uniformly distributed vibrational chromophores and microscopic stress confinement, but homogeneous in the plasma-induced ablation due to optical breakdown being rather uniform in tissues. The inhomogeneity of the initial stress field during the PIRL ablation also contributes to the high efficiency of the DIVE-driven photomechanical process under stress confinement [3].

Photodisrupture

When the optical power density is increased beyond 10^{13} W cm^{-2}, plasma generation and optical breakdown still occur, but mechanical effects consisting of shock waves, cavitation, and jet formation start to exert major impact and dominate the fragmentation and disruption of tissues. The requirement of high optical power densities reaching 10^{16} W cm^{-2} necessitates solid-state lasers like those employed in the plasma-induced ablations, with pulse durations ranging from 100 fs to 100 ns [18]. Due to the occurrence of plasma generation and optical breakdown, the photodisrupture inherits from the plasma-induced ablation the adverse effects originating from ionization and the corresponding differences to the PIRL ablation under DIVE condition, as well. In addition, shock waves and cavitation effects in the photodisrupture are not localized in the incident volume, but diffuse into collateral tissues [18]. This is again in stark contrast to the situation in the PIRL ablation under DIVE condition, where the acoustic transients are strongly localized in the incident volume.

Summary of laser-tissue interaction mechanisms

Compared to the five well-established types of laser-tissue interaction mechanisms, the DIVE-driven ablation is a unique process, realized by the PIRL with the wavelength of $3\,\mu m$ and the pulse duration on the order of ten to a few hundred picoseconds. Exciting the vibrational stretching mode of the OH bond at the wave number of $3400\,cm^{-1}$, the DIVE-driven ablation process efficiently utilizes the deposited energy with the low ablation threshold of approximately $1\,J\,cm^{-2}$ [3, 4] for the tissue types and other biological samples mentioned in this dissertation. The excited vibrational modes effectively couple the energy directly to translation motions at the fastest possible time scales, i.e. the half period of the O-O acoustic translational liquid modes of water [2, 24]. This excitation process effectively directly couples the absorbed energy into the very translational motions required for material removal. The minimized optical energy density from the PIRL directly induces a mechanical desorption, while thermal and stress confinement is maintained. With the selective excitation of the OH bond, the DIVE-driven ablation imposes little damage to collateral tissues and minimizes the undesired modifications of the biological complexes [8]. Therefore, the plume compositions of the DIVE-driven ablation genuinely represent the original samples and can be directly used for analysis and diagnosis.

1.3 Structure of this dissertation

Based on the theoretical background of the DIVE principle, the following chapters are dedicated to different application scenarios of the DIVE-driven ablation in surgery, analysis and diagnosis, with a summary chapter in the end.

- **Chapter 2** describes applications of the DIVE principle in ophthalmology.

- **Chapter 3** presents the combination of the DIVE principle and mass spectrometry for proteomics research.

- **Chapter 4** elaborates on an innovative method for sample extraction under the DIVE principle for biological analysis and diagnosis.

- **Chapter 5** summarizes the studies elaborated in this dissertation and presents a scientific outlook.

2 Applications of DIVE in ophthalmology

2.1 Introduction

The eye, as sketched in Fig. 2.1, is one of the most delicate and complicated organs of humans and animals. Various laser-based therapeutic methods have been developed to treat disorders in segments of the eye, including (from the front to the rear) cornea, sclera, trabeculum, iris, lens, vitreous body, and retina. Conventional lasers are categorized according to their target segments of the eye. After the brief overview of current laser-based treatments, the applications of the DIVE principle for therapeutic purposes in ophthalmology are introduced, and the results of proof-of-principle studies are presented and discussed. A part of the results in this chapter is published in Ref. [16, 17].

2.1.1 Conventional lasers for ophthalmologic therapies

This section is structured according to different segments of the eye. Each segment of the eye is described for its characteristics first. Then conventional laser technologies, employed in clinical practice, are presented as methods to treat pathologic conditions of the corresponding eye segment. In order to provide a general overview, a table in the end of this section is compiled from the laser parameters available [18] with respect to the target ocular tissues and the types of treatment.

Cornea

The cornea is the most anterior segment of the eye, providing 70% of the total refractive power [18]. The human cornea is divided into six layers. Starting from the anterior to the posterior, there are corneal epithelium, Bowman's membrane, stroma of cornea, Dua's layer [25], Descemet's membrane, and
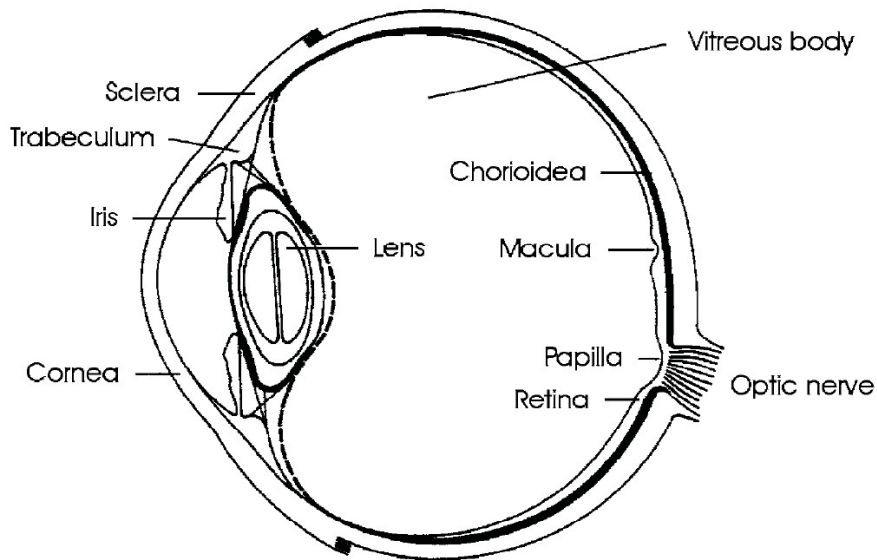
Figure 2.1: Schematic sketch of a human eye [18]. Laser-based treatments are mainly applied to cornea, sclera, trabeculum, iris, lens, vitreous body, and retina.

corneal endothelium. The corneal thickness amounts to approximately $520\,\mu m$ centrally and $650\,\mu m$ peripherally [26], $90\,\%$ of which is the stroma [18]. The largest component of cornea is water, making up $70\,\%$ to $75\,\%$ of the wet weights of the epithelium and the stroma [27].The majority of corneal solids are proteins, particularly collagens, as $70\,\%$ of the dry weight of the stroma [28], whose regular structure contributes to the transparency of cornea in the visible wavelength range.

Corneal surgeries assisted by lasers can be categorized into two groups, removal of pathologic conditions, and refractive corneal surgery [18]. One important scenario of removal of pathologic conditions in cornea is corneal transplantation, or keratoplasty, where corneal trephination can be performed by Excimer lasers or femtosecond lasers instead of traditional mechanical scalpels. Keratoplasty using ArF Excimer lasers has shown reduction in astigmatism after suture removal compared with mechanical trephination [29]. However, this technique demands the usage of inflexible metal masks, a relatively long radiation time and intensive maintenance of the Excimer laser. Keratoplasty, using femtosecond lasers emitting at the wavelength of about $1\,\mu m$, allows different profiles of trephination [30]. However, applanation, or other means of flattening or deformation of the cornea, is necessary for keratoplasty using femtosecond lasers or mechanical scalpels, which induces a horizontal torsion as an important determinant of high or irregular astigmatism [31]. In addition, the

functionality of femtosecond lasers is limited in deep layers of cornea and also in corneas that are oedematous or pathologically altered [32]. Further technical details and comparison of different laser systems for keratoplasty can be found in Sec. 2.3.1.

In refractive corneal surgeries, photorefractive keratectomy directly corrects the refractive power of the eye, where significant volumes of the cornea are ablated away by Excimer lasers. ArF Excimer lasers are commonly employed with the output wavelength of $193\,nm$, the pulse duration of $10\,ns$, and the repetition rate of $10\,Hz$. The highly localized photon-induced molecular decomposition leads to cleavages of molecular bonds at electronically excited states [33]. An ablation depth of $1\,\mu m$ at the bovine corneal tissue can be achieved with the optical energy density of $1\,J\,cm^{-2}$ [34]. Human corneas ablated by the ArF Excimer laser exhibit a smooth surface, which is sealed with a pseudomembrane between $80\,nm$ and $300\,nm$ in thickness [35] with undulating ripples no more than $1\,\mu m$ [36]. Despite the ablation precision, healing after photorefractive keratectomy is similar, or even lagging, compared with that after the surgeries performed with conventional mechanical tools [37]. During the healing process of human corneas after photorefractive keratectomy, two independent types of complications occur most frequently as hindrance, namely myopic regression and haze [38]. Myopic regression is caused by keratocyte-mediated stromal rethickening, while the corneal keratocytes are specialized fibroblasts acting in wound healing. The degree of myopic regression is proportional to the ablation depth. Haze originates from the high number of wound healing keratocytes and the increased cellular reflectivity.

Another standard technique of refractive corneal surgeries is laser-assisted in situ keratomileusis (LASIK), usually consisting of three steps [18]. First, a flap is created at the anterior part of the cornea by mechanical blades or lasers emitting at the wavelength of about $1\,\mu m$, a pulse duration between $300\,fs$ and $500\,fs$, and a pulse energy of a few microjoules. The femtosecond laser beam is focused slightly underneath the corneal surface and creates a bubble-shaped hollow spot as a result of photo damage. A continuous layer of bubbles is obtained by scanning the laser beam and leads to the flap separation [39]. In the second step of LASIK, the corneal stroma is ablated away by UV radiation. In clinical practice, the UV radiation is usually generated directly by Excimer lasers. Concerning this application scenario of Excimer lasers, the gas fill of ArF is more favorable than that of KrF or XeCl, due to the high absorbance of cornea at the wavelength of $193\,nm$ [28]. The ArF Excimer laser is advantageous in the aspects of uniform ablated edge and absent stromal melting [40]. However,

the ArF Excimer laser is noisy and maintenance intensive, employs toxic gas and produces low beam quality and stability [39]. As an alternative source of UV radiation to ablate the corneal stroma, a laser emitting at the wavelength of about $1\,\mu m$ could be converted to the fifth harmonic, approaching the wavelength of $200\,nm$. Such attempts have been reported on corneal samples in a few research laboratories. Collagen lamellas at the ablated edge are neatly cut by a quintupled picosecond Nd:YLF laser at the wavelength of $211\,nm$ [41]. Uniformly ablated edge and low thermal effects are obtained by a quintupled nanosecond Nd:YAG laser at $213\,nm$ [40, 42]. The lateral precision of $30\,\mu m$ and the surface roughness of $6\,\mu m$ are achieved by a quintupled femtosecond Yb:KGW laser at $205\,nm$ [39]. As the last step of LASIK, the flap is pulled back to the original site by surgical tweezers.

Sclera

The sclera is the opaque white protective part of the human eye, rich in fibrous bands and thus rigid [26]. In case of open-angle glaucoma [43], an incision in the sclera tissue can be considered. The aim of this surgical procedure, sclerostomy, is to improve drainage of the aqueous humor [18], reduce the intraocular pressure and mitigate the symptoms. Sclerostomy can be performed with a few different types of lasers. Since the sclera tissue does not absorb strongly in the visible and near infrared wavelength range, optical breakdown can be induced by a few hundred pulses from a nanosecond Nd:YAG laser, resulting in perforation of the sclera with collateral thermal damage of a few hundred micrometers [44]. Another possibility of laser-based sclerostomy is facilitated by visible dye lasers with the application of external inks to the sclera tissue [18].

Trabeculum

The trabeculum, or trabecular meshwork, can cause open-angle glaucoma [43] when malfunctioning. As a possibility of treatment, trabeculoplasty can be performed with an argon ion laser to shrink the trabecular meshwork and improve drainage of the aqueous humor, which is achieved with thermal interactions between approximately one hundred laser pulses and the trabecular meshwork. The focal diameter of the laser is on the order of $50\,\mu m$ to $100\,\mu m$ [18].

Iris

The iris is the tissue surrounding the pupil, consisting of collagen fibers and pigment cells. The dislocation of the iris leads to blocked drainage of the aqueous humor and thus closed-angle glaucoma [18]. Perforation of the iris, or iridotomy, can be performed with argon ion lasers for dark irises or Nd lasers for bright irises [18]. The argon ion laser is usually employed for $0.1\,\text{s}$ to $0.2\,\text{s}$, with an optical power of $700\,\text{mW}$ to $1500\,\text{mW}$ and a spot diameter of $50\,\mu\text{m}$, while a pulse energy of a few millijoules are needed from nanosecond or picosecond Nd lasers [18].

Lens

The lens, together with the cornea, achieves the refractive power of the eye, which naturally requires its transparency. Cataracts arise from the opaqueness of the lens. The treatment of cataracts involves lens fragmentation, implementation of lens replacement and removal of scattering membrane at the posterior lens capsule in case of need. Lens fragmentation can be performed with a picosecond Nd:YLF laser, and posterior capsulotomy with a nanosecond Nd:YAG laser. In both cases, the threshold of optical breakdown should be reached to avoid photo damage to the other ocular tissues [18].

Vitreous body

Since the transparent vitreous body locates directly next to the retina, it is necessary to opt for thermal interactions when lasers are utilized to remove pathologic irregularities therein [18].

Retina

As a part of the nervous system, the retina has a delicate structure and plays an essential role in vision acquisition. Lasers can be employed to treat retinal pathologic conditions, including retinal holes, retinal detachment, diabetic retinopathy, central vein occlusion, senile macula degeneration and retinal tumors [18]. Thermal interaction between the laser beam and the retinal tissue is utilized to coagulate the target areas. For example, an argon ion laser, emitting at the wavelengths of $488\,\text{nm}$ and $514\,\text{nm}$, can be applied over exposure times ranging from $0.1\,\text{s}$ to a few seconds with an optical power of $0.1\,\text{W}$ to $1\,\text{W}$ and a spot diameter of $200\,\mu\text{m}$ to $1000\,\mu\text{m}$ [18]. A krypton laser serves the coagulation purpose, with its emission wavelengths of $568\,\text{nm}$ and $647\,\text{nm}$ preferentially absorbed by different retinal components [45]. Care should be taken

to avoid undesired vaporization, carbonization and severe vision loss owing to coagulation of the macula [18].

Target ocular tissue	Treatment type	Laser type	Available laser parameters
Cornea	LASIK	ArF laser or femtosecond laser	Nd:glass laser, τ=500 fs, E_p=3 µJ
Cornea	Intrastromal ablation	Nd laser	τ=30 ps, E_p=100 µJ to 140 µJ
Cornea	Keratomileusis, photorefractive keratectomy	ArF Excimer laser	1 J cm^{-2} to 5 J cm^{-2}, 1 laser pulse removes 0.1 µm to 1 µm of tissue
Cornea	Removal of pathologic conditions	Nd lasers	τ=30 ps, $E_p \approx$50 µJ
Cornea	Removal of pathologic conditions	ArF Excimer lasers	
Sclera	Sclerostomy	Visible dye lasers	
Sclera	Sclerostomy with perforation	Nd:YAG laser	τ=12 ns, E_p=16 mJ to 53 mJ, 250 pulses to 500 pulses
Trabeculum	Trabeculoplasty	Argon ion laser	Approximately 100 pulses
Iris	Iridotomy with perforation for bright iris	Nd lasers	τ=ns or ps, E_p>a few mJ
Iris	Iridotomy with perforation for dark iris	Argon ion lasers	τ=0.1 s to 0.2 s, I=700 mW to 1500 mW
Lens	Lens fragmentation	Nd:YLF laser	τ=ps, above optical breakdown threshold
Lens	Posterior capsulotomy	Nd:YAG laser	τ=30 ns, E_p>5 mJ, more than 10^{10} W cm^{-2}
Lens & front eye segments	Surgery	Short-pulsed lasers	
Vitreous body		Thermally acting lasers	
Retina	Treatment of chorioidea	Krypton ion laser	λ=647 nm
Retina	Treatment of pigment epithelium & xanthophyll in macula	Krypton ion laser	λ=568 nm
Retina	Coagulation of retinal tissue	Argon ion laser	λ=488 nm or 514 nm, cw or τ=0.1 s to a few seconds
Retina	Welding of detached retina segments	Ruby laser	λ=694 nm, τ=1 µs to 250 µs

Table 2.1: Conventional lasers for ophthalmologic therapies, compiled from Ref. [18]. The laser parameters frequently stated are wavelength λ, pulse duration τ, pulse energy E_p, number of pulses, optical power I and optical power density.

2.1.2   DIVE for ophthalmologic applications

The PIRL ablation under DIVE condition introduces a new aspect of laser therapeutic applications in ophthalmology. Generally rich in water content, ocular tissues are suitable targets for the DIVE process. In light of its successful applications in phonomicrosurgery [11], laryngeal surgery [12, 13], porcine skin [14] and chicken humeral cortex [15], the PIRL ablation is expected to render precise incisions in ocular tissues with minimal collateral damage. Therefore, proof-of-principle studies were performed on samples of cornea, sclera, trabecular meshwork, iris, lens and retina. Emphasis is placed on cornea samples, since the PIRL ablation under DIVE condition provides a possibility of contact-free and applanation-free trephination and might broaden the armamentarium of corneal transplant surgery.

2.2   Material and methods

2.2.1   The PIRL system

A PIRL, model PIRL-HP2-1064 OPA-3000 from Attodyne Inc., Canada, was used to deliver radiation at the wavelength of 3000 ± 90 nm onto the sample, with a pulse duration of 300 ps and a repetition rate of 1 kHz. A home built optical system equipped with a scanning unit was used to deliver and focus the PIRL beam onto the sample for ablation. The scanning unit, consisting of a two-dimensional galvanometer scanner and a control program, allowed for user defined scanning speeds and ablation patterns, such as circle, line, rectangle or disk. The PIRL beam was focused onto the sample with an optical power of 460 mW. The transverse beam diameter at the focus was approximately 140 μm. The ablation was performed by applying the linear and circular scanning patterns to the sample surface. A schematic diagram and a photograph of the experimental setup of the PIRL system are shown in Fig. 2.2.
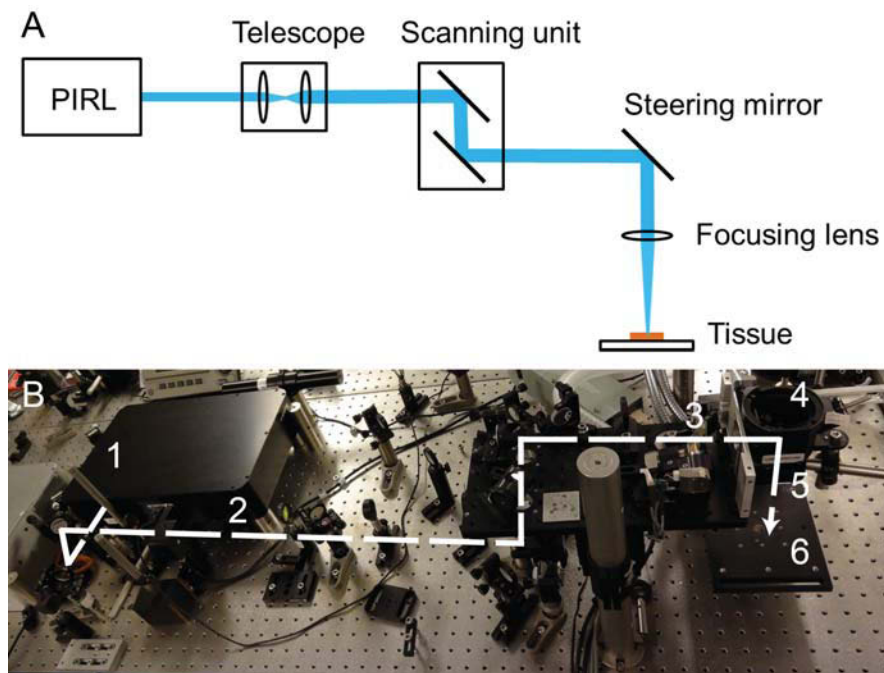
Figure 2.2: Schematic diagram of the PIRL system (A). Experimental setup of the PIRL system (B), where the white dashed line indicates the beam path from the output of the PIRL to the sample holder. Locations of the major components of the PIRL system are indicated by the numbers 1 to 6. 1: PIRL. 2: Telescope. 3: Scanning unit. 4: Steering mirror. 5: Focusing lens. 6: Tissue.

2.2.2   Ocular tissues

Freshly enucleated porcine globes were obtained from a local abattoir, kept refrigerated, and irrigated with a physiological solution. The ocular tissues were excised from the porcine eye globes and used directly in the ablation experiments. All ablation experiments and characterization measurements were performed within 36 hours of excision.

Human donor corneas unsuitable for transplantation were obtained from the eye bank of the University Medical Center Hamburg-Eppendorf (UKE). Full ethical approval was obtained and the procedures were carried out in accordance with the Declaration of Helsinki [46].

2.2.3   Characterization methods

Histology

Immediately following the ablation experiments, the corresponding tissue samples were fixed in phosphate buffered 3.5% formaldehyde. Specimens were then embedded in paraffin, cut into $4\,\mu m$ thick sections, and stained with hematoxylin and eosin (H.E., Merck, Darmstadt, Germany). Stained samples were then scanned for digitization using MIRAX SCAN (Carl Zeiss Microimaging GmbH, Jena, Germany). Microscopic width measurement and histological examination were carried out using Aperio ImageScope software (Aperio Technologies, Inc., Vista, CA, USA).

Environmental scanning electron microscopy

In order to prepare for the examination with the environmental scanning electron microscope (ESEM), the corresponding tissue samples were immersed in 1% osmium tetroxide in phosphate buffered saline (PBS) for $30\,min$ and then thoroughly washed. The hydrogenated tissue blocks were analyzed with the back scattered electron (BSE) mode of the XL30 ESEM (FEI, Hillsboro, Oregon, USA) equipped with a DISS5 digital image scanning system (Electronic Point, Halle, Germany).

Confocal laser scanning microscopy

The corresponding tissue samples were examined with a Nikon C2+ confocal laser scanning microscope (Nikon GmbH, Düsseldorf, Germany) and then analyzed with NIS-Elements v 4.20 software (Nikon GmbH).

Infrared thermography

A thermal camera (model PIR uc 180, InfraTec, Dresden, Germany) with a spectral range of $7.5\,\mu m$ to $13\,\mu m$ was used in order to avoid capturing the thermal signal of the PIRL beam at the wavelength of $3\,\mu m$. Real-time thermal images at the frame rate of $100\,frames/s$ were captured during the ablation experiments at corneas using the circular pattern. Maximal temperature within the ablation path was measured. In addition, temperatures were also measured at points 1 mm and 2 mm away from the ablation path, and at a baseline far away from the irradiated area. The data acquired were analyzed with IRBIS 3Plus software (InfraTec).

2.3   Results and discussion

2.3.1   Cornea

Imaging and histological analyses

Both linear and circular scanning patterns were applied during the PIRL ablations under DIVE condition of porcine and human cadaver corneal tissues, which rendered contact-free incisions accordingly. The linear ablations were configured with a length of $4\,\text{mm}$, a scanning speed of $120\,\text{mm}\,\text{s}^{-1}$ and a scanning repetition rate of $15\,\text{Hz}$. The scanning speed was determined according to the beam diameter of the PIRL at focus, in order to minimize spatial overlapping of consecutive pulses on the tissue and to avoid gaps between the pulses. A representative linear pattern of the PIRL ablation at corneal tissues is shown in Fig. 2.3, including a photograph and images acquired with confocal laser scanning microscope and ESEM. These images were obtained from the corneal tissues ablated by the PIRL under identical conditions. The photograph (Fig. 2.3 (A)) shows that the ablation front proceeded in a well-controlled manner parallel to the corneal surface until the cornea was penetrated, since air bubbles were observed in the anterior chamber after the Descemet's membrane was perforated.
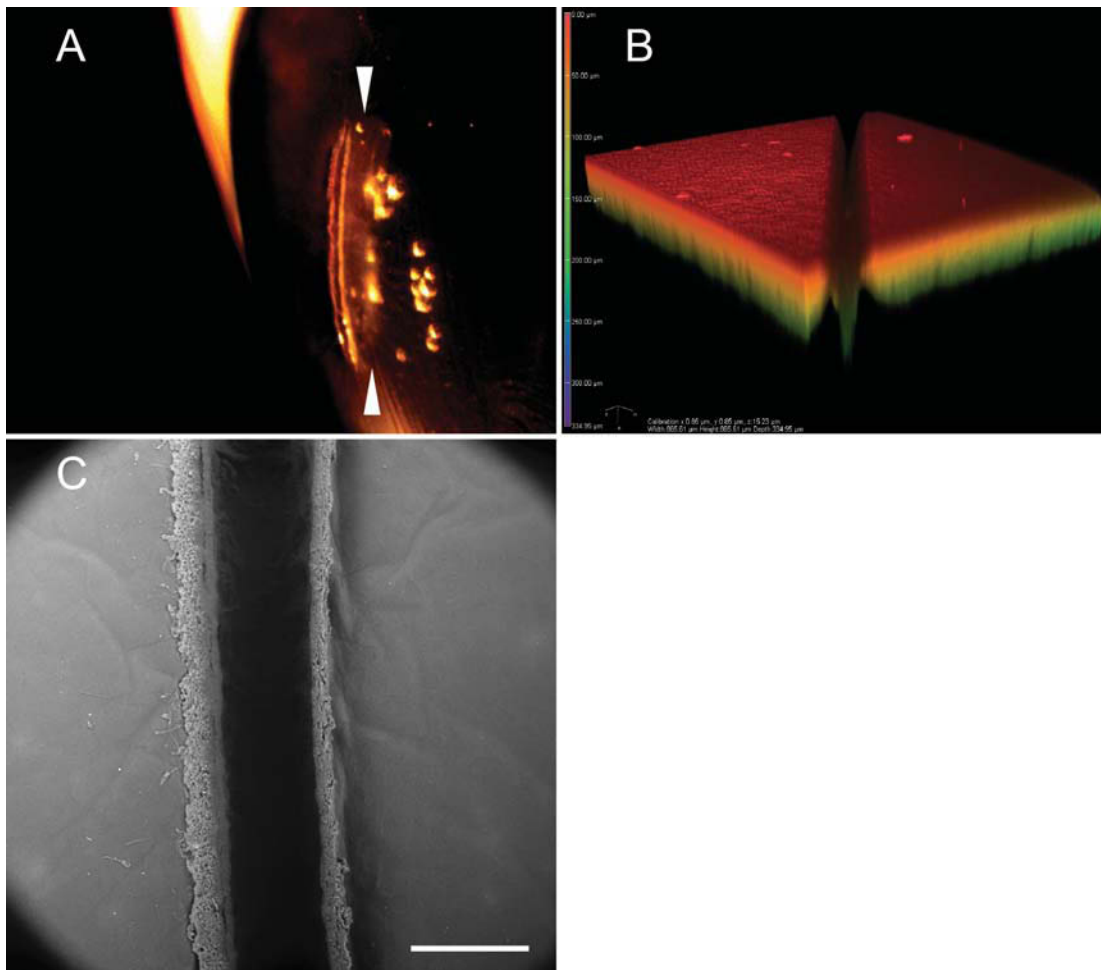
Figure 2.3: Photograph (A), confocal laser scanning microscope (B) and ESEM (C) images of linear ablation patterns at human post mortem corneal tissues performed with the PIRL. The length of the linear ablation pattern was $4\,\mathrm{mm}$. The time span of the PIRL ablation was $5\,\mathrm{s}$. The arrow heads in (A) indicate the region where the ablation front proceeded in a well-controlled manner parallel to the corneal surface. Identical PIRL ablations were applied to the corneal tissues which were analyzed afterwards with the confocal laser scanning microscope and the ESEM. The scale bar represents $300\,\mathrm{\mu m}$.

The circular ablations were configured with diameters varying between $4\,\mathrm{mm}$ and $8\,\mathrm{mm}$, in order to test the feasibility of contact-free and applanation-free corneal trephination by the PIRL ablation under DIVE condition. A representative circular pattern of the PIRL ablation at corneal tissues is shown in Fig. 2.4 including a photograph and images acquired from confocal laser scanning microscope and histological analysis. These images were obtained from the corneal tissues ablated by the PIRL under identical conditions. The images from the confocal laser scanning microscope and the ESEM confirm the preci-

sion of the deep incisions performed by the PIRL ablation at corneal tissues. Moreover, the histological analysis verifies the minimal damage to collateral tissue, as shown in Fig. 2.4 (C). No collateral damage is observed in the corneal epithelium. There is also no visible damage at the front edge of the incision, or in other words the bottom of the post-ablation opening, in the corneal stroma. The average collateral damage at the vertical edges of the post-ablation opening remains on the single cell level, and the maximum dimension of damage does not exceed $25\,\mu$m. The expansion of collateral damage resides on the same order of magnitude as previous studies on PIRL ablations of laryngeal tissues [11, 12, 13] and chicken humeral cortex [15]. The residual collateral damage can be attributed to two factors. One factor is that the PIRL beam does not have a top-hat transverse beam profile. Part of the side wings of the transverse beam profile can have the optical power below the ablation threshold of the DIVE process. Hence, this part of the optical power is insufficient to achieve ablation. Instead, it induces thermal effects in the tissue. The other factor is that the PIRL beam was focused manually onto the sample surface for ablation, since currently there is no auto-focusing mechanism available. The fact that the focusing might not remain optimal for each laser pulse during the ablation could result in minor thermal effects in the irradiated tissue. It should, however, be emphasized that the noted damage, even with present limitations in beam delivery, is still on the order of a single cell boundary and more than an order of magnitude smaller than the damage zones of conventional lasers, notably infrared lasers, used for surgery.
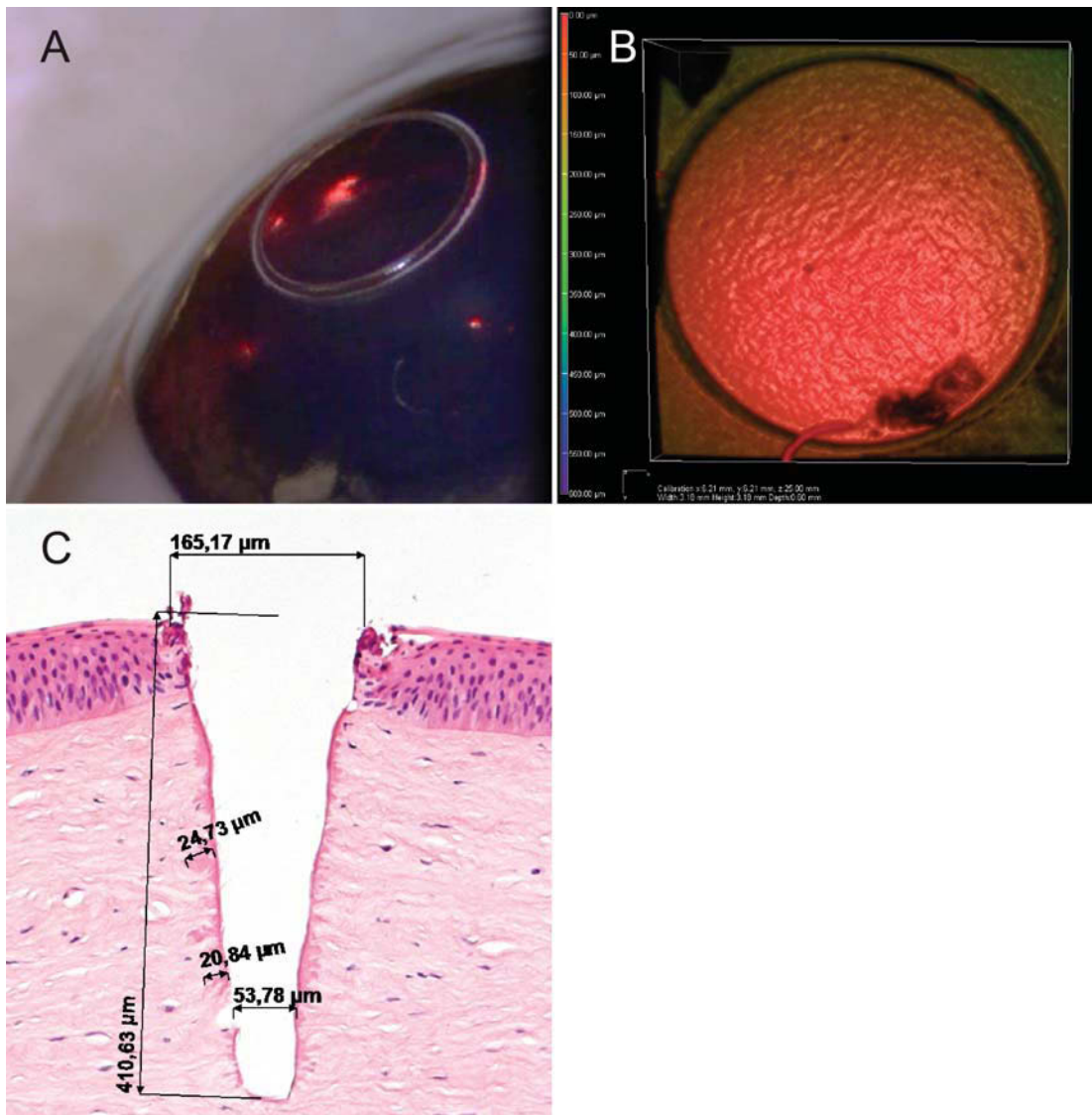
Figure 2.4: Photograph (A), confocal laser scanning microscope (B) and histological (C) images of circular ablation patterns at corneal tissues performed with the PIRL. The diameter of the circular ablation pattern was 4 mm. Identical PIRL ablations were applied to the corneal tissues which were analyzed afterwards with the confocal laser scanning microscope and the histological procedure. The artefact on the lower part of the sample in (B) was observed on the tissue before the PIRL ablation. Measurements were taken during the histological analysis (C), namely the widths of the upper and lower parts of the PIRL incision, the depth of the incision, and the dimensions of the two largest sites of collateral damage.

Tissue temperature during PIRL ablation

The infrared thermal camera was employed to measure the temperatures of the PIRL ablation sites at corneal tissues in order to acquire more thermal properties of this process. The circular ablation pattern with the diameter of $4\,\mathrm{mm}$ was applied to six porcine corneas over the ablation time spans of $2\,\mathrm{s}$, $4\,\mathrm{s}$ and $6\,\mathrm{s}$, two samples for each time span. A representative set of temperature measurements is shown in Fig. 2.5, which depicts the temperatures measured at the ablation path, $1\,\mathrm{mm}$ and $2\,\mathrm{mm}$ away from the ablation path, and the baseline, during the PIRL ablation over $6\,\mathrm{s}$. The temperature measurements were recorded over a time span long enough to include the entire ablation process as well as the subsequent stabilization. The temperature at the ablation path increased first quickly compared with the other measurement sites at the start of the ablation process, then gradually reached a plateau during the latter part of the ablation process, and then decreased swiftly when the ablation process terminated. Insignificant temperature increases, starting from $15\,\mathrm{°C}$ and reaching $20\,\mathrm{°C}$ in maximum, were also observed at the measurement sites $1\,\mathrm{mm}$ away from the ablation path. Even smaller temperature increases were observed at the measurement sites $2\,\mathrm{mm}$ away from the ablation path. After the quick post-ablation decrease, the temperature at the ablation site stabilized towards the ambient temperature. During all measurements, the maximal temperatures at the ablation sites over the ablation time spans of $2\,\mathrm{s}$, $4\,\mathrm{s}$ and $6\,\mathrm{s}$ were $33.5\,\mathrm{°C}$, $35.1\,\mathrm{°C}$ and $34.2\,\mathrm{°C}$, respectively.
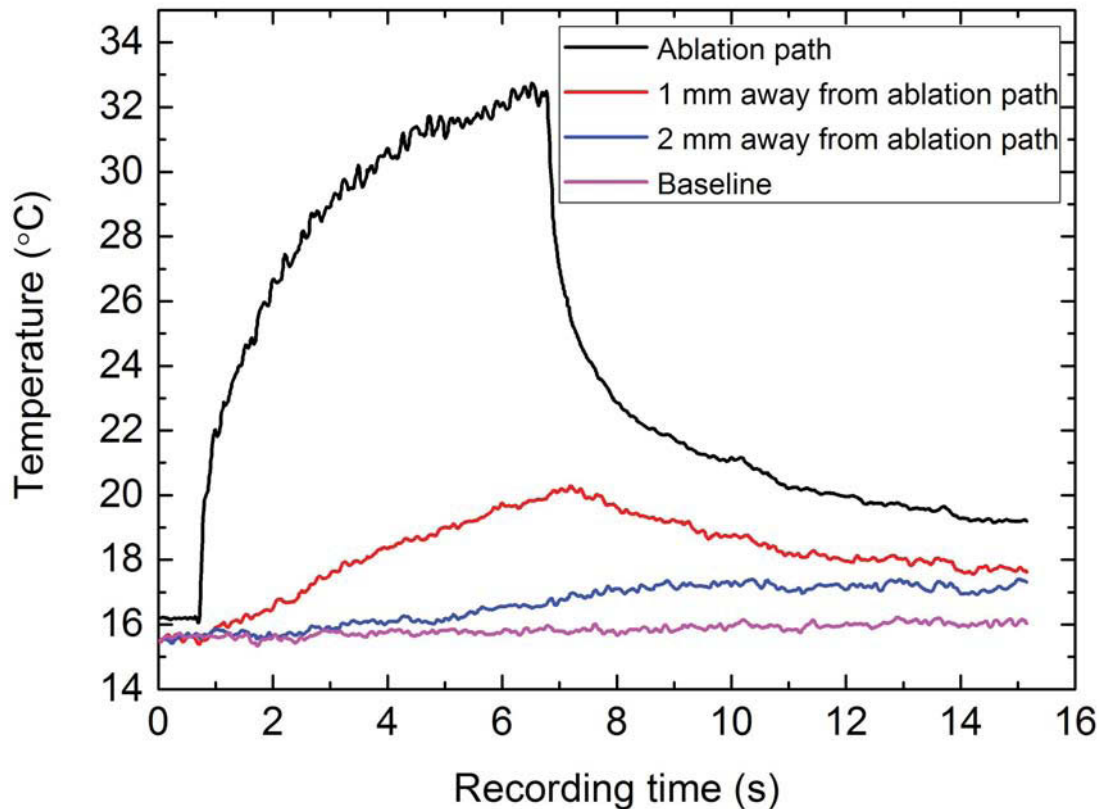
Figure 2.5: Temperature measurements with the infrared thermal camera during the PIRL ablation of porcine cornea. The diameter of the circular ablation pattern was 4 mm. The ablation time was 6 s. The temperatures measured at the ablation path, 1 mm and 2 mm away from the ablation path are depicted in black, red and blue, respectively. The baseline temperature is depicted in magenta. Five-point Fast Fourier Transform was applied to each curve for smoothing.

Although the temperature at the ablation sites increased during the PIRL ablation, it did not exceed the body temperature and remained in the physiological range, which theoretically would not lead to thermal degradation of biological complexes like proteins. Such insignificant temperature increases at the ablation sites were also reported in previous studies on PIRL ablations of laryngeal tissues [13], porcine skin [14] and chicken humeral cortex [15]. It is necessary to note that the data from the thermal camera should be interpreted with caution, as the frame rate of the thermal camera could be too low to detect fast temperature changes due to the PIRL ablation. On the other hand, the histological analysis revealed thermal effects on collateral tissues with similar appearance in all samples and at the single cell level on average. The thermal effects on collateral tissues were also independent of the ablation time and the

maximum temperature during the ablation process. An exemplary image from the histological analysis is shown in Fig. 2.4 (C). These findings indicate that the DIVE-driven ablation process does not impose a hostile environment to the tissue in the aspect of temperature, which contributes to the minimal collateral damage and the fact that the biological complexes are ablated in an intact manner.

Ablation depth with respect to ablation time

In order to further characterize the PIRL ablations of corneal tissues, the correlation between the ablation time and the ablation depth was investigated. Eight different ablation time spans, $1\,\mathrm{s}$ to $8\,\mathrm{s}$, were applied to a total of forty porcine corneas, five samples for each time span. Apart from the ablation time span, other experimental parameters were identical during the PIRL ablations and the processing of the samples, including the optical power, the linear ablation pattern measuring $4\,\mathrm{mm}$ in length, and the scanning speed. Following the PIRL ablations, the porcine corneas underwent identical histological analysis, and the depths of the incisions resulting from the PIRL ablation were measured. The average depths of the PIRL ablations with respect to the ablation time spans are summarized in Tab. 2.2 and Fig. 2.6.

Ablation time [s]	Average ablation depth [μm]	Standard deviation of the average ablation depth [μm]
1	139	15
2	215	24
3	353	32
4	404	36
5	478	51
6	567	59
7	617	30
8	652	48

Table 2.2: Average depths of the PIRL ablations under DIVE condition at porcine corneas with respect to the ablation time spans. The ablation pattern was a line measuring $4\,\mathrm{mm}$.
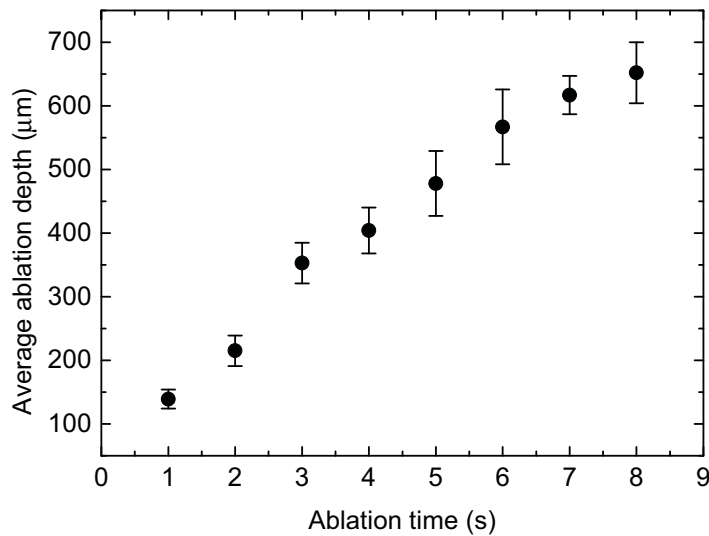
Figure 2.6: Average depths of the PIRL ablations under DIVE condition at porcine corneas with respect to the ablation time spans. The error bars represent the standard deviation corresponding to each data point. The ablation pattern was a line measuring 4 mm.

Reproducible ablation depths were obtained within a given time span of the PIRL ablation. The ablation depth increases approximately in proportion to the ablation time span. But a decreasing slope in Fig. 2.6 is observed when the ablation time reaches seven or eight seconds. Two factors are expected to attribute to the decreasing slope. One factor is that the ablation front was proceeding into the Descemet's membrane by the ablation time of seven or eight seconds. The Descemet's membrane belongs to the posterior part of the cornea and is rich in collagen, whose reduced water content renders it slightly more difficult for the DIVE process to remove than the corneal stroma. The other factor is the loss of optical power due to increased diffraction at the edges of the entry point initially cut, which led to the reductions in the light on target and in the amount of tissue ablated. The increased diffraction was explained by the absence of external tension applied onto the corneas to widen the incisions, as the PIRL beam progressed deep into the tissue.

The proportionality between the ablation depth and the ablation time span from one to six seconds provides a possibility of further analysis of this ablation process at the cornea. Linear fitting was applied to the data points with the ablation time spans between one and six seconds. The slope of the linear fitting was used to calculate the ablation depth of each PIRL pulse. A simple

model incorporating Beer-Lambert's Law illustrates the relationship between the ablation depth D of a single pulse, the tissue absorption coefficient α, the absorbed fluence F_a and the threshold fluence F_{th} [47, 48, 49].

$$D = \frac{1}{\alpha} \ln(\frac{F_a}{F_{th}}) \qquad (2.1)$$

The absorption coefficient of cornea in the mid-infrared range is depicted in Ref. [50]. According to Eq. 2.1, the absorbed fluence was estimated as 1.1 times of the threshold fluence during this ablation process. This estimation is coherent with the experimental results, in light of the successful PIRL ablations at the cornea.

Another observation from Tab. 2.2 and Fig. 2.6 is that the standard deviation of the average ablation depth is approximately $10\,\%$ of the corresponding average ablation depth for the ablation time of $1\,\text{s}$ to $6\,\text{s}$, and less than $10\,\%$ for longer ablation time spans. This investigation on the ablation depth with respect to the ablation time establishes the PIRL ablation under DIVE condition as a reliable and reproducible method for corneal incisions. In the aforementioned scope of ablation parameters, the tissue volume ablated per unit time is stable and the amount of tissue removal can be controlled by the user-defined ablation time.

Suitability to PIRL ablation

Water and collagen are the two dominating components of soft tissues by mass and also the most abundant chromophores in such tissues in the infrared spectral region [9]. The vibrational modes of water and collagen dominate the absorption spectra. Water has two significant absorption peaks at the wavelengths of $2.9\,\mu\text{m}$ and $6.1\,\mu\text{m}$ [10, 51]. Collagen also has two important absorption peaks at the wavelengths of $6.1\,\mu\text{m}$ for the amide I-band and $6.4\,\mu\text{m}$ for the amide II-band of collagen [9]. As a typical "extracellular matrix-continuous" soft tissue, the cornea has collagen fibrils as the main mesoscopic structural element [9], whose regular size and spacing contribute to the cornea's optical transparency at the visible wavelength range [26]. Due to the abundance of water therein, the cornea is a suitable target for the DIVE process. Based on the above proof-of-principle studies, the PIRL ablation under DIVE condition serves as a reliable and reproducible method to perform contact-free and applanation-free linear incisions and trephinations at the cornea with minimal collateral damage.

Comparison to preceding laser therapeutic methods

ArF Excimer lasers and femtosecond lasers have been well established in the market for ophthalmologic applications. In order to perform corneal trephinations, it is necessary to apply an inflexible metal mask [29, 52] to the patient's eye, when the ArF Excimer laser is utilized. When the femtosecond lasers are opted for corneal trephinations, a glass lens or a standard microscope coverslip [32, 53] is used to applanate the cornea in order to facilitate this procedure. The applanation device imposes potential side effects of residual glass particles in the cornea after keratoplasty [54]. The applanation during the trephination for keratoplasty with the femtosecond lasers can result in an oval shaped recipient bed, which limits the theoretical perfect congruence of the donor and recipient [55]. The reduction of post-operative astigmatism is not confirmed for the femtosecond lasers-assisted trephination compared to the mechanical trephination [31, 55]. In comparison, the PIRL ablation performs incisions including trephination at the cornea in a contact-free and applanation-free manner, which is free from the necessity and the potential side effects of metal masks and applanation devices.

In healthy and pathological cornea and sclera, the dominating phenomenon in the tissue optics is Rayleigh scattering as a result of the interaction between the incident laser beam and the spatial distribution of the collagen fibrils [54]. An nontrivial part of the laser radiation at the wavelength of $1\,\mu m$ is scattered in oedematous cornea ($40\,\%$) and sclera, and the beam quality is significantly degraded [54]. Therefore, the femtosecond lasers currently on the market have limited surgical applications in oedematous cornea and sclera. The scattering is strongly reduced and the residual absorption dominates for the wavelength range of $1.6\,\mu m$ to $1.8\,\mu m$ [54]. Optimization of the corneal surgery is shown in Ref. [32] with a femtosecond laser at the wavelength of $1.6\,\mu m$. On the contrary, the laser radiation at the wavelength of $3\,\mu m$ is strongly absorbed in the first few micrometers of tissues, as elaborated in Chap. 1, which eliminates the problem of scattering. Hence, the PIRL ablation under DIVE condition enables penetrating incisions deep into the corneal stroma and does not present any limitation to corneal transplant surgery without applanation of the cornea. Moreover, the PIRL ablation also easily renders precise incisions at oedematous cornea, scarring cornea, and sclera, the last of which is elaborated in the following section. The characteristic technical parameters of different commercial laser systems and the PIRL system for keratoplasty are summarized in Tab. 2.3.

Laser systems	ArF Excimer	Femtosecond type 1	Femtosecond type 2	Near infrared	Mid-infrared
Manufacturer	N. A.	Abbott Medical Optics, Alcon, Bausch+Lomb, Zeiss Meditec	Ziemer	Prototype in Ref. [32]	Prototype PIRL
Wavelength [nm]	193	1050	1050	1650	3000
Repetition rate	>200 Hz	>60 kHz	10 MHz	10 kHz	1 kHz
Pulse duration	20−200 ns	200−500 fs	200−300 fs	600 fs	300 ps
Pulse energy	Approximately 1.6 mJ	Approximately 3 µJ	Approximately 5 nJ	2−20 µJ	460 µJ
Spot diameter [µm]	950	3 − 4	1 − 2	1	140
Applanation	No. Metal mask needed	Yes	Yes	Yes	No
Trephination of oedematous or scarring cornea	Yes	N.A.	Oedematous yes, scarring N.A.	Yes	Yes
References	Ref. [29]	Ref. [54, 55, 56]	Ref. [54, 56]	Ref. [32]	This work and Ref. [16, 17]

Table 2.3: Summary of characteristic technical parameters of different laser systems for keratoplasty. The Excimer and two types of femtosecond lasers are commercially available for clinical use. The enumeration of manufacturers are only meant for information purpose and not exhaustive. The near infrared laser and the PIRL are prototypes. N.A. represents information not available.

As a research facility, the free electron lasers with microsecond pulses at the wavelength range of mid- and long-infrared produce ablations of soft biological tissues including the cornea with high efficiency [57, 58] and minimal collateral damage, for example $10\,\mu m$ to $20\,\mu m$, at the wavelength of $6.0\,\mu m$ [59]. However, the free electron lasers have not been employed in clinical use, owing to their huge space consumption and immobility which are unsuitable for patient treatment. As a table top system, the PIRL consumes much less space and can in principle be further reduced in size. Even a mobile PIRL system should be possible. In addition, the long integrated macro-bunch of the free electron lasers' pulse structure represents really a microsecond excitation process under these conditions, where it is well known that unarrested nucleation growth and cavitation shock wave damage occur. PIRL's picosecond excitation process completely avoids this problem in collateral damage. Therefore, the PIRL ablation under DIVE condition has the potential for patient treatment in the operation theatre.

2.3.2 Sclera

The linear scanning pattern measuring $4\,mm$ in length was applied during the PIRL ablations under DIVE condition of porcine sclera. The incisions were performed without difficulty, although the sclera is more mechanically stable and rigid due to a higher percentage of fibrous bands therein than the cornea. Since the DIVE process does not involve molecular bond cleavage or optical breakdown, a few collagen fibrils that were not ablated away can still be observed in the ESEM image of the PIRL incision at the sclera, as shown in Fig. 2.7 (A). In a tissue rich in collagen like the sclera, the presence of the few unablated collagen fibrils at the PIRL incision indicates that the DIVE process is a gentle ablation procedure that reduces modifications of the biological complexes to the minimum. In order to selectively remove collagen, it is possible to selectively excite the collagen vibrational modes as well to soften this tissue constituent for removal as needed.

The correlation between the ablation time and the ablation depth was investigated in the PIRL ablations of porcine sclera. Five different ablation time spans, $1\,s$ to $5\,s$, were applied to a total of twenty porcine scleras, four samples for each time span. Apart from the ablation time span, other experimental parameters were identical during the PIRL ablations and the processing of the twenty porcine scleras, including the optical power, the linear ablation pattern and the scanning speed. Following the PIRL ablations, the porcine scleras underwent identical histological analysis and the depths of the incisions resulting

from the PIRL ablation were measured. The average depths of the PIRL ablations with respect to the ablation time spans are shown in Fig. 2.7 (B). Technical limitations of the histological analysis led to the fact that only one sclera sample was suitable to measure the ablation depth for the ablation time of 1 s. Thus, there is no error bar based on standard deviation available for this data point with the ablation time of 1 s. The accuracy of the measurement itself is within this point area shown. The PIRL ablation under DIVE condition renders reproducible incisions at the sclera, whose average depth is approximately proportional to the ablation time. In light of the characteristics of the DIVE process, the PIRL ablation can be utilized to perform incisions at the sclera in the operation theater, for example in sclerostomy where an incision starting from the exterior proceeding to the interior is required.
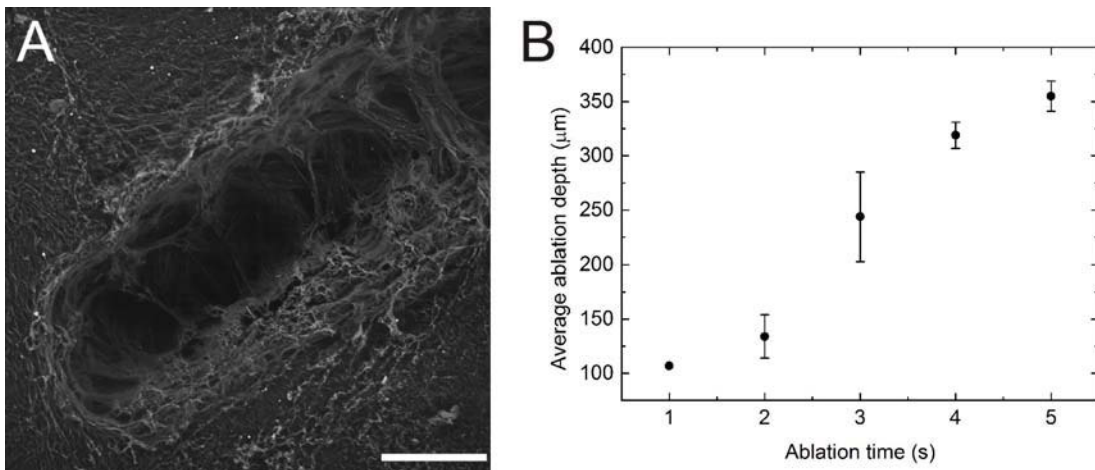
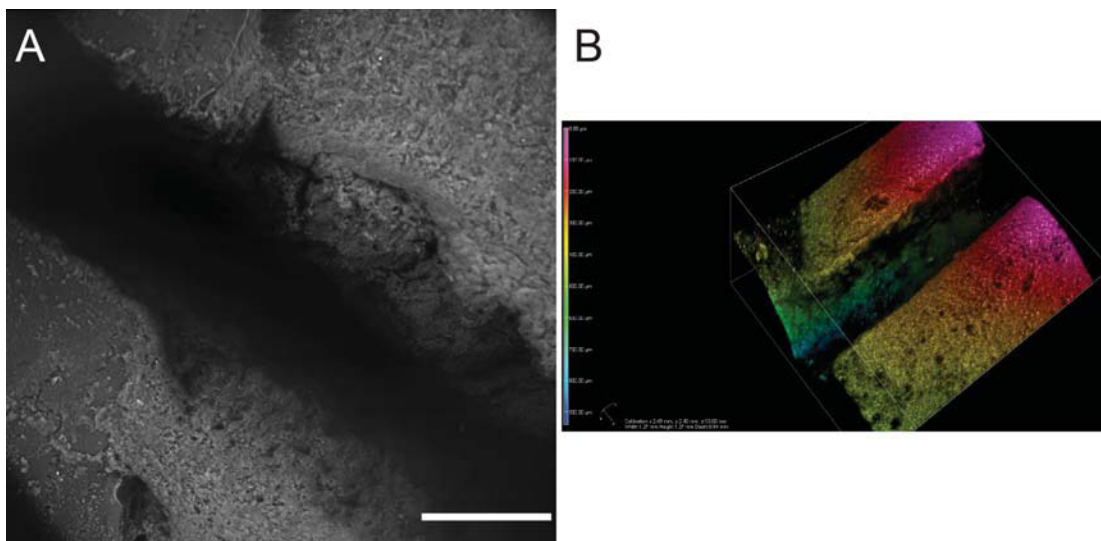**Figure 2.7:** Representative ESEM image of the PIRL ablation under DIVE condition at porcine sclera (A). Part of the linear incision with one end is shown from the top view. Collagen fibrils not ablated away were visible on the bottom of the post-ablation opening. The scale bar is 200 µm. Average depths of the PIRL ablations under DIVE condition at porcine scleras with respect to the ablation time spans (B). The error bars represent the standard deviation corresponding to each data point. The ablation pattern was a line measuring 4 mm. Four sclera samples were ablated by the PIRL for each ablation time span. Owing to technical limitations of the histological analysis, only one sclera sample was suitable to measure the ablation depth for the ablation time of 1 s, which results in the non-availability of error bar based on standard deviation for this data point. The accuracy of the measurement itself is within the point area shown.

2.3.3   Other ocular tissues

The linear scanning pattern was applied during the PIRL ablations under DIVE condition of porcine trabecular meshwork, lens, iris, and retina. The length of

the ablation pattern was $2\,mm$ at the trabecular meshwork, $2\,mm$ at the lens, $3\,mm$ at the iris, and $2\,mm$ at the retina. The ablation time was $5\,s$ for all the samples. For each type of the ocular tissues, the incisions were performed by the PIRL under identical conditions and examined with the ESEM. The confocal laser scanning microscope was employed to obtain images of the PIRL incisions at the trabecular meshwork and the lens. The incisions at the trabecular meshwork exhibit neat and precise edges, as shown in Fig. 2.8. Thus the PIRL ablation could be utilized when incisions are needed at the trabecular meshwork, which could be potentially developed to a new technique to treat open-angle glaucoma.

Figure 2.8: Representative ESEM image of the PIRL ablation under DIVE condition at porcine trabecular meshwork (A), where part of the linear incision is shown from the top view. The scale bar represents $300\,\mu m$. Representative confocal laser scanning microscope image of the PIRL ablation under DIVE condition at porcine trabecular meshwork (B), where part of the linear incision is shown from the top view.

Top views of the PIRL incisions at the lens are shown in Fig. 2.9. The two side edges, cut open by the PIRL, lead to the bottom of the incised channel in the middle of Fig. 2.9 (A). The surface of one edge and a part of the channel bottom are depicted in magenta and blue, respectively, in Fig. 2.9 (B). It is observed that the organization of the lens fibers was well preserved at the side edges and the bottom of the incised channels, which confirms the gentleness of the DIVE process. Well preserved collagen fibrils are also present at the bottom of the incised channels at the iris and the retina, as shown in Fig. 2.10. Due to the fact that the retina is on average only $0.5\,mm$ or even less in thickness [18],

the PIRL ablation with the duration of $5\,\text{s}$ penetrated the retina and proceeded into the sclera underneath.
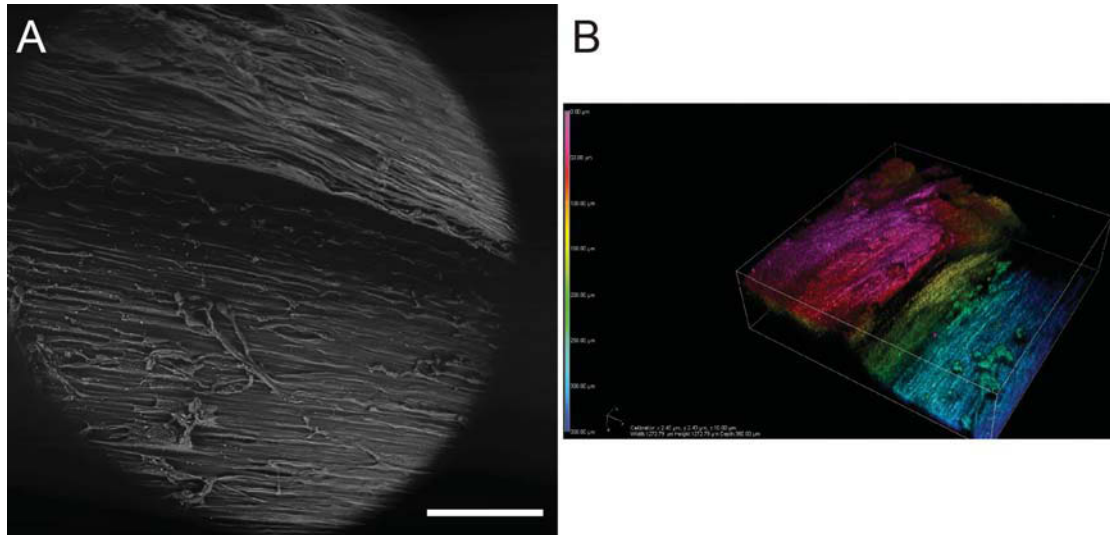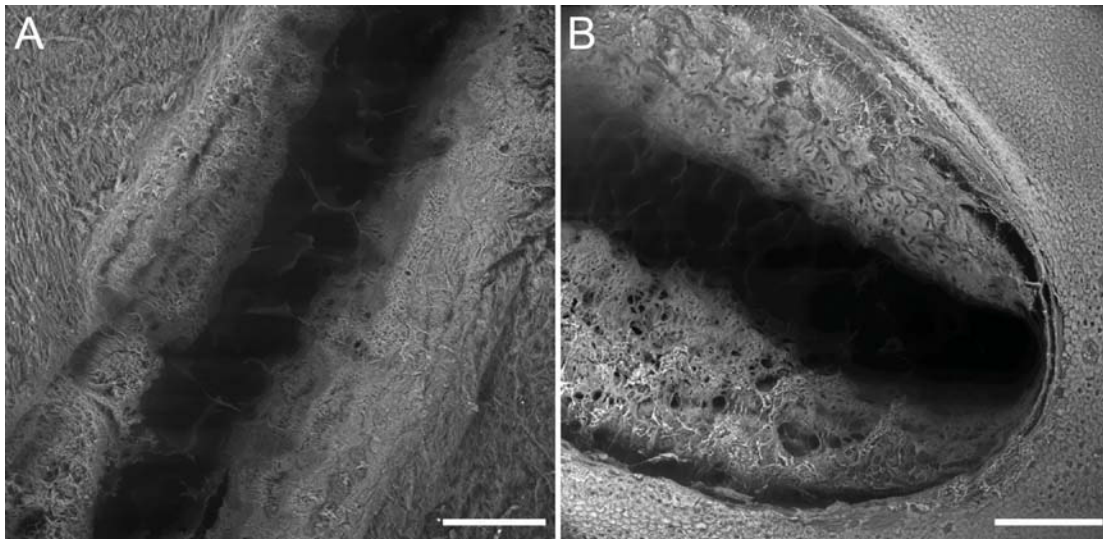

Figure 2.9: Representative ESEM image of the PIRL ablation under DIVE condition at porcine lens (A), where part of the linear incision is shown from the top view. The scale bar represents $300\,\mu\text{m}$. Representative confocal laser scanning microscope image of the PIRL ablation under DIVE condition at porcine lens (B), where part of the linear incision is shown from the top view.

Figure 2.10: Representative ESEM image of the PIRL ablation under DIVE condition at porcine iris (A), where part of the linear incision is shown from the top view. Representative ESEM image of the PIRL ablation under DIVE condition at porcine retina (B), where part of the linear incision with one end is shown from the top view. The PIRL ablation penerated the retina and proceeded into the sclera underneath. The scale bars represent $200\,\mu m$.

From the empirical point of view, there is no principal difference between the PIRL ablation under DIVE condition at the aforementioned ocular tissues and that at the cornea and the sclera. The precise and neat incisions are conspicuously observed together with minimal collateral damage in all these tissues. This is easily comprehensible, in light of the similar compositions of these soft tissues in the eye. Naturally, further investigations are necessary to characterize the PIRL ablation at these ocular tissues. As preliminary outlook on application scenarios, the PIRL ablation should not be limited to the aforementioned contact-free and applanation-free corneal keratoplasty. It could also be employed to perform incisions and excisions at the sclera, the trabecular meshwork, the lens, the iris and the retina, especially when precision and minimal collateral damage are of preeminent demand. Due to the strong absorption of the laser radiation at the wavelength of $3\,\mu m$ by tissues, when an incision is required not at the tissular surface but inside the eye globe or other organs, it is worthwhile to consider using a fiber to deliver the PIRL beam to the surgical site.

3 DIVE mass spectrometry for proteomics

3.1 Introduction

Apart from the surgical application as a laser scalpel, another substantial application scenario for the PIRL ablation resides in its combination with various analytical techniques, including but not limited to chemical analyses, mass spectrometry and biomedical microscopy, for further advancement in the corresponding fields. This chapter elaborates on pilot experiments performed to test the combination of the PIRL ablation under DIVE condition and conventional mass spectrometry techniques. The combination of the PIRL ablation, biochemical analyses and biomedical microscopy is discussed in Chap. 4. The pilot experiments in this chapter aim at answering two major questions. The first question is whether the PIRL ablation is a sample specific process to extract and introduce protein samples to analytical procedures. In other words, it is necessary to investigate the range of proteins that could be successfully extracted and introduced by the PIRL ablation for chemical analyses. The second question is whether fragmentation and other changes in the chemical and enzymatic properties would occur in the protein species ablated by the PIRL. Given that mass spectrometers were intensively utilized in the pilot experiments, a brief introduction in the following paragraphs provides a general sketch of this type of analytical apparatus with emphasis on the specific variations employed. The interested readers are referred to more thorough literature, e.g. [60], for further information. Subsequently, the pilot experiments and the results, part of which are published in Ref. [61], are presented. Based on the results, further possibilities to combine the DIVE process and mass spectrometry are discussed in the scope of current trends of research in mass spectrometry for biological samples.

3.1.1 Working principle of mass spectrometers

A mass spectrometer measures the mass of a sample more precisely than other techniques and provides information on its chemical structure [60, 62]. However, it does not directly weigh the mass of an analyte, but rather measures the mass-to-charge ratio (m/z) of a charged particle. With the number of charges known, the atomic mass could be calculated from the m/z value [60, 63]. The general working principle of a mass spectrometer is sketched in Fig. 3.1. An analyzing process of mass spectrometer typically consists of the following consecutive steps.

- The sample is introduced from gas, liquid or solid phase into the apparatus.

- Since the mass spectrometer only measures charged particles, ionization of the sample is a crucial step either in parallel to or after the sample introduction.

- The charged particles undergo specific trajectories in the electric and/or magnetic fields implemented in the mass analyzer.

- The signals generated by the detector are translated into m/z values according to the specific type of mass analyzer.

High vacuum, or very low pressure, typically 10^{-2} Pa to 10^{-5} Pa [63], is applied to the ion source, the mass analyzer and the detector in order to eliminate background molecules. Otherwise, the collision, scattering and neutralization of ions would impair the measurements, as the ions might be deflected, fragmented or eliminated [60, 63]. The results on measured m/z values are collected and compiled into mass spectra. Special attention should be paid to the interpretation of data in order to obtain credible results. For example, in the case of peptide identification, it is usually necessary to manually validate the search results by comparing the recorded mass spectra and the database, instead of blindly trusting the computer software [62]. The constituent steps of the analytical process are further described in the next paragraphs with emphasis on the techniques utilized in the experiments. For an extensive review, the interested readers are kindly referred to standard textbooks on mass spectrometry such as Ref. [60, 63, 64, 65].
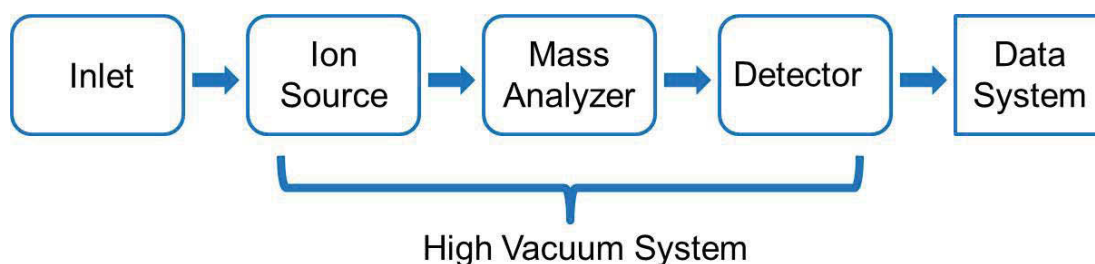
Figure 3.1: Working principle of a mass spectrometer in sketch. The arrows indicate the sequential process that an analyte undergoes through different components of the mass spectrometer.

3.1.2 Sample introduction

The inlet unit introduces analytes into the mass spectrometer. The appropriate configuration of the inlet unit is determined by the sample, together with its aggregate state and thermal chemical properties. Samples in the gas phase can be directly introduced using a direct vapor inlet or gas chromatography. Thermally labile analytes can be introduced from the condensed phase with liquid chromatography or a direct insertion probe. Direct ionization techniques are frequently employed to introduce samples of thermal instability or insignificant vapor pressure [63].

High-Performance Liquid Chromatography/Mass Spectrometry (HPLC/MS) benefits from the introduction of nonvolatile and/or polar samples [60] via liquid chromatography. In liquid chromatography, a solvent, or the mobile phase, first takes up the analyte, and then they move together through a column with packing material, or the stationary phase. Components of the analyte are separated chromatographically in the column according to their different affinities to the mobile and stationary phases [66, 67]. Interfaces for HPLC/MS commonly employ atmospheric pressure ionization, including electrospray ionization [68], as elaborated in the next paragraphs.

3.1.3 Sample ionization

Sample ionization is an essential step that transforms the analyte molecule from its neutral form to a charged form, which facilitates the analytical process by the mass spectrometer. The ionization can only be bypassed if the analyte is naturally charged, e.g. certain types of lipids [69, 70]. When an electron is removed, a cation is formed from the neutral analyte molecule; when a proton is added, an adduct ion is formed from the neutral analyte molecule and the

additional proton [63]. The analyte molecule can be multiply charged, depending on the specific ionization technique employed. Various ionization techniques have been developed, including inductively coupled plasma, electron ionization, chemical ionization, electrospray ionization, Matrix-Assisted Laser Desorption/Ionization (MALDI), fast atom bombardment, secondary ion mass spectrometry, and variations of each type. Fragmentation commonly occur depending on the ionization energy, which complicates the mass spectra but provides structural information of the analyte [63].

In inductively coupled plasma, the analyte is introduced into an argon plasma consisting of Ar^+ and free electrons in a glass torch, where the corresponding cation is produced [62].

Electron ionization is the most commonly used ionization technique for analytes in the gas phase in mass spectrometry [60]. Electrons from thermal emission are accelerated by an electric field between the cathode and the anode. The analyte molecules traveling through the ionizing electron beam are ionized when an electron is removed from the molecule, since its electron cloud is distorted by an ionizing electron passing and then the electron is ejected [63]. The cations are generated not only from the intact molecules but also from their fragments. In case of extensive ionization energy, ions from the intact molecules can be eliminated and only those from fragments are detected. Although the abundance of fragmentation provides structural information during the interpretation, electron ionization is not suitable to analyze proteins, in that this technique breaks chemical bounds and that the excessive fragmentation renders overwhelmingly complicated mass spectra [62].

In chemical ionization, reagent gas is implemented in the ionization cell which is slightly modified from that for electron ionization. The reagent gas is converted to a cloud of reagent ions by the ionizing electron beam. For positive chemical ionization, proton transfer reaction takes place between an analyte molecule and a reagent ion, resulting in an adduct analyte ion. For negative chemical ionization, electron capture reaction leads to the analyte carrying a negative charge. Little excessive energy is applied during the process of chemical ionization, rendering reduced fragmentation and intensified signals from the analyte during the measurements. Therefore, chemical ionization is termed as a "soft" ionization technique.

Due to the difference in fragmentation during the ionization process, electron ionization and chemical ionization are complementary to each other. The former can be selected when the fragments are needed as "fingerprints" to compare with or screen in the database. The latter can be utilized when the ions

corresponding to the intact analyte molecules, termed as the molecular ions, are required for swift and reliable identification [62].

Electrospray ionization is another "soft" technique to produce analyte ions continuously in atmospheric pressure. The analyte is introduced in solution through a capillary with a cone at its end. A high voltage is applied between the capillary and the skimmer of the mass analyzer. Droplets are formed when the analyte solution is released from the capillary, whose size is reduced on the way to the orifice. While the mechanism of electrospray ionization is still under discussion [60, 63], one school of thoughts involves a continuous and repetitive process of desolvation and droplet fission. Desolvation is casued by the evaporation of the solvent, while the application of drying gas accelerates this process. Since the electrosprayed droplets are charged, fission is induced by electric repulsion between the excessive charges, or Coulomb explosion of the droplets. The continuous and repetitive desolvation and droplet fission lead to analyte molecules with multiple charges in the end [62]. As an example of further development and variation of electrospray ionization, nanoelectrospray ionization utilizes a refined capillary with reduced sample consumption and flow rate, which reduces the loss of biomolecules, signal suppression and adduct formation. Due to its "softness", electrospray is suitable for analysis of proteins, even those of large masses. Since the analyte is multiply charged, the m/z value might be reduced such that large biomolecules can be dealt with using inexpensive mass analyzers. Deconvolution or other means of simplification is helpful for interpretation of the measured m/z values, where the analyte is presented in multiple signals with different charge numbers [60, 62].

MALDI produces analyte ions in a "soft" but discrete manner. First the analyte is mixed in solution with a certain type of matrix that facilitates ionization. The mixture is applied to a target plate, where it is dried and the matrix crystals form. A pulsed laser, usually in the UV wavelength range, radiates the target surface. The energy of the laser pulses is absorbed by the matrix molecules, which leads to the ejection of singly protonated analyte ions in most cases [62]. Despite the controversy over its exact working mechanism [60, 63], MALDI has been used to analyze molecules in the mass range of $500\,\mathrm{Da}$ to $500\,000\,\mathrm{Da}$ with the choice of matrices made through empirical experience. On one hand, MALDI is advantageous in generating singly charged analytes, especially with large masses. On the other hand, it is difficult to remove the background signals from the matrix and to stabilize the signal intensities, which hinders quantization of this process [62].

In fast atom bombardment, a solution consisting of the analyte and a matrix

is introduced by a target as well. The target is bombarded by a fast atom beam of energetic rare gas neutrals. The desorbed ions originate from not only the analyte and its fragments but also the matrix. Fast atom bombardment typically produces analyte ions in the mass range of $300\,\text{Da}$ to $6000\,\text{Da}$ [62].

In secondary ion mass spectrometry, a beam of energetic ions is focused on to the analyte in the solid phase without any matrix, which sputters and ionizes the analyte molecules into the gas phase [63].

3.1.4   Mass analysis

After sample ionization, the analyte ions are guided into a mass analyzer, where they are separated according to their m/z values. Different types of mass analyzers utilize different motional features of ions in electric and/or magnetic fields to achieve such separations in space or time. Then the signal intensities detected correspond to the abundances of the separated ion groups. Commonly used types of mass analyzers include Time-Of-Flight (TOF), quadrupole, ion trap, orbitrap and Fourier Transform Mass Spectrometer (FTMS),together with their combinations and variations [60].

A TOF mass analyzer is basically a flight tube with an backing plate at one end and a detector at the other end. An electric field is applied between the backing plate and an acceleration grid [63]. After entering the flight tube, the ions are accelerated in the electric field, complete the travel distance and arrive at the detector with time delays determined by their m/z values. According to Newton's second law of motion, the kinetic energy of the ion could be denoted as

$$E = \frac{1}{2}mv^2 = eVz \tag{3.1}$$

with e as the elementrary charge, V as the accelerating potential and v as the ion velocity. The flight time of the ion is denoted as

$$t = \frac{L}{v} = L\sqrt{\frac{m}{z}\frac{1}{2eV}} \tag{3.2}$$

Rewriting Eq. 3.2 delivers the m/z value with respect to the flight time.

$$\frac{m}{z} = 2eV\frac{t^2}{L^2} \sim t^2 \tag{3.3}$$

Therefore, ions with lower m/z values travel faster and are detected earlier, while those with higher m/z values travel slower and are detected later. The TOF mass analyzer has theoretically no upper limit for the m/z value and the

capacity for fast averaging. It is also compatible with pulsed ion sources like MALDI [60]. The TOF mass analyzer can be configured in a few different manners, such as a linear and a reflectron configurations shown in Fig. 3.2. Mass resolution is a drawback of the linear configuration of the TOF mass analyzer [63]. A single stage gridded ion mirror, or a reflector, could be added into the flight tube at the end opposite to the entrance for ions, which applies a repulsive electric field to the ions and thus reflects them. When initial energy spread occurs to a group of incoming ions with identical m/z value, the reflected trajectory compensates the initial energy spread. The compensation consequently improves the resolution of the reflectron configuration of the TOF mass analyzers [62].
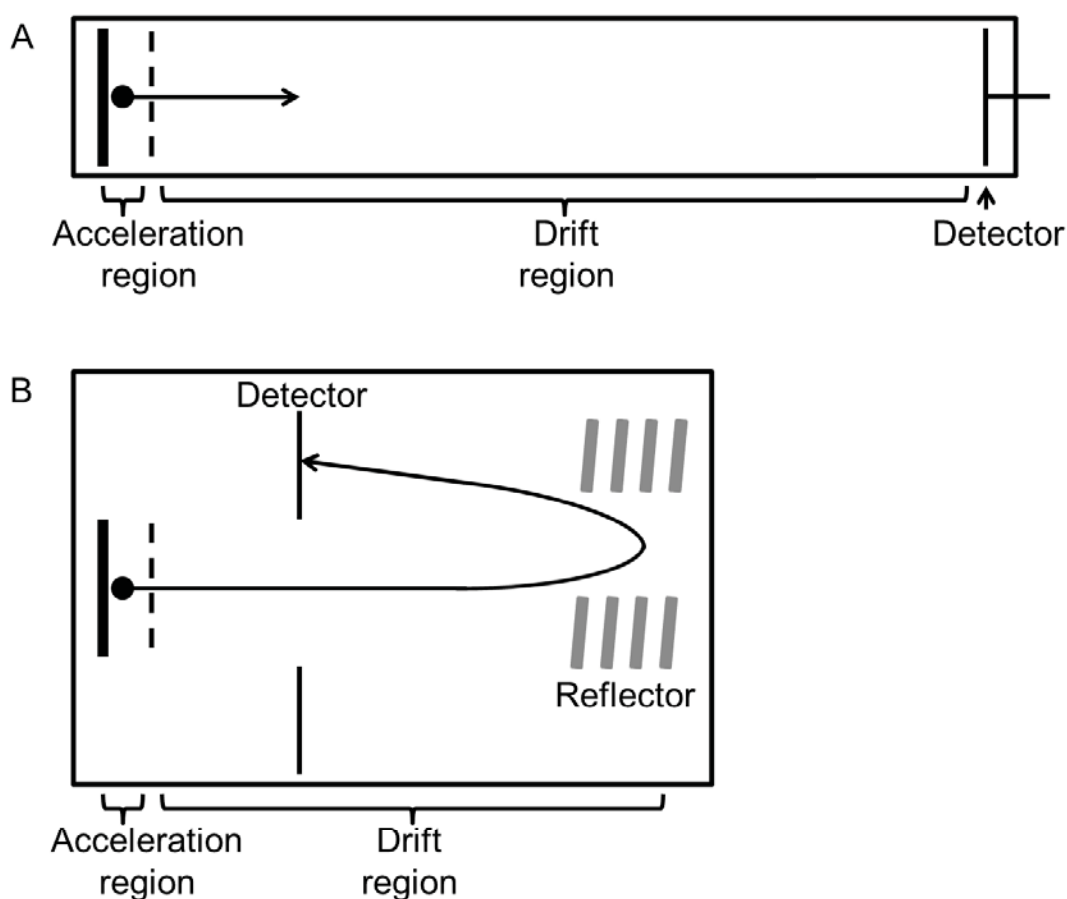
Figure 3.2: Linear (A) and reflectron (B) configurations of the TOF mass analyzer. Potential ion trajectories are depicted in both sub-figures.

A quadrupole mass analyzer incorporates four cylindrical electrodes with a static and a Radio Frequency (RF) electric field applied to them, where the elec-

trodes are arranged in parallel, but across each other, such as shown in Fig. 3.3. The incoming analyte ions follow complicated three-dimensional trajectories determined by their m/z values and the electric fields. The electric fields selects only one m/z value, so that a stable trajectory is established for the corresponding ions in between the electrodes. Ions with other m/z values follow unstable trajectories and deviate from the electrodes. Therefore, the quadrupole mass analyzer functions as a mass "filter" [60]. The quadrupole mass analyzer is advantageous in simplicity, robustness, expense and interfacing possibilities. In the meanwhile, there are limitations in its resolution, accuracy, upper limit of m/z value and scanning speed to cover the measuring range of m/z values. The combination of electrospray ionization and the quadrupole mass analyzer can extend the mass range of samples for measurements, since electrospray ionization renders multiply charged ions [62].
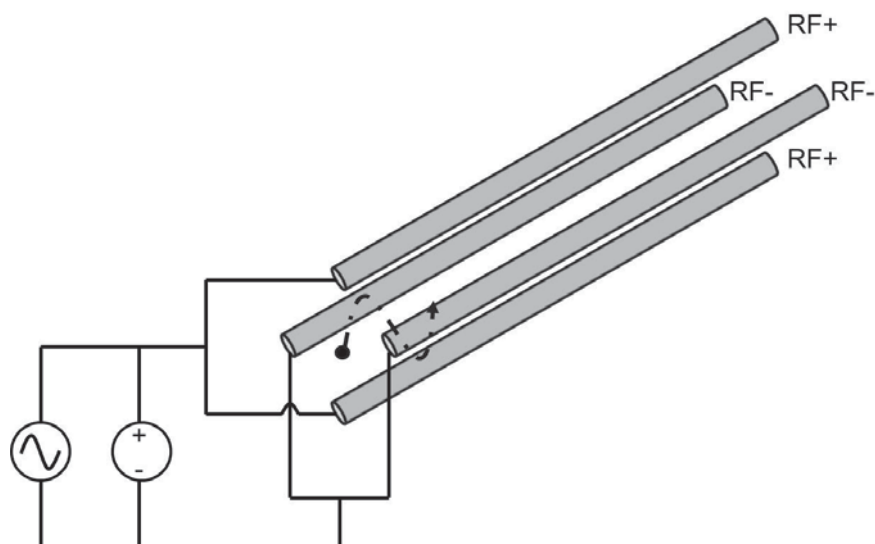
Figure 3.3: A quadrupole mass analyzer in sketch. The dashed curve depicts a possible ion trajectory in between the electrodes. The polarities of the RF voltages are marked out for only one half of the RF cycle, which are exchanged for the other half cycle.

An ion trap could be seen as a three-dimensional quadrupole mass analyzer, consisting of two end-cap electrodes and a ring electrode in the middle, with static and RF electric fields applied to the electrodes as well. In addition, dampening gas like helium is required. Different from the one-dimensional quadrupole mass analyzer, the ion trap mass analyzer could store all incoming ions with various m/z values in the equipment. The ejection of ions with a certain m/z value is performed by the choice of the electric fields [62]. Despite of its convenience, the ion trap mass analyzer consumes a long time for detection;

it has limited resolving power [1] and the upper m/z value around 6000; and the dampening gas may induce undesired collisions of the stored ions [60].

In an orbitrap mass analyzer, the motions of all incoming ions take place in the space between an inner spindle-shaped and an outer barrel-shaped electrodes coaxial to each other. A static electric field is applied to the two electrodes [60]. Due to the carefully engineered shapes of the electrodes and the electric field, the ions circle radially around and oscillate axially along the inner electrode at the same time. Only the axial oscillation frequency ω is related to the m/z value but independent from other variables,

$$\omega = \sqrt{\frac{k}{\frac{m}{z}}} = \sqrt{k\frac{z}{m}} \tag{3.4}$$

with k as an instrumental constant. Fourier Transform is applied to the measured signals of the axial oscillations, in order to distinguish different oscillation frequencies of ions with different m/z values [62]. Although it requires the lowest pressure, in other words the highest vacuum, the orbitrap mass analyzer has been commercialized to the length of three one-Euro coins (Thermo Electron Corporation), offering the resolving power of more than $70\,000$ [60].

A Fourier Transform mass analyzer has its core in a cell for ion cyclotron resonance, as shown in Fig. 3.4. Different from the mass analyzers described previously, a static and uniform magnetic field is applied to the cell, which leads to the cyclotron motions of all incoming ions along circular orbits. The angular frequency of an ion's cyclotron motion is related only to the magnetic flux density B and the m/z value,

$$\omega = \frac{eB}{\frac{m}{z}} = eB\frac{z}{m} \tag{3.5}$$

with e as the elementary charge. In order to excite ions of one m/z value, an RF voltage can be applied to the side panels of the cell, whose frequency is identical to the cyclotron frequency of the ions of interest. The excited ions process with increasing cyclotron radii but their angular frequency is maintained. When the ions approach the upper and bottom panels with electrodes, their angular frequency is detected as the oscillation frequency of the induced current at the electrodes [63]. In order to excite ions of various m/z values, a chirped signal with various frequencies can be employed [60]. Due to the various fre-

---

[1]The resolving power R is a specific m/z value divided by the difference in the m/z value Δm that can be distinguished by the mass spectrometer. $R = \frac{m/z}{\Delta m}$ [60].

quency components of the detected signals, Fourier Transform is applied to obtain the angular frequencies, from which the m/z values are calculated. Compared to other mass analyzers, the Fourier Transform mass analyzer offers the highest resolution and accuracy [62]. However, its high price and significant space consumption restrict its usage mainly to research laboratories.
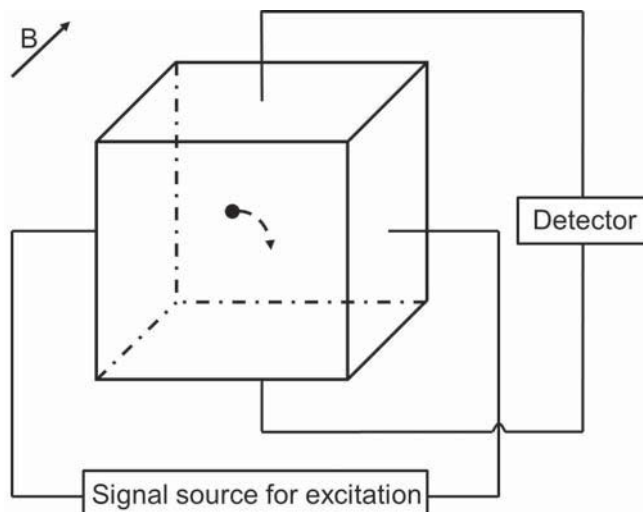

Figure 3.4: A Fourier Transform mass analyzer in sketch. The magnetic field is denoted by B. The two side panels of this cell are connected to the signal source for excitation of the ions. The top and bottom panels are connected to the detection device. Part of an ion's precessing trajectory is depicted in a dashed curve.

In order to obtain structural information on the analyte, the precursor ions are dissociated in the mass spectrometer and then the product ions are further measured of their m/z values. Tandem mass spectrometry could achieve this goal, utilizing single or multiple mass analyzers. The ion trap, the orbitrap and the FTMS as stand-alone mass analyzers can perform tandem mass spectrometry in the time domain [60]. Multiple identical or hybrid mass analyzers, e.g. TOF-TOF, quadrupole-TOF and so on, can fulfill this purpose in the space domain. In the latter case, a collision cell is usually built in between the mass analyzers.

After being separated in the mass analyzer according to their m/z values, the ions arrive at the detector, where signals are generated by their charge or momentum. Traditionally photographic plates were used, and a Faraday cup is a classical solution for large signals [63]. Modern instruments employ an electron multiplier as the detector, due to its advantages in low noise and high speed [62]. The electron multiplier offers good precision and significantly higher sensitivity compared to the Faraday cup [60].

Owing to the flourishing computer technology, the data system and the interpretation of mass spectra have been significantly advanced. For example, the probability based matching searches and compares the "fingerprints" of the analyte with a library or database [63], which brings along significant convenience and ease to researchers. However, it is necessary to understand and verify the interpretation of mass spectra and not to blindly trust the computer based searches.

3.1.5 Applications of mass spectrometers

In light of the capabilities to measure mass precisely and to provide structural information, various types and combinations of mass spectrometers are utilized in the fields of analytical chemistry, biochemistry, clinical diagnosis and others. The analytes can be inorganic or organic and of a wide range of mass. Amongst the manifold application scenarios, mass spectrometers are of special importance in proteomics. Proteomics is the identification, study and assessment of all the proteins expressed and modified during the lifetime of a cell [60, 62]. In the scope of the biological dogma from DNA to RNA and then to protein, proteomics is coherently in accordance with the central dogma and the associated fields of study, such as genomics. With respect to genomics, proteomics is complementary but more complicated. Several contributing factors are the great abundance of proteins expressed by the limited number of genes, post translational modifications, environmental influence and gene mutations [71]. Since proteins compose the main functional machinery in cells, proteomics can lead to significant and time-saving advancements in drug development and discoveries of prognostic markers, taking proteins as targets [71, 72].

The central focus of a proteomic study usually resides on a complex protein mixture. Mass spectrometry provides a precise solution to the analysis of such a protein mixture. After the protein mixture is either first separated and then digested (termed as top-down), or first digested and then separated (termed as bottom-up or shot-gun), the eventual assembly of peptides are analyzed with mass spectrometers and identified according to their m/z values and their dissociated components [60, 62]. Due to their "softness", electrospray ionization and MALDI are frequently used to introduce and ionize the peptides into the conjunctive mass analyzers, where tandem mass spectrometry is commonly employed in order to identify the peptides from their constituents [72, 73]. The technical features render mass spectrometry an appropriate tool in the pilot experiments to answer the two questions, posed in the beginning of this chapter,

concerning the effects of the PIRL ablation on proteins. The pilot experiments and the results, elaborated in the following sections, serve as a solid foundation to discuss not only the effects of the PIRL ablation on proteins, but also further integration of the PIRL ablation in mass spectrometry. Owing to the characteristics of the DIVE process, the PIRL ablation can potentially be combined with mass spectrometric technologies and utilized in the aforementioned application scenarios.

3.2   Material and methods

In the pilot experiments, tissue samples and proteinous molecules in solutions were ablated by the PIRL and the ablation plume was collected. Biochemical techniques were used to examine the abundance of proteins in the collected ablation plume of tissue samples. Furthermore, conventional mass spectrometry techniques were utilized to compare the chemical compositions of the ablated molecules and the corresponding controls, in order to investigate potential fragmentations as well as chemical or enzymatic changes induced by the PIRL ablation.

3.2.1   The PIRL ablation

The PIRL system is described in Chap. 2. The following are the parameters utilized during the pilot experiments on the application of the PIRL ablation under DIVE condition in mass spectrometry. The optical power of the PIRL beam at the sample surface was approximately $450\,\mathrm{mW}$. The optical energy density per pulse at the sample surface was $3.39\,\mathrm{J\,cm^{-2}}$. The peak power density was $1.13 \times 10^{10}\,\mathrm{W\,cm^{-2}}$, which at $1\,\mathrm{kHz}$ gives an average focused power density of $3.39 \times 10^3\,\mathrm{W\,cm^{-2}}$. However, the PIRL beam was scanned at the speed of $130\,\mathrm{mm\,s^{-1}}$ during the ablation process. The beam scanning was fast enough to sample a new spot between shots such that the focused fluence of $3.39\,\mathrm{J\,cm^{-2}}$ is the relevant parameter. In order to investigate whether the PIRL ablation is specific to protein species, a piece of mouse muscle tissue was ablated by the PIRL in a square pattern measuring $5\,\mathrm{mm} \times 5\,\mathrm{mm}$ over an ablation time of $5\,\mathrm{min}$. In order to examine with mass spectrometers possible fragmentation and chemical alternation in proteins ablated by the PIRL, aliquots of Ribonuclease A (RNase A) solution, trypsin solution and human blood plasma were utilized and transferred onto caps of reaction vials. The PIRL ablation was performed on the surface of the sample solutions in the square pattern measuring

$4\,\text{mm}$ x $4\,\text{mm}$, until the aliquot was completely ablated away.

3.2.2 Samples and corresponding ablation plume collection

Mouse muscle tissue

The mouse muscle tissue was directly used for the PIRL ablation without any sample preparation or treatment. The ablation plume was captured in a home built cryo-trap using liquid nitrogen, as shown in Fig. 3.5. This cryo-trap consisted of a vacuum pump unit (MZ 2C VARIO and CVC 2000, Vacuubrand GmbH + Co KG, Germany), a tubing system and a conical centrifuge tube (Falcon$^{\text{TM}}$ $50\,\text{ml}$, Thermo Fisher Scientific Inc., USA). The ablation plume was condensated at the bottom of the conical centrifuge tube due to the suction activated by the vacuum pump and the cooling by the liquid nitrogen.
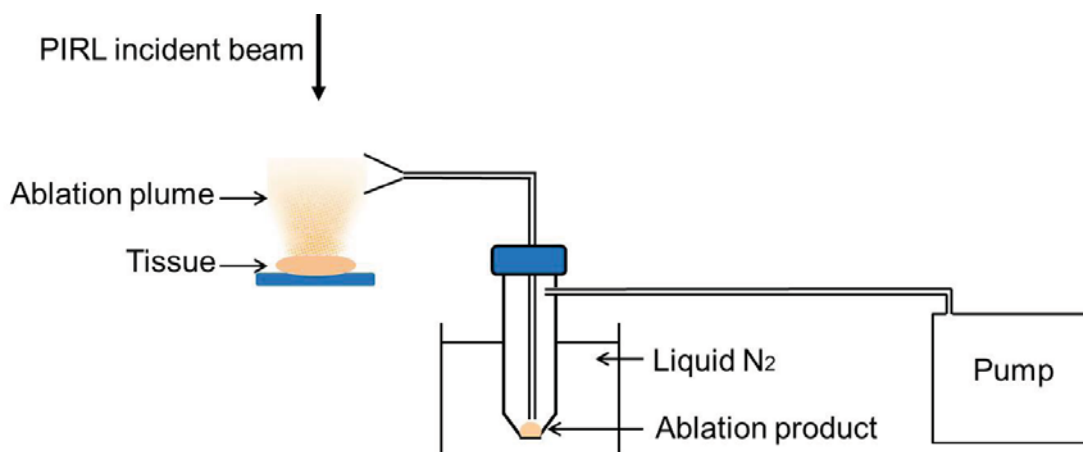
Figure 3.5: Schematic diagram of the setup to collect the ablation plume with a cryo-trap using liquid nitrogen. The vacuum pump activates a suction mechanism, through which the ablation plume is collected in the conical centrifuge tube. As the tube is cooled by liquid nitrogen, the ablation plume is condensated at its bottom.

RNase A solution

RNase A was purchased from Sigma-Aldrich BioChemie GmbH, Germany. The concentration of the RNase A solution was $5.9\,\mu\text{g}\,\mu\text{l}^{-1}$. The volume of $300\,\mu\text{l}$ from the RNase A solution was transferred to a reaction vial's cap and ablated by the PIRL. The ablation plume was captured with a home built trapping device. This trapping device utilized the vacuum pump, the tubing system and a plastic housing containing a C8 reversed-phase extraction membrane disc

(3M Empore$^{\text{TM}}$ SPE, Sigma-Aldrich). Before the PIRL ablation and the plume collection were performed, the extraction disc was conditioned with $300\,\mu l$ of pure acetonitrile (ACN) (HPLC-grade, Merck, Germany) and equilibrated with $0.1\,\%$ Formic Acid (FA) (Sigma-Aldrich, Germany) using the vacuum pump. During the PIRL ablation, the ablated RNase A molecules were trapped on the reversed-phase membrane due to the suction of the ablation plume activated by the vacuum pump.

As a control sample, un-ablated RNase A solution with the volume of $300\,\mu l$ was transferred onto another extraction disc and vacuumed over the reversed-phase membrane.

The reversed-phase membranes with the ablated RNase A molecules and the un-ablated control were placed into P-200 tips and washed with $200\,\mu l$ of $0.1\,\%$ Trifluoroacetic Acid (TFA) (Sigma-Aldrich). Elution was achieved with $200\,\mu l$ of $70\,\%$ ACN, $0.1\,\%$ TFA (dissolved in HPLC-H_2O). The samples were subsequently vaporized with a vacuum concentrator. The dried samples were dissolved in $20\,\mu l$ of $0.1\,\%$ FA for further mass spectrometric analysis.

Trypsin solution

Trypsin (non-sequencing grade, Sigma-Aldrich) was dissolved in $100\,mmol$ NH_4HCO_3 rendering the concentration of $4.55\,\mu g\,\mu l^{-1}$. A volume of $300\,\mu l$ from the trypsin solution was transferred to a reaction vial's cap and ablated by the PIRL. The ablation plume was captured with the cryo-trap using liquid nitrogen, as condensate at the bottom of a conical centrifuge tube (Thermo Fisher Scientific Inc.).

Human plasma serum

Human plasma serum was obtained from donation in accordance to the ethics committee of the medical association Hamburg. A volume of $300\,\mu l$ from the human plasma serum was transferred to a reaction vial's cap and ablated by the PIRL without any further treatment. The ablation plume was collected in the cryo-trap using liquid nitrogen.

3.2.3 Analytical methods

Gel elctrophoresis of ablated mouse muscle tissue

The concentration of proteins in the collected ablation plume of the mouse muscle tissue was determined with a NanoDrop 1000 spectrophotometer (Thermo

Scientific, USA) as $19.33\,\mu g\,\mu l^{-1}$. In order to perform Sodium Dodecyl Sulfate-Polyacrylamide Gel Electrophoresis (SDS-PAGE), $7.5\,\mu l$ of the collected ablated mouse muscle was dissolved in $5\,\mu l$ of four times concentrated sample buffer, $1\,\mu l$ of 20 times concentrated reducing agent and filled up to $20\,\mu l$ with HPLC-H_2O. The sample was incubated at $95\,°C$ for $5\,min$ and loaded onto a $10\,\%$ Criterion^{TM} XT Bis-Tris gel (Bio-Rad, Germany). The proteins were separated at a constant voltage of $120\,V$ for $45\,min$. The gel was stained over night according to Dyballa and Metzger [74] and destained with $40\,\%$ methanol.

Alpha-casein digestion of ablated trypsin solution

In order to test its enzyme activity, $1\,\mu l$ of the condensate collected during the PIRL ablation of the trypsin solution was dissolved in $79\,\mu l$ of trypsin resuspension buffer (Promega GmbH, Germany). For the purpose of tryptic digestion, $2.9\,mg$ of alpha-casein (Sigma-Aldrich) was dissolved in $100\,\mu l$ of urea ($6\,mol$). For reduction, $2.3\,\mu l$ of dithiotreitol (Sigma-Aldrich) ($100\,mmol$, dissolved in $100\,mmol\ NH_4HCO_3$ (Sigma-Aldrich)) was added and incubated for $10\,min$ at $56\,°C$. Afterwards, $2.3\,\mu l$ of iodacetamide (Sigma-Aldrich) ($300\,mmol$, dissolved in $100\,mmol\ NH_4HCO_3$) was added and incubated for $30\,min$ in the dark. Then $850\,\mu l$ of NH_4HCO_3 ($100\,mmol$) was added. Finally, the trypsin digest solution ($80\,\mu l$) was added and the sample was digested over night at $37\,°C$. The digest was acidified with FA and evaporated. The sample was dissolved in $70\,\mu l$ of $0.1\,\%$ TFA and desalted with home-made Oligo R3 (Life Technologies, Germany) micro-column as described in Ref. [75]. After desalting, the sample was evaporated and dissolved in $20\,\mu l$ of $0.1\,\%$ FA for nano Ultra Performance Liquid Chromatography-Electrospray Ionization-Quadrupole-Time-Of-Flight tandem mass spectrometry (UPLC-ESI-QTOF-MS/MS) analysis.

As a control sample, intact alpha-casein was dissolved in $0.1\,\%$ FA, rendering the concentration of $1\,\mu g\,\mu l^{-1}$ and analyzed without further trypsin incubation by nano UPLC-ESI-QTOF-MS/MS analysis.

Angiotensin I incubation of ablated human plasma serum

The amount of $4.752\,\mu g$ from the human plasma serum collected from the ablation plume was incubated with angiotensin I (Ang 1-10, with the concentration of $10^{-5}\,mol$, dissolved in MS-H_2O) at $37\,°C$. After defined incubation time spans ($0\,h$, $6\,h$ and $24\,h$), aliquots with the volume of $0.5\,\mu l$ were used for MALDI-TOF MS analysis.

MALDI-TOF MS analyses

MALDI-TOF MS analyses were performed on model Reflex IV (Brucker, Germany) equipped with an N_2-laser in positive ion-mode. Measurements on the RNase A sample were carried out in the linear mode with 2,5-dihydroxyacetophenone (DHAP) as matrix. In order to prepare the matrix, 7.6 mg of DHAP was dissolved in 375 µl of ethanol. After vortexing and sonification, 125 µl of diammonium citrate was added. The volume of 2 µl from the dissolved sample was mixed with 2 µl of 2% TFA and 2 µl of the DHAP solution in a tube with the volume of 0.5 ml. Due to friction on the tube surface, crystallisation seeds were created with a small pipette tip. The volume of 1 µl from the solution was loaded on a MALDI anchor chip target.

Measurements on the angiotensin I incubated with the ablated human plasma serum were carried out in the reflector mode. The sample was prepared according to the dried-droplet method with 2,5-dihydroxybenzoic acid (DHB) as matrix. The matrix solution consisted of DHB with the concentration of 20 mg ml^{-1} and ACN: 0.1% TFA with the volume to volume ratio of 30:70, dissolved in HPLC-H_2O. The volume of 0.5 µl from the angiotensin I incubated with the ablated human plasma serum was mixed with 0.5 µl of the DHB matrix solution and utilized for measurements with the MALDI-TOF mass spectrometer.

LC-MS/MS analyses

LC-MS measurements were performed by injecting the samples onto the nano UPLC-ESI-QTOF (nanoACQUITY, Waters, UK and QTOF Premier, Micromass/ Waters, UK) mass spectrometer. The samples were loaded at the rate of 5 µl min^{-1} on a trapping column (nanoACQUITY UPLC PST trap column, C18, 180 µm x 20 mm, 5 µm, 100 Å, Waters, UK; buffer A: 0.1% FA in HPLC-H_2O; buffer B: 0.1% FA in ACN) with 2% buffer B. After sample loading, the trapping column was washed for 5 min with 2% buffer B at the rate of 5 µl min^{-1}. The peptides were eluted at the rate of 200 nl min^{-1} onto the separation column (nanoACQUITY UPLC Ethylene Bridged Hybrid (BEH) column, C18, 75 µm x 150 mm, 100 Å; gradient: 2% to 50% B in 30 min in case of the short gradient, or in 90 min in case of the long gradient). The spray was generated from a fused-silica emitter (I.D. 10 µm, New Objective, USA) at a capillary voltage of 1520 V, a source temperature of 100 °C and a cone voltage of 40 V in positive ion mode. For MS/MS measurements, data were recorded in the data dependent acquisition mode. MS survey scans were performed over an m/z range

of 400 to 1500 with a scan time of $0.6\,\text{s}$ and an inter-scan delay of $0.05\,\text{s}$. The two most abundant signals were used for fragmentation. MS/MS spectra were obtained over an m/z range of 100 to 1500 with a scan time of $0.95\,\text{s}$ and a collision ramp of $22\,\text{eV}$ to $30\,\text{eV}$. An online exclusion was used to prevent multiple fragmentation events with the exclusion time of $20\,\text{s}$ and the exclusion window of $\pm\,2$.

Full scan MS spectra were recorded for measurements on intact proteins over an m/z range of 500 to 3000. A lock-spray spectrum was recorded for calibration every $10\,\text{s}$ with $1\,\text{pmol}\,\mu\text{l}^{-1}$ of [Glu1] Fibrinopeptide B (Sigma-Aldrich, Germany) over an m/z range of 100 to 1500 using a collision energy of $22\,\text{eV}$.

3.3 Results and discussion

3.3.1 Results

The PIRL ablation was applied to the mouse muscle tissue, the solutions of RNase A and trypsin, and human plasma serum, in combination with conventional analytical techniques including mass spectrometry, in order to investigate sample specific requirements and alternations of proteins during the DIVE process.

Over the ablation time of $5\,\text{min}$, the PIRL ablated away a piece of the mouse muscle tissue measuring $5\,\text{mm}$ x $5\,\text{mm}$ x $1.5\,\text{mm}$. No treatment was required for the mouse muscle tissue before the PIRL ablation. The collected ablation plume of the mouse muscle was condensated in the conical centrifuge tube, rendering a volume of $50\,\mu\text{l}$ with a protein concentration of $19.33\,\mu\text{g}\,\mu\text{l}^{-1}$. Therefore, $0.9665\,\text{mg}$ of proteins was extracted by the PIRL ablation from $37.5\,\text{mm}^3$ of mouse muscle. The volume of $7.5\,\mu\text{l}$ from the collected ablation plume was directly used for SDS-PAGE without any further processing. A significant number of bands were observed on the SDS-PAGE, ranging from a few kDa to a few hundred kDa, as shown in Fig. 3.6. Therefore, great abundance of different protein species was directly extracted by the PIRL ablation from the mouse muscle tissue.
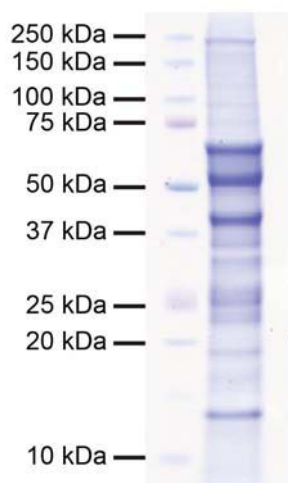
Figure 3.6: SDS-PAGE of proteins collected from the PIRL ablation of mouse muscle, reproduced from Ref. [61] with permission. Left: protein standards. Right: 145 μg of proteins from the mouse muscle ablated by the PIRL. Protein species with a large variety of molecular weights are present.

As a standard model protein commercially available, RNase A in solution was ablated by the PIRL and the ablation plume was collected and analyzed with a MALDI-TOF mass spectrometer and a LC-ESI-QTOF mass spectrometer. The un-ablated RNase A in solution was analyzed in the identical way as the control. The MALDI-TOF mass spectra in Fig. 3.7 present signals corresponding to the ablated and un-ablated RNAse A protein species doubly and triply protonated. Using the MALDI-TOF mass spectrometer, the spectra of the ablated and un-ablated RNase A molecules are almost identical to each other. The LC-ESI-QTOF mass spectrometer was employed as an alternative analysis to compare the ablated and un-ablated RNase A protein species. Due to the electrospray ionization employed, multiply protonated RNase A molecules are presented in the LC-ESI-QTOF mass spectra in Fig. 3.8 for both the ablated and the un-ablated samples. As a zoom-in of Fig. 3.8, deconvoluted spectra [2] of ablated and un-ablated RNase A molecules are shown in Fig. 3.9. All signals detected in the mass spectra of the ablated RNase A molecules were also found in the mass spectra of the un-ablated control, and vice versa. According to the mass spectrometry analyses, the ablated RNase A protein species was virtually identical to the un-ablated control. No fragmentation or chemical alternation was found for the RNase A molecules through the PIRL ablation.

---

[2]Deconvoluted mass spectrum presents a desired signal or desired signals extracted from a mass spectrum including the signal(s) but complicated, or convolved in other words, in certain ways [76].
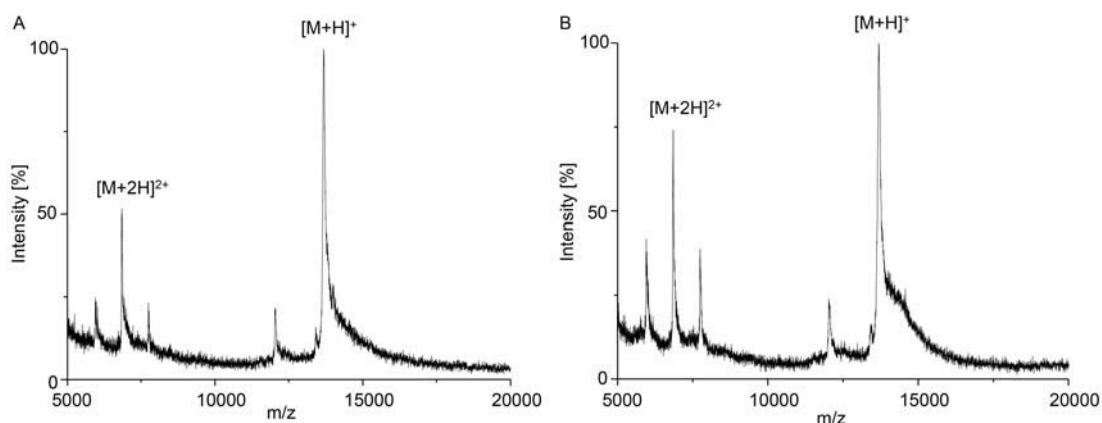
Figure 3.7: MALDI-TOF mass spectra of RNase A in solution ablated by the PIRL (A) and the un-ablated control (B). Matrix: 2,5-DHAP. Signals corresponding to the RNase A protein species doubly and triply protonated are marked out. The important features are the mass peaks. The differences in baseline and relative peak intensities are normal variations seen with matrix preparation in the MALDI method.
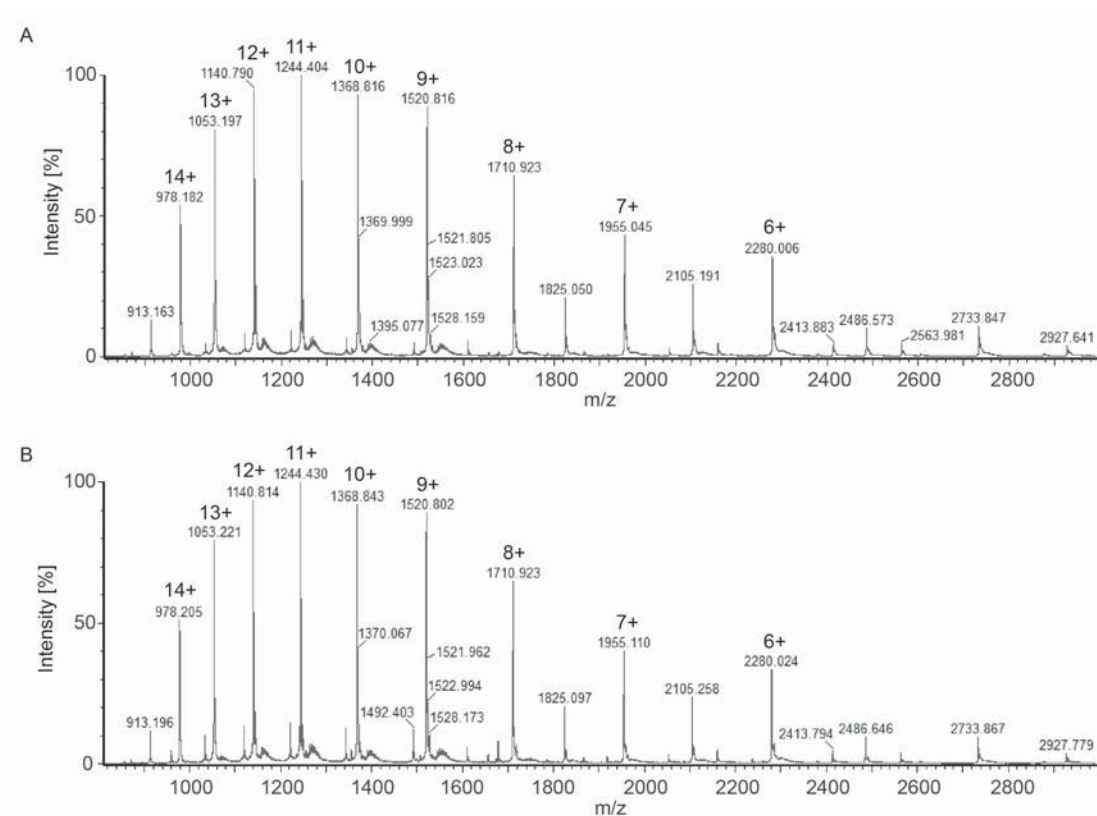
Figure 3.8: LC-ESI-QTOF mass spectra of RNase A in solution ablated by the PIRL (A) and the un-ablated control (B). Signals corresponding to the RNase A protein species six to fourteens times protonated are marked out.
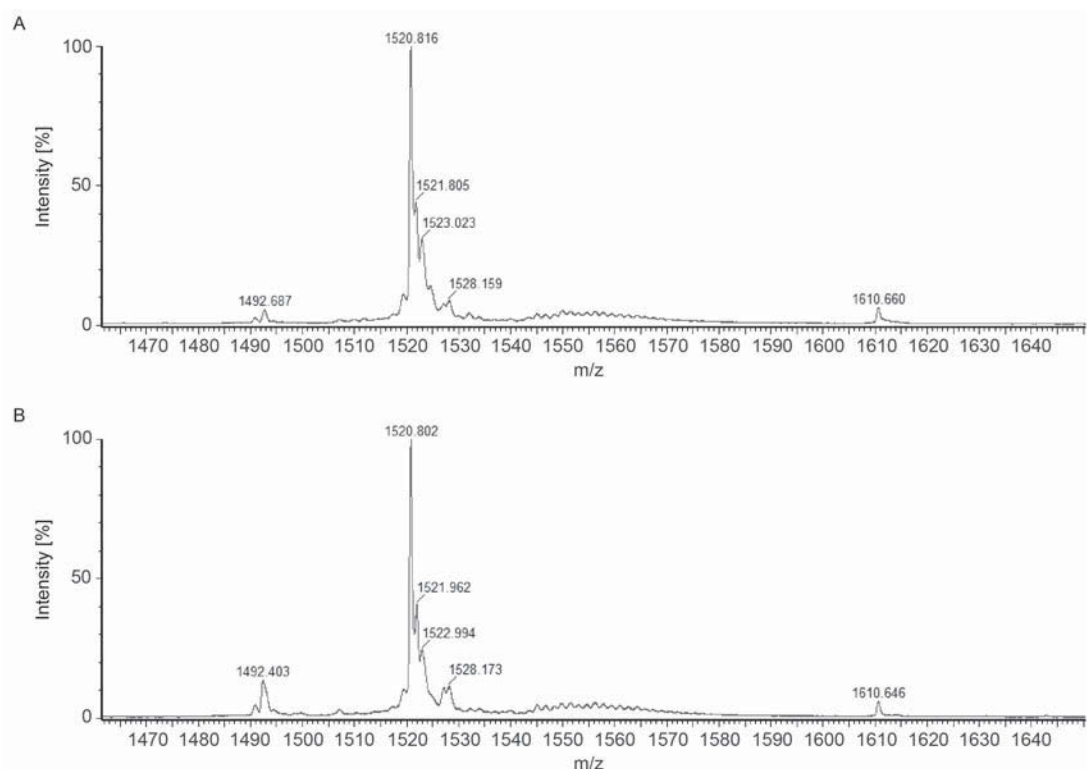
Figure 3.9: Deconvoluted LC-ESI-QTOF mass spectra of RNase A in solution ablated by the PIRL (A) and the un-ablated control (B). The most intensive signals correspond to RNase A protein species nine times protonated.

In addition to possible fragmentation and chemical alternation, it was studied whether the enzymatic activity of proteins would be preserved through the PIRL ablation. Trypsin and human blood plasma were selected for this purpose. Trypsin in solution was ablated by the PIRL, the ablation plume of which was collected and incubated with alpha-casein and analyzed with nano UPLC-ESI-QTOF-MS/MS. Alpha-casein not incubated with trypsin was analyzed in the identical procedure as a control sample. In the chromatogram of alpha-casein incubated with the ablated trypsin, no signals of the intact alpha-casein were observed, and a number of tryptic peptides were detected, as shown in Fig. 3.10 (A). For the non-incubated alpha-casein, the intact alpha-casein was observed but no tryptic peptides were detected, as shown in Fig. 3.10 (B). Hence, alpha-casein was digested during the incubation by the ablated trypsin, and on the contrary it remained intact without incubation. Therefore, trypsin maintained its enzymatic activity through the PIRL ablation.
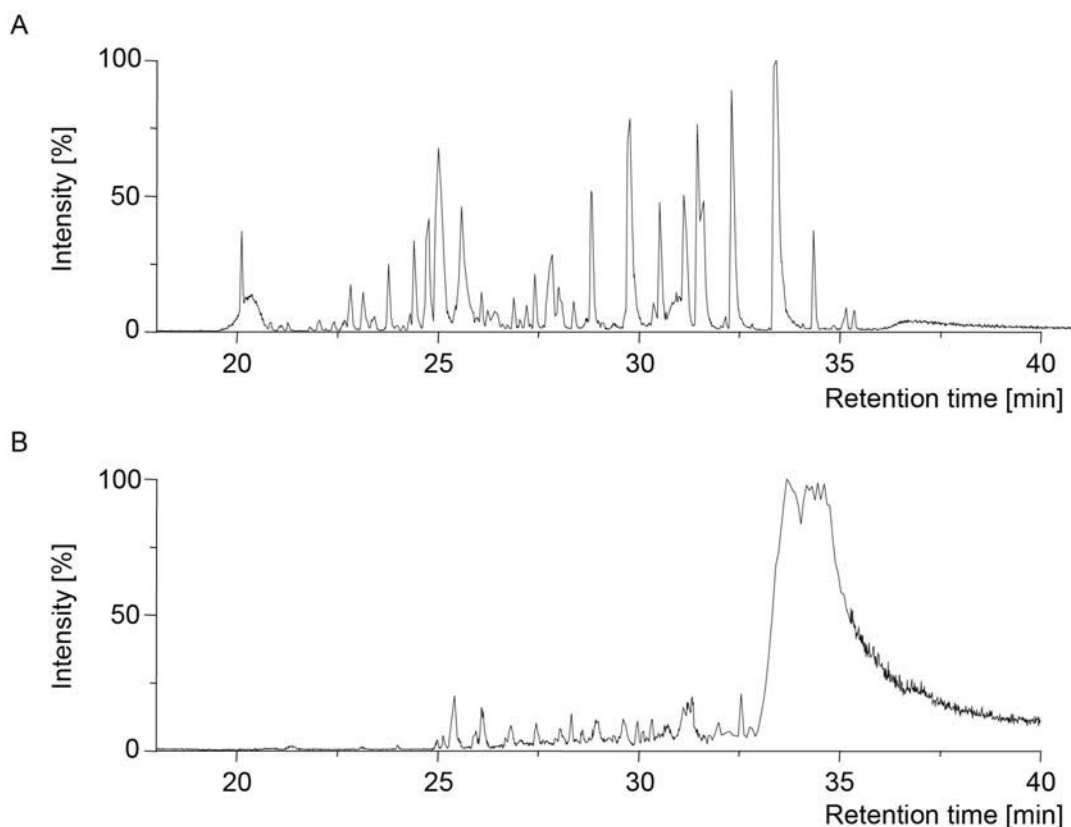
Figure 3.10: Base Peak-Chromatograms of the nano UPLC-ESI-QTOF-MS/MS analyses of alpha-casein digested by the ablated trypsin (A) and alpha-casein not incubated with trypsin (B), reproduced from Ref. [61] with permission. In chromatography, different components of the analyte are separated with respect to the retention time. In the base peak-chromatogram, a mass spectrum is recorded at each measuring point of the retention time, and the ion signal with the highest intensity in the mass spectrum is plotted in the chromatogram with respect to the retention time [76].

As a second model to investigate the potential effects of the PIRL ablation on enzymatic activities, human blood plasma serum was ablated and the collected ablation plume was incubated with Ang 1-10. The MALDI-TOF mass spectrometer was used to analyze the incubation results after $0\,\mathrm{h}$, $6\,\mathrm{h}$ and $24\,\mathrm{h}$, as shown in Fig. 3.11. After six hours of incubation, Ang 1-8 and Ang 6-10 were observed. After 24 hours of incubation, Ang 4-10 and Ang 1-7 were observed. These angiotensin peptides were generated from the precursor Ang 1-10 during the metabolizing proteolytic activities of enzymes in human blood plasma [77]. Therefore, the enzymatic activities of proteins in human blood plasma were maintained through the PIRL ablation.
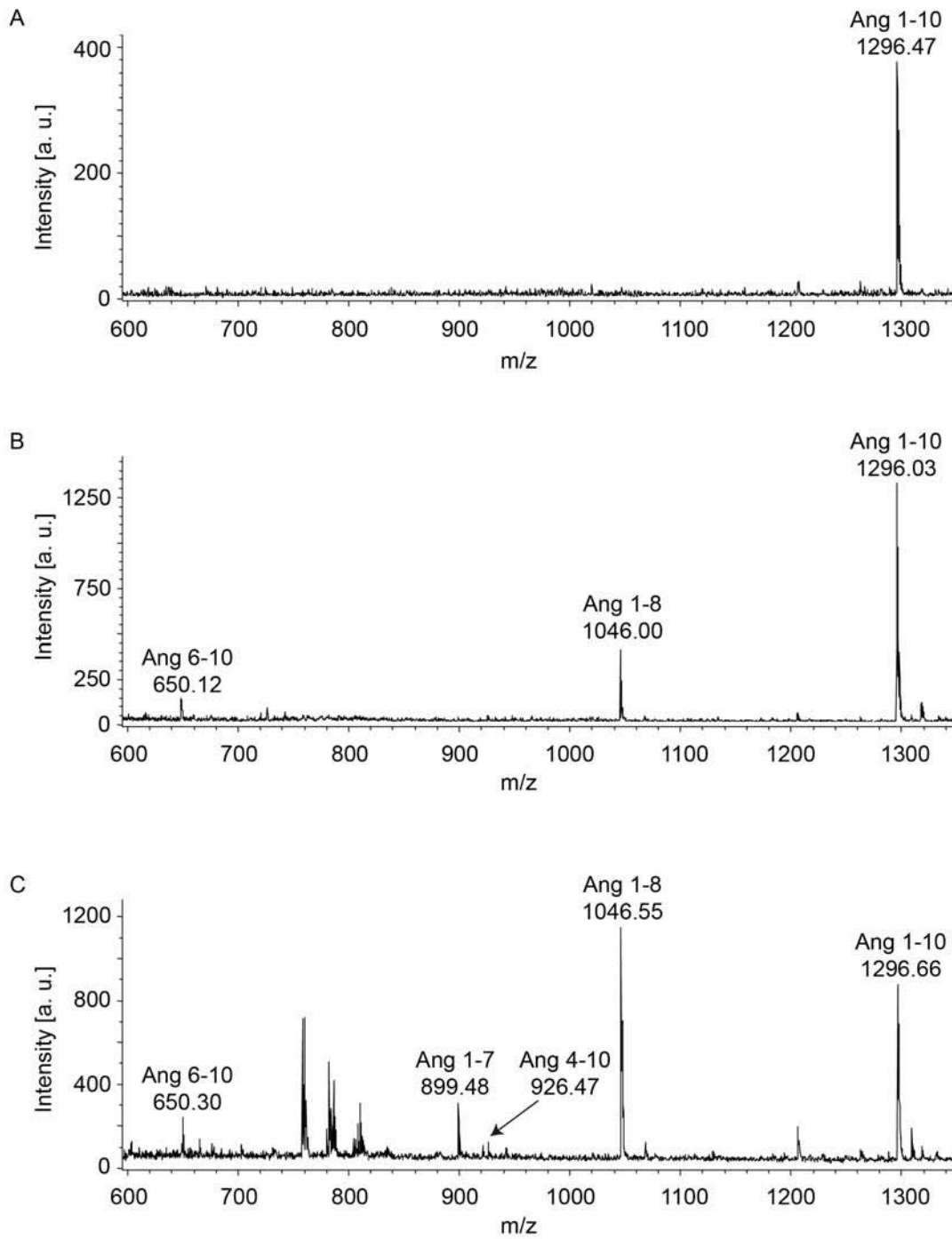
Figure 3.11: MALDI-TOF mass spectra of ablated human blood plasma serum incubated with Ang 1-10 for $0\,h$ (A), $6\,h$ (B) and $24\,h$ (C), reproduced from Ref. [61] with permission. Matrix: 2,5-DHB. Angiotensin peptides generated in the incubation were marked out.

3.3.2 Discussion

Analyses using conventional biochemical and MS techniques provided informative insight into the PIRL ablation plume of tissue samples and proteins in solutions. The pilot experiments provide answers to the two questions posed in the beginning of this chapter, concerning the effects of the PIRL ablation on proteins.

The first question is answered by investigating the proteins in the ablation plume of tissue. Great abundance of proteins was extracted by the PIRL ablation from the mouse muscle tissue, ranging from less than $10\,\text{kDa}$ to almost $250\,\text{kDa}$, as shown in the SDS-PAGE in Fig. 3.6. The huge variety of the proteins extracted from the mouse muscle tissue indicates that the PIRL did not impose any sample specific requirements.

The answer to the second question is derived from the analyses of the ablation plumes of RNase A solution, trypsin solution, and human plasma serum. The absence of fragmentation and chemical alternation during the PIRL ablation of RNase A in solution was verified against the un-ablated control with two types of mass spectrometers, MALDI-TOF and LC-ESI-QTOF. The mass spectra of the collected ablated RNase A samples were virtually identical to those of the un-ablated control in both cases, as shown in Figs. 3.7, 3.8 and 3.9. Therefore, RNase A molecules in solution did not suffer from detectable fragmentation or chemical change during the PIRL ablation. Furthermore, the enzymatic activities of proteins in the DIVE condition were examined using two models, trypsin and human plasma serum. The trypsin collected through the PIRL ablation maintained its enzymatic activity and digested alpha-casein completely into peptides during the incubation, as shown in Fig. 3.10 (A). The enzymes in human plasma serum maintained their Ang 1-10 metabolizing proteolytic activities throughout the PIRL ablation. During the incubation of the ablated human plasma serum with Ang 1-10, the presence of angiotensin peptides, i. e. Ang 1-8 and Ang 6-10 after $6\,\text{h}$ as well as Ang 4-10 and ang 1-7 after $24\,\text{h}$, verifies the preserved enzymatic activities of corresponding plasma proteases in the ablated human plasma serum, as shown in Fig. 3.11. Consequently, no deviation was observed in the enzymatic functions of trypsin and proteases in human plasma serum corresponding to Ang 1-10 metabolizing proteolysis, in the cases of trypsin and human plasma serum collected from the PIRL ablation plumes.

Both the physical principle of the DIVE process and the pilot experiments indicate that the PIRL ablation has great potential as a sampling technique to introduce proteins and other biomolecules to mass spectrometers, where *in situ*

and *in vivo* investigation could be envisioned. This aspect is further discussed in the following paragraphs.

The demand from analytical science and daily practice is an ever increasing request for mass spectrometry, especially on biological samples whose properties should be taken into account during analyses with mass spectrometers. It is necessary to adapt the instrumental configurations of mass spectrometers to the features of the biological analytes and the conditions of their origins. Despite of their "softness", electrospray ionization and MALDI are unsuitable for many types of biological samples, in that electrospray ionization requires the analyte dissolved in a solvent and that MALDI employs a denaturing matrix and high vacuum. Such necessities of electrospray ionization and MALDI are especially in conflict with *in vivo* investigations [78]. Derivations and variations of these two ionization techniques have emerged to ionize and introduce biological samples to mass analyzers, including Desorption Electrospray Ionization (DESI), Atmospheric Pressure Infrared MALDI (AP IR MALDI) and Laser Ablation Electrospray Ionization (LAESI).

In DESI, the charged solvent spray is applied to the unprepared samples on a substrate. There the samples are then desorbed, ionized and introduced into a mass analyzer [79]. An exemplary combination of DESI and an ion trap mass analyzer has provided information on lipids in human brain specimens, which could potentially intraoperatively guide brain tumor surgery according to tumor cell concentration [80]. AP IR MALDI utilizes oftentimes either an Er:YAG [81], or Nd:YAG [82], or Yb:YAG [83] laser pumped optical parametric oscillator to desorb the biological molecules, with the laser pulse duration on the order of nanoseconds. Combined with ion trap or TOF mass analyzers, AP IR MALDI has produced strong ion signals of peptides, metabolites and small carbonhydrates with artificial matrix [81, 83] or even in native water [82]. The LAESI technique established by Nemes and Vertes [84] also employs lasers at the wavelength of $2.94\,\mu m$ with nanosecond pulses to ablate water-containing biological samples into the gas phase, which are ionized by the electrospray. Studies on proteins, lipids and small metabolites have been performed *in situ* and *in vivo* with LAESI and mass analyzers like TOF and QTOF [78, 84, 85, 86, 87, 88]. During LAESI, fragmentation of biological molecules is claimed to be practically absent, and the internal energy of the ejected molecules and particulates is not significantly larger than that of electrospray ionization [88].

The integration of the PIRL ablation, a certain ionization mechanism (e.g. electrospray ionization) and a mass analyzer has the potential to set a foothold in the analysis of biological molecules and tissue samples, owing to the charac-

teristics of the DIVE process. As elaborated in Chap. 1, the PIRL ablation takes place with the confinement of thermal and acoustic transients and the threshold fluence of approximately $1\,\mathrm{J\,cm^{-2}}$ [3] for the biological samples in this study. In a stark contrast, the optical fluence in the LAESI experiments is higher, e.g. from $1.9\,\mathrm{J\,cm^{-2}}$ to $2.2\,\mathrm{J\,cm^{-2}}$ [78] to even around $15\,\mathrm{J\,cm^{-2}}$ [88], and the pulse width is much longer i.e. on the nanosecond scale. Since the shock wave dynamics affects the ejection of particulates and the internal energy of product ions [88], the PIRL ablation, with thermal acoustic confinement and low optical fluence directly coupling to translation motions for ablation, is more likely to ensure the production of molecular ions and the absence of fragmentation. Moreover, when the PIRL ablation is employed to introduce biological samples to mass spectrometers, there is no need to treat the sample in advance. This result is particularly important that one does not have to dissolve the sample in a solution, or to apply an external matrix. Therefore, the PIRL ablation can facilitate *in situ* and *in vivo* analyses with mass spectrometers. In the meanwhile, further investigations are necessary to gain a deeper understanding of the plume dynamics of the PIRL ablation, in order to optimize the combination with ion source and mass analyzer.

Not only the exact chemical compositions but also their spatial distributions are crucial to understanding complex biochemical processes at any point of an organism's life cycle [89]. Imaging mass spectrometry provides such a possibility in two dimensions or even potentially in three dimensions, exempting chemical tagging and antibodies [90]. MALDI is frequently coupled to ion trap or QTOF mass analyzers to perform tissue imaging [89, 91]. DESI with ion trap [80] or hybrid ion source with Fourier Transform mass analyzer [92] are also employed to probe brain, heart, and lung tissues. LAESI facilitates investigations on plant metabolic characteristics via molecular imaging and depth profiling as well [78]. A deterministic factor of the spatial resolution of imaging mass spectrometry is the focal diameter of the laser beam on the sample surface. Imaging mass spectrometers based on MALDI usually operate with the spatial resolution of $50\,\mathrm{\mu m}$ to $100\,\mathrm{\mu m}$, while the example based on LAESI has a lateral resolution of $350\,\mathrm{\mu m}$ and a depth resolution of $50\,\mathrm{\mu m}$ [78]. The PIRL parameters can be adjusted to give $10\,\mathrm{\mu m}$ lateral and micron longitudinal resolution due to the complete confinement of the absorbed energy and transduction to translational motions driving the ablation.

In this regard, tissue imaging is another niche to pursuit, amongst the many application possibilities of the PIRL ablation in mass spectrometry. When a translation stage and the corresponding control loop are added, the integration

of the PIRL ablation, the ionization mechanism and the mass analyzer could be configured to register mass spectra with respect to the location of the PIRL ablation. From one ablation site to the next, the PIRL ablation provides a means to scan through the region of interest on the tissue. Afterwards, the spatial distributions of the chemical compositions could be obtained from the tissue, with the DIVE process lending a hand in securing the intactness of the chemical compositions. Similar to the established laser-based techniques for tissue imaging, reducing the diameter of the focal spot of the PIRL beam could lead to the increase in spatial resolution. The PIRL beam can in principle be focused to the diffraction limit on the order of its wavelength, approximately $3\,\mu m$. As elaborated in Chap. 1, the PIRL radiation is absorbed within the first few micrometers of the tissues. These two dimensions can be reckoned as the optimal lateral and vertical resolution in the case of tissue imaging with the PIRL ablation. Furthermore, potential combinations of the PIRL ablation and large-scale analytical methods such as tissue microarrays [93] have a very positive outlook on advancing the research on not only large molecules like proteins and peptides but also drug metabolites and lipids. It is naturally necessary to fine-tune the instrumental details, including ablation parameters, ion source, measurement parameters, data acquisition and comparison, in order to gauge the specific samples and the aims of experiments.

4 Towards ultimate limit of biodiagnosis

4.1 Introduction

The extraction of biological complexes from their native environment is the first essential step towards biochemical analysis and disease diagnostics. Specific techniques must be employed to extract samples effectively. These techniques are highly dependent upon the biological complex, biomolecular, viral or cellular, and the medium from which the extraction is performed [94, 95]. Such extraction techniques involve homogenization, elution and concentration of samples like blood [96], feces [96], urine [97], plant tissues [98, 99] and suspected foods for pathogen detection [100]. Further processing of such samples can be time consuming and involve complicated specific biochemical purifications, before subsequent analytical and diagnostic procedures can be performed. In certain scenarios, including determination of inflammatory or cancerous conditions, biopsies are employed to obtain cells or tissues. However, the biopsies, especially when incisions or needles are used to remove macroscopic quantities, commonly result in secondary infections [101, 102], pain [103, 104] and prolonged healing time [104]. This chapter elaborates on the development and characterization of a laser based extraction method capable of removing volumes as small as a few cells with the integrity of the constituent material fully preserved. The method is free from mechanical intervention, which significantly reduces the complexity and time required for the extraction of biological entities, compared to conventional extraction methods. The potential of this method is also demonstrated to substantially increase the speed for biological analysis and disease diagnosis.

Laser based methods to extract biological samples have been under development for a number of years [105], where laser radiation has been frequently utilized as a tool for the excision of tissue [106, 107, 108, 109]. The CO_2 laser is a common solution used in laser cone biopsy [107] and endoscopic laser ex-

cisional biopsy [108] in the operation theater. Laser cutting microdissection techniques employ a UV laser [110, 111] to excise the region of interest, after which downstream molecular analysis is performed on the obtained sample. Laser capture microdissection techniques isolate specific tissue regions for biopsy, utilizing an infrared wavelength of $10.6\,\mu m$ (CO_2 laser) to melt a plastic membrane on top of the tissue and then lifting off the region of interest [109]. These laser based extraction methods result in similar benefits and drawbacks that are incurred for a given laser's application to surgical cutting. As typical for CO_2 laser cutting, excessive tissue removal and thermal damage can lead to prolonged healing time and complications [112].

In contrast to conventional medical lasers, the PIRL scalpel under DIVE condition has been demonstrated to cut at the fundamental (single cell) limit for minimally invasive surgery, effectively without scar tissue formation [8] by taking advantage of the extremely high absorption of the vibrational stretching mode of water [1, 9, 10] in the $3\,\mu m$ wavelength range. The pulse duration of PIRL, on one hand, avoids excessively high peak powers of the incident radiation that would lead to multiphoton ionization and plasma formation with accompanying massive fragmentation and loss of the identity of the constituent material, and on the other hand, minimizes shock wave damage and thermal degradation. Applications of the PIRL ablation under DIVE condition, further beyond the surgical ones, can be derived from the characteristics of the ablation process.

In this chapter, the DIVE process is specifically exploited for the purposes of rapid extraction of biological systems, which can lead to numerous applications for high speed, on-the-fly detection, of micrometer scale biopsies of sample volumes as small as $10^{-13}\,l$ or less (sub-picolitre). Several methods were employed to investigate the higher order integrity and functionality of the biological entities ablated by the PIRL under DIVE condition from frozen concentrated aqueous solutions or suspensions and also from their natural environment. The analytical techniques include high-resolution microscope imaging, western blot analysis, colony development and inoculation tests, in order to examine the integrity and activity of collected ablated biological complexes. To ensure spatially homogeneous samples, the biological complexes were prepared in pure solutions or suspensions as samples for the PIRL ablation and plume collection. The examinations following ablation and collection revealed intact high order structure of the intercellular globular protein ferritin, intact structural integrity and sustained fluorescence of the commonly used fluorescent labeling protein recombinant Green Fluorescence Protein (rGFP), and intact biological activities

of *Tobacco Mosaic Virus* (TMV, Family *Virgaviridae*, Genus *Tobamovirus*) and *Saccharomyces cerevisiae* (*S. cerevisiae*) cells. Especially for the infectious agent TMV, the gentleness of this laser extraction method is further verified by successfully inoculating the TMV collected from the ablation plume into the live leaves of *Nicotiana glutinosa* L. Furthermore, it is demonstrated that the PIRL ablation is capable to extract infectious agents like TMV from its natural environment, e.g. systematically infected tobacco leaves, and that the extracted sample (the collected ablation plume) maintains its biological activity, validated by the inoculation test. These results confirm that the ablation plume collected during the DIVE process serves as a valid sample for analysis and biodiagnosis, establishing the PIRL ablation under DIVE condition as a direct, simple, and effective method for the soft extraction of biological entities. A part of the results in this chapter is published in Ref. [113].

4.2 Material and methods

4.2.1 The PIRL ablation

The PIRL system has been described in Chap. 2. In the experiments related to this chapter, the PIRL beam was focused onto the sample with an optical power of $350\,\mathrm{mW}$. The transverse beam diameter at the focus was approximately $130\,\mu\mathrm{m}$. The energy density at the focus was $2.64\,\mathrm{J\,cm^{-2}}$, which was above the threshold of $1\,\mathrm{J\,cm^{-2}}$ for the DIVE condition [114] regarding to the biological samples in this study. The PIRL beam was scanned in a square pattern measuring $4\,\mathrm{mm} \times 4\,\mathrm{mm}$ at the speed of $200\,\mathrm{mm\,s^{-1}}$, so that the consecutive pulses did not overlap. The ablation was performed by applying the scanning pattern to the sample surface. The aqueous samples were kept frozen with dry ice during the entire ablation process. Dark field imaging of the PIRL ablation of ice was used to verify the minimization of recoil or splashing from the sample, as shown in Fig. 4.1.
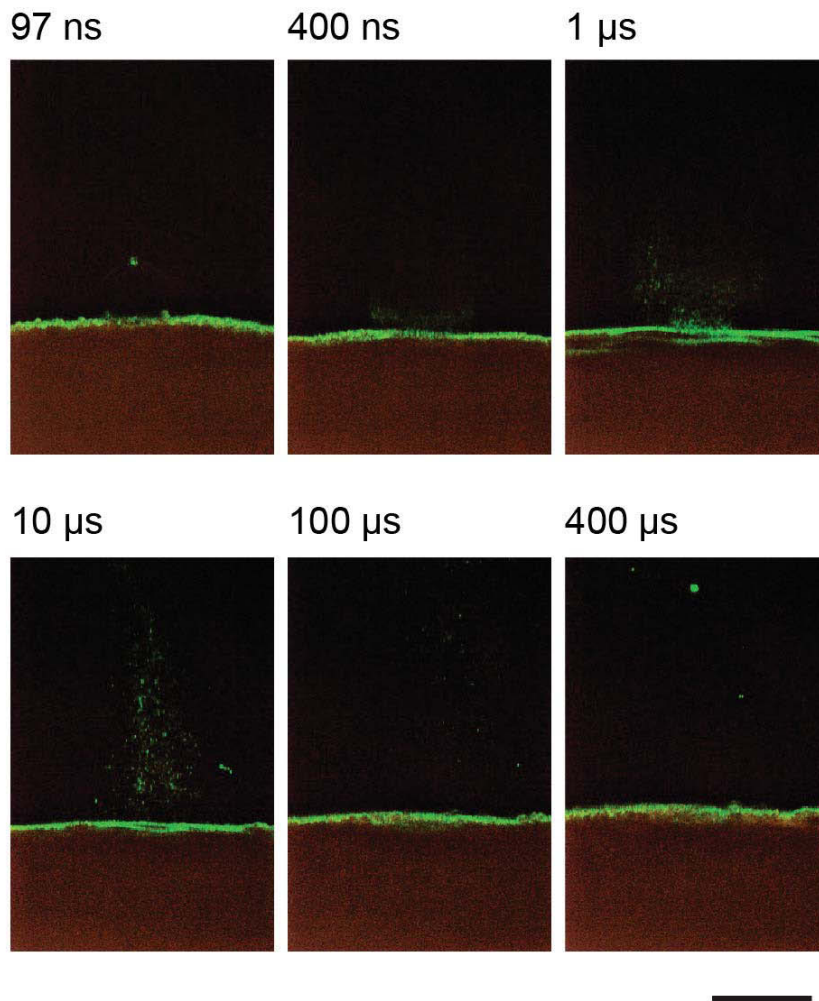
Figure 4.1: Dark field imaging [114] of the PIRL ablation under DIVE condition of ice (courtesy of Jing Zou [115], reproduced with permission). No recoil or splashing was observed up to $10\,\mu s$ after ablation, which is consistent with the ablation plume measurement carried out on liquid water [114]. Small particles with a size less than $10\,\mu m$ were observed at times later than $10\,\mu s$ and were significantly fewer in number and size compared to measurements performed on liquid water [114]. Images were acquired with a camera (D3100, Nikon, Japan) following the PIRL ablation with delay times of $94\,ns$, $400\,ns$, $1\,\mu s$, $10\,\mu s$ and $500\,\mu s$. Similar to the setup described by Franjic & Miller [114], a multimode fiber (M37L02, Thorlabs Inc., US) delivered the illumination light with a pulse duration of $100\,ps$ and a pulse energy of $200\,\mu J$ at the wavelength of $526\,nm$ onto the ablation site. All delays were carried out with the same illumination source. The ablation was performed by focusing the PIRL beam with a pulse duration of $100\,ps$ and a pulse energy of $130\,\mu J$ at the wavelength of $2.91\,\mu m$ to a spot with the diameter of $100\,\mu m$ ($1/e^2$ intensity level). The ice sample was $18.0\,M\Omega$ nanopure water cooled with dry ice, kept in a stainless steel well with the inner diameter of $6\,mm$ and the depth of $4\,mm$. The scale bar represents $200\,\mu m$.

4.2.2   Samples

Ferritin was purchased from Serva Feinbiochemica GmbH & Co. KG, Germany, $2\times$ crystallized, ultra-pure, $10\,\%$ sterile aqueous solution from equine spleen. rGFP was purchased from Takara Bio Europe/Clontech, France, catalog number 632373, $1\,\mathrm{mg\,ml}^{-1}$. The ferritin and rGFP samples were used without further purification. A final concentration of approximately $40\,\mathrm{mg\,ml}^{-1}$ TMV-T1 [116] was purified from *Nicotiana tabacum* L. cv. Samsun according to Gooding & Hebert [117] and a $10\,\%$ to $40\,\%$ (weight/volume) sucrose gradient. The source of *S. cerevisiae* cells was food-grade fresh baker's yeast, purchased from F. X. Wieninger GmbH, Germany. A suspension of *S. cerevisiae* cells was obtained after centrifugation of $0.552\,\mathrm{g}$ of the yeast paste and $1\,\mathrm{ml}$ of water. The above samples, namely solutions of ferritin, rGFP and TMV and suspension of *S. cerevisiae* cells, were frozen before the PIRL ablation. Tobacco leaves systematically infected with TMV were used directly for the PIRL ablation without any treatment. The source of *Tyrolichus casei* mites was food-grade mite cheese, purchased from Würchwitzer Milbenkäse, Schmelzer & Pöschel GbR, Germany. A suspension of *Tyrolichus casei* mites was obtained after centrifugation of $0.375\,\mathrm{g}$ of the matrix with the mites and $1\,\mathrm{ml}$ of water. The suspension of *Tyrolichus casei* mites was frozen before the PIRL ablation.

4.2.3   Ablation processes and analyses of collected ablation plume

Ablation and TEM imaging of ferritin

The ablation plume from ferritin was collected directly onto Transmission Electron Microscope (TEM) grids (carbon film on 400 square mesh copper, Electron Microscopy Sciences, USA), which were placed obliquely above and parallel to the ablation site with the PIRL beam propagating in vicinity, over an ablation time of $50\,\mathrm{ms}$. An aliquot of un-ablated ferritin was deposited onto the TEM grids and dried as a control. The grids and samples were then negatively stained with $1\,\%$ uranylacetate (Merck KGaA, Germany). The TEM grids used to image the collected ablation plume of ferritin and the un-ablated control were glow discharged with a formvar carbon film (Electron Microscopy Sciences). TEM imaging was performed on an FEI Tecnai G20 microscope (FEI company, The Netherlands) equipped with a 2K wide angle CCD camera (Veleta, Olympus Soft Imaging Solutions GmbH, Germany) using an acceleration voltage of $80\,\mathrm{kV}$. The line tool of the software ImageJ (http://imagej.nih.gov/ij/ Wayne Rasband, National Institute of Health, USA)

was used to measure the diameters of ferritin particle in the TEM images of ferritin collected from the ablation plume and the un-ablated control.

Ablation and fluorescence microscopy of rGFP

The ablation plume from rGFP was collected directly onto microscope glass slides (Superfrost, Glaswarenfabrik Karl Hecht KG, Germany), which were placed above and parallel to the ablation site with the PIRL beam propagating through the slides, over an ablation time of $30\,s$. The un-ablated control was deposited directly onto microscope glass slides. Fluorescence images were acquired with a Nikon Ti-U inverted microscope (Nikon GmbH, Germany) equipped with a 40x objective with a Numerical Aperture (NA) of 0.6 (CFI S Plan Fluor ELWD 40X, Nikon GmbH) and a Nikon DS-Vi1 CCD camera (Nikon GmbH). An ultra-high pressure 130W mercury lamp (Intensilight, Nikon GmbH) with a $450\,nm$ to $490\,nm$ bandpass filter was used for sample illumination and excitation. Fluorescence images of the sample were taken with a $505\,nm$ long-pass dichroic mirror and filtered with a $515\,nm$ long-pass filter (B2-A, Nikon GmbH).

Ablation and fluorescence spectroscopy of rGFP

The ablation plume from rGFP was collected directly onto microscope glass slides, which were placed above and parallel to the ablation site with the PIRL beam propagating through the slides, over an ablation time of $50\,s$. The un-ablated control was deposited directly onto microscope glass slides. Fluorescence spectra were then acquired with a confocal laser scanning microscope equipped with a spectral detector (LSM 510 META FSC, Carl Zeiss Microscopy GmbH, Germany) using a 10x objective with an NA of 0.3 (Plan Neofluar 10x, Carl Zeiss Microscopy GmbH). The $488\,nm$ laser line of an argon laser (LASOS Lasertechnik GmbH, Germany) was used for excitation.

Ablation and western blot analysis of rGFP

The ablation plume from rGFP was collected in a glass bottom dish (MatTek Corporation, USA) placed upside down above the ablation site during an ablation time of $120\,s$. The MatTek glass bottom dish containing the collected ablation plume was washed with $100\,\mu l$ Laemmli-Buffer which was then loaded onto a $15\,\%$ SDS-PAGE. After the electrophoresis the protein was transferred onto a Hybond enhanced chemiluminescence nitrocellulose membrane (Code: RPN3032D) and incubated in a GFP-horseradish peroxidase antibody (Santa

Cruz, SC-8334). The signals were detected using the SuperSignal West Femto Maximum Sensitivity Substrate (Pierce) and Amersham Hyperfilm™ (Product Code 28906837). The film was digitalized with an Epson Perfection 4870 Photo scanner.

Ablation and TEM imaging of TMV

The ablation plume of TMV was deposited directly onto TEM grids over the ablation time of $110\,$s. An aliquot of un-ablated TMV control was deposited onto the TEM grids and dried. TEM grids used to image the collected ablation plume of TMV and the un-ablated control were glow discharged with the formvar carbon film, and negatively stained with $1\,\%$ uranylacetate. TEM imaging was performed on the FEI Tecnai G20 microscope equipped with the 2K wide angle CCD camera using an acceleration voltage of $80\,$kV.

Ablation and inoculation test of TMV

A micro scrubber bottle (Bohlender GmbH, Germany) was filled with $2\,$ml of sodium phosphate buffer ($10\,$mmol, pH 7) to collect the ablation plume of TMV over an ablation time of $720\,$s with the gas-washing mechanism enabled by the vacuum pump unit (Vacuubrand GmbH + Co KG). The concentration of the ablation plume of TMV collected in the micro scrubber bottle was estimated as $0.2\,$mg ml^{-1} in optical extinction measurements according to Brakke [118] using Pico Drop (Pico Drop Ltd, UK). Leaves of *Nicotiana glutinosa* L. at the four to six leaves stage were inoculated with $20\,$µl of the collected ablation plume. The phosphate buffer was used as a negative control. The leaves were incubated for 96 hours until local lesions were observed.

Ablation of systematically infected tobacco leaves and inoculation test of collected plume

The micro scrubber bottle was filled with $2\,$ml of sodium phosphate buffer ($50\,$mmol, pH 7) containing $2\,\%$ (weight/volume) polyvinylpyrrolidon and $0.2\,\%$ (weight/volume) sodium sulfite, in order to collect the ablation plume of tobacco leaves systematically infected with TMV over an ablation time of $1430\,$s with the gas-washing mechanismenabled by the vacuum pump unit (Vacuubrand GmbH + Co KG). One of the systematically infected leaves after the PIRL ablation is shown in Fig. 4.2. Leaves of *Nicotiana glutinosa* L. at the four to six leaves stage were inoculated with $20\,$µl of the collected ablation plume. The

phosphate buffer was used as a negative control. The leaves were incubated for 96 hours until local lesions were observed.

Figure 4.2: Representative tobacco leaf systematically infected with TMV after the PIRL ablation. Since the square scanning pattern was applied during the ablation process, the rectangular features imprinted on the leaf were those ablated away by the PIRL.

Ablation and confocal microscopy of *S. cerevisiae* cells

The ablation plume from *S. cerevisiae* cells was collected directly onto microscope glass slides over an ablation time of $120\,$s. The microscope glass slides were fixed with $2\,\%$ (volume/volume) paraformaldehyde (Electron Microscopy Sciences) in phosphate buffered saline (PAA Laboratories GmbH, Austria) immediately after the PIRL ablation. The collected ablation plume containing *S. cerevisiae* cells was stained with Cell Mask orange plasma membrane stain (Life technologies, Germany) and DRAQ5 DNA stain (BioStatus Limited, United Kingdom). The samples were embedded in Mowiol 4-88 (Art.-No. 0731, Carl Roth GmbH + Co. KG, Germany) and imaged with a confocal laser scanning microscope (LSM 510 META FSC, Carl Zeiss Microscopy GmbH) using a 40x objective with an NA of 1.3 (Plan Neofluar 40x, Carl Zeiss Microscopy GmbH).

Ablation and microscope imaging of *S. cerevisiae* cells collected on growth medium

The Yeast-Extract-Peptone-Dextrose (YEPD) growth medium [119] was poured into petri dishes, leaving an open window in the center. The petri dishes were placed upside down above and parallel to the ablation site with the PIRL beam transmitted through the window. The ablation plume containing *S. cerevisiae* cells was deposited directly onto the YEPD growth medium over an ablation time of $120\,$s. *S. cerevisiae* cells collected from the ablation plume were cultured on the YEPD growth medium and colonies developed over 120 hours. Images of the yeast colonies were acquired in oblique illumination mode using a Nikon

AZ 100 multizoom microscope (Nikon GmbH) equipped with a Nikon DS-Ri1 digital camera (Nikon GmbH).

Ablation and microscope imaging of *Tyrolichus casei* mites

In order to capture the ablated *Tyrolichus casei* mites, double-sided adhesive tape was applied to microscope glass slides, leaving a window in the center. The microscope glass slides were placed above and parallel to the ablation site with the PIRL beam transmitted through the window and the adhesive tape facing the ablation site. The ablation plume containing *Tyrolichus casei* mites was deposited directly onto the microscope glass sides over an ablation time of $240\,s$. Immediately after the ablation process, the microscope glass sides were examined using a light microscope Nikon AZ 100 (Nikon GmbH) with a Nikon DS-Ri1 CCD camera (Nikon GmbH). The un-ablated control was deposited on to the microscope glass slides and examined with the light microscope directly.

4.3   Results and discussion

4.3.1   Results

The PIRL ablation under DIVE condition was applied to frozen aqueous solutions or suspensions of four biological entities: ferritin, rGFP, TMV and *S. cerevisiae* cells. The ablation plume was collected, analyzed and compared with the corresponding control, where the structural integrity and biological activity of the samples were verified. It was demonstrated that these biological entities in the ablation plume maintained their integrity and function. Furthermore, the PIRL ablation was applied to tobacco leaves systematically infected with TMV, where the ablation plume was collected and inoculated onto host plants. The biological activity of TMV shown by the successful inoculation test confirmed that the PIRL ablation is a simple and direct method to extract pathogens like TMV from the natural environment.

Proteins

Representative TEM images, as shown in Fig. 4.3, present negatively stained ferritin collected directly from the ablation plume onto TEM grids and the un-ablated control deposited and dried onto TEM grids. The toroidal structure of ferritin protein surrounding the iron core is clearly visible in the images from both samples. No significant structural variation was observed in the ferritin

complexes collected from the ablation plume. Corresponding structure and characteristics were also observed in the un-ablated ferritin control. The measured average diameters of the ferritin complexes were 12.6 ± 0.6 nm for the ablated and 12.6 ± 0.8 nm for the un-ablated samples. Consequently, the overall high order structure of the ferritin complex was preserved through the PIRL ablation under DIVE condition.
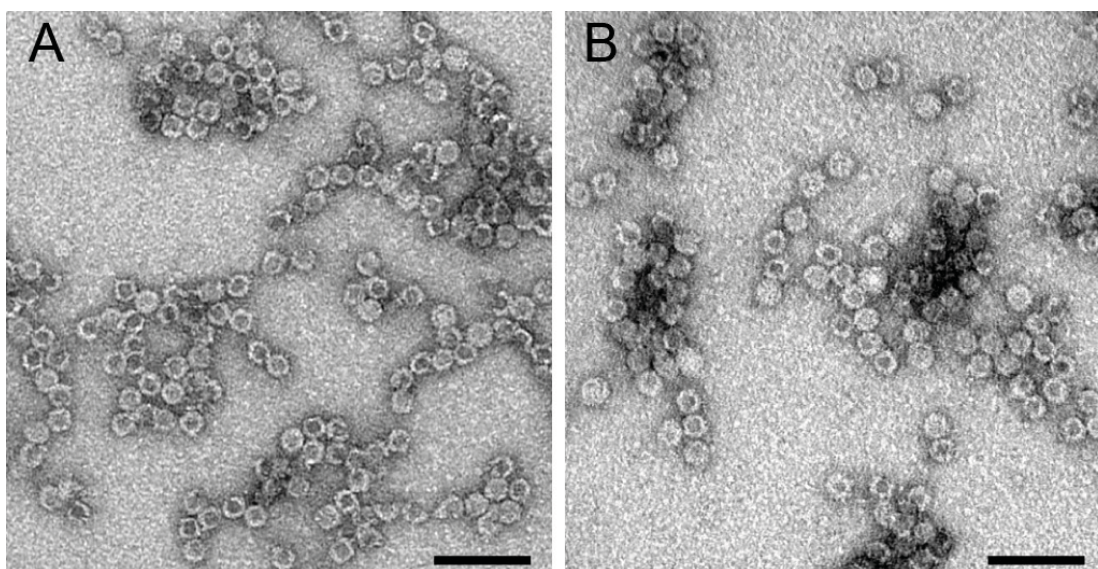
Figure 4.3: Representative high-resolution TEM images of the PIRL-ablated ferritin protein complexes and the un-ablated control, reproduced from Ref. [113] with permission. The ferritin protein complexes in the ablation plume (A) were collected during the PIRL ablation under DIVE condition from frozen aqueous solution directly onto TEM grids. The un-ablated ferritin protein complexes (B) were deposited directly from solution onto TEM grids. The scale bars represent 50 nm.

The rGFP samples collected directly from the ablation plume onto microscope slides exhibited fluorescence under a light microscope with an intensity comparable to that of the un-ablated control, which was deposited directly onto microscope slides, as shown in Fig. 4.4. The fluorescence emission spectra of rGFP collected directly from the ablation plume and the control rGFP deposited from solution onto microscope slides are shown in Fig. 4.5 (A). The spectra from both samples resulted in the characteristic emission maximum at the visible wavelength of 506 nm and the shoulder at 520 nm. Any changes in the protein structure would lead to shifts in the spectrum or even complete loss of fluorescence. No significant differences were observed between the fluorescence spectra of rGFP collected from the ablation plume and the un-ablated control under identical excitation conditions (488 nm). The spectra are in good

agreement with those previously reported [120] and demonstrate that the rGFP collected from the ablation plume remained functional.
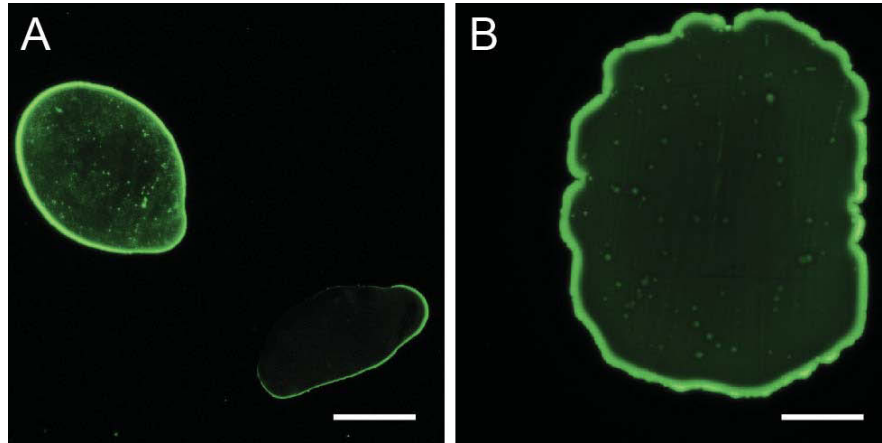
Figure 4.4: Representative fluorescence images of the PIRL-ablated rGFP and the control, reproduced from Ref. [113] with permission. The rGFP collected directly from the PIRL ablation under DIVE condition (A) and the un-ablated control (B) were deposited onto microscope slides. The images were acquired with an inverted light microscope. The scale bars represent $50\,\mu m$.
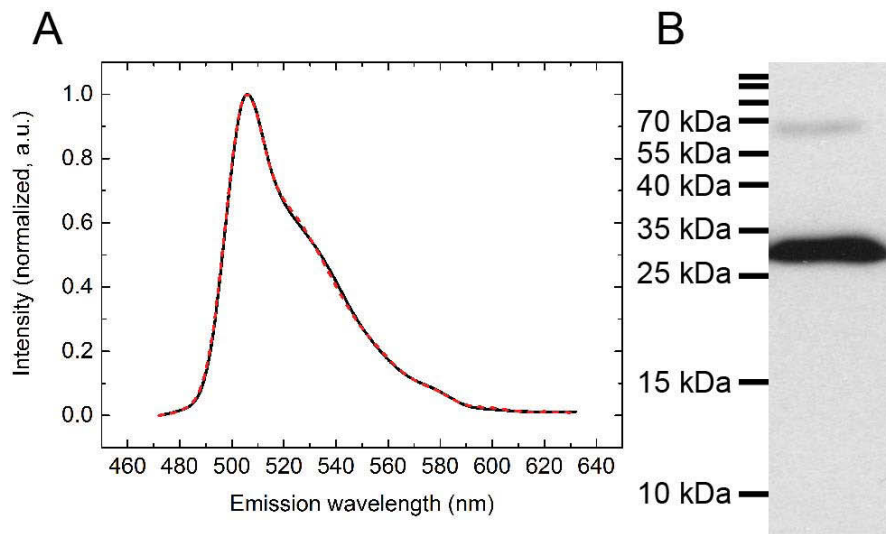
Figure 4.5: Characterization of rGFP integrity following the PIRL ablation under DIVE condition from frozen aqueous solution, reproduced from Ref. [113] with permission. Fluorescence emission spectra (A) were taken from rGFP collected from the ablation plume (black solid line) and the un-ablated control (red dash line). The excitation wavelength was 488 nm. The fluorescence intensity was normalized to unity individually for each curve. Cubic spline interpolation of 1024 points was applied separately to each curve. Western blot analysis (B) was performed on rGFP collected from the ablation plume. Two distinct bands were observed, one corresponding to the monomeric form of rGFP (26.9 kDa) and the other weaker band to the dimeric form (53.8 kDa).

The collected ablation plume from frozen aqueous solutions of rGFP was further examined by western blot analysis in order to investigate ablation-induced protein cleavage and degradation. Two distinct bands were observed, as shown in Fig. 4.5 (B), one band corresponding to the monomeric form (26.9 kDa) and the other weaker band corresponding to the dimeric form (53.8 kDa) of rGFP. No evidence of protein degradation, e.g. laddering or smearing, was observed in the blot. Hence, rGFP collected from the ablation plume did not undergo peptide cleavage or degradation through the PIRL ablation under DIVE condition.

Viruses

Representative TEM images, as shown in Fig. 4.6, present negatively stained TMV collected directly from the ablation plume onto TEM grids and the un-ablated TMV control sample deposited and dried onto TEM grids. TMV virions with characteristic widths of 18 nm and lengths equal to, or greater than, the individual TMV virion length, 300 nm, were observed in both the collected

ablation plume and the un-ablated control. Viral filaments with a maximum length of approximately $1.2\,\mu\mathrm{m}$ (4 virion units) were observed in the ablated samples, as shown in Fig. 4.6 (A). TEM images of the un-ablated control sample, as shown in Fig. 4.6 (B), contained a higher percentage of long viral filaments and an increase in the maximum virion filament length (approximately $2.4\,\mu\mathrm{m}$, 8 virion units), as compared to the collected ablated sample. An increase in the number of isolated single virions ($18\,\mathrm{nm} \times 300\,\mathrm{nm}$) was observed in the images of the collected ablated sample, compared to the un-ablated control. Damaged and truncated virions with a length of less than 300 nm were observed in the TEM images of the ablated samples and the un-ablated control with occurrences of $11\,\%$ and $12\,\%$, respectively, of the total number of viral particles observed. Therefore, virion destruction and truncation most likely occurred prior to ablation during sample purification and preparation but not during the PIRL ablation.
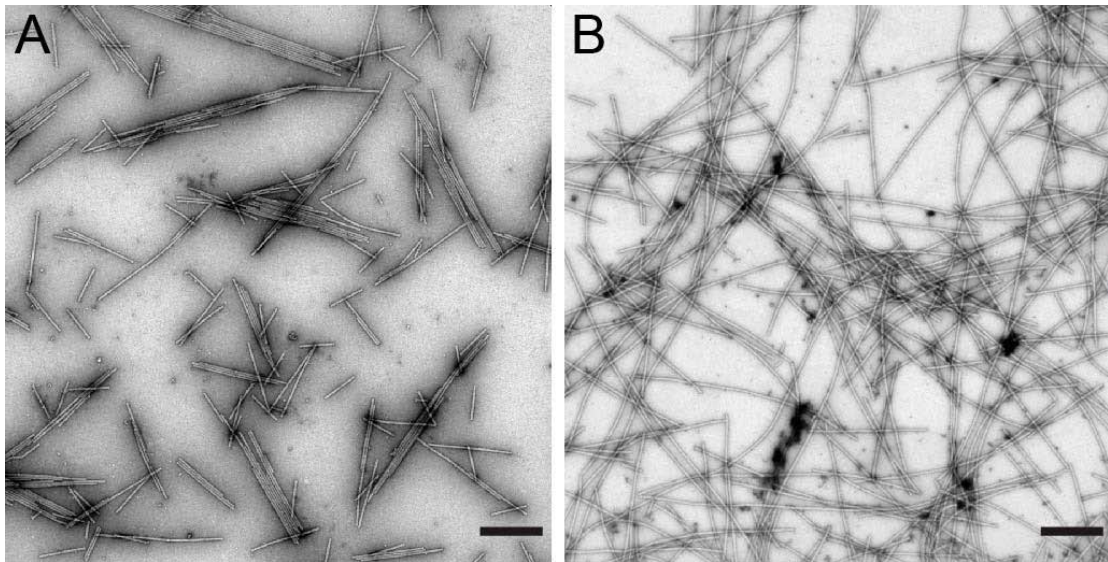
Figure 4.6: Representative high-resolution TEM images of the PIRL-ablated TMV and the un-ablated control, reproduced from Ref. [113] with permission. The TMV from the plume (A) during the PIRL ablation under DIVE condition from frozen aqueous solution were collected onto TEM grids. The un-ablated control (B) was deposited directly from solution onto TEM grids. The scale bars represent $500\,\mathrm{nm}$.

The viability of TMV following ablation was tested by inoculating the leaves of *Nicotiana glutinosa* L. with TMV collected from the ablation plume as described in the methods section. Lesions consistent with TMV infection were observed on the surface of the leaves, as shown in Fig. 4.7 (left), after incubation for 96 hours. A representative leaf of *Nicotiana glutinosa* L. inoculated

with only the corresponding phosphate buffer is shown in Fig. 4.7 (right). The collection efficiency of the ablation plume was estimated from the volumes of ablated and collected materials, together with the TMV concentrations before and after ablation calculated from optical extinction coefficient measurements. Over the ablation time of $720 \, \text{s}$, approximately $3.97 \, \text{mg}$ of TMV virions were ablated from frozen aqueous solution by the PIRL beam. Approximately $0.40 \, \text{mg}$ of TMV was collected from the ablation plume, which renders a plume collection efficiency of $10.08 \, \%$. A dose of $4 \, \mu\text{g}$ of TMV virions (dissolved in $20 \, \mu\text{l}$ aqueous solution) collected directly from the ablation plume were used to inoculate the leaves of *Nicotiana glutinosa* L. The TMV virions retained their ability to successfully colonize in tobacco leaves following the PIRL ablation and collection.
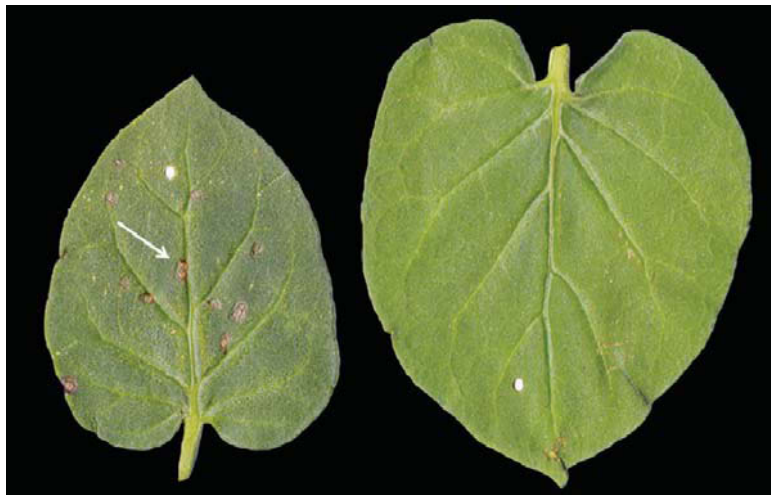
Figure 4.7: *Nicotiana glutinosa* L. leaves 96 hours post inoculation with TMV collected from the ablation plume (left leaf), reproduced from Ref. [113] with permission. The plume was produced by the PIRL ablation under DIVE condition from frozen aqueous solution of TMV. Several local lesions induced by the TMV infection can be observed on the left leaf 96 hours after the inoculation with the collected ablated TMV. The arrow points out one of the local lesions. The right leaf was inoculated only with the buffer and thus no lesion was observed.

The capability of the PIRL ablation to extract TMV from the natural environment was tested by the ablation of systematically infected tobacco leaves, as shown in Fig. 4.2. The ablation plume was collected and directly inoculated onto the leaves of *Nicotiana glutinosa* L. without any treatment. Lesions consistent with TMV infection were observed on the surface of the leaves inoculated with the collected plume, as shown in Fig. 4.8 (left), after incubation for 96 hours. A representative leaf of *Nicotiana glutinosa* L. inoculated with only

the corresponding phosphate buffer is shown in Fig. 4.8 (right). Therefore, the plume collected during the PIRL ablation of systematically infected tobacco leaves contained TMV with preserved biological activity.
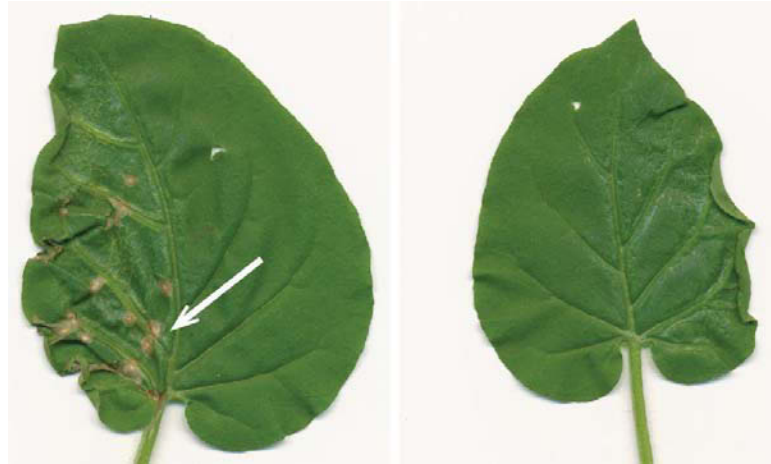
Figure 4.8: *Nicotiana glutinosa* L. leaves 96 hours post inoculation with TMV collected during the PIRL ablation of systematically infected tobacco leaves (left leaf), reproduced from Ref. [113] with permission. Several local lesions induced by the TMV infection can be observed on the left leaf 96 hours after the inoculation with in the collected ablation plume containing intact TMV. The arrow points out one of the local lesions. The right leaf was inoculated only with the buffer and thus no lesion was observed.

Cells

A representative confocal microscope image of *S. cerevisiae* cells collected directly from the ablation plume and stained with plasma membrane stain (Cell Mask orange) and DNA stain (DRAQ5, green) is shown in Fig. 4.9. The stains were selected in order to monitor the integrity of the cellular membrane and the DNA of the cells. Individual cells were dispersed across the collection surface, more than 70% of which retained a shape and size equivalent to viable *S. cerevisiae* cells. The DNA of these cells was also confined within intact cellular membranes, as shown in Fig. 4.9. Cells with ruptured cellular membranes were also observed in the collected ablation plume. The stained DNA of these cells was observed partially or completely outside the ruptured cellular membranes, as shown in Fig. 4.9.
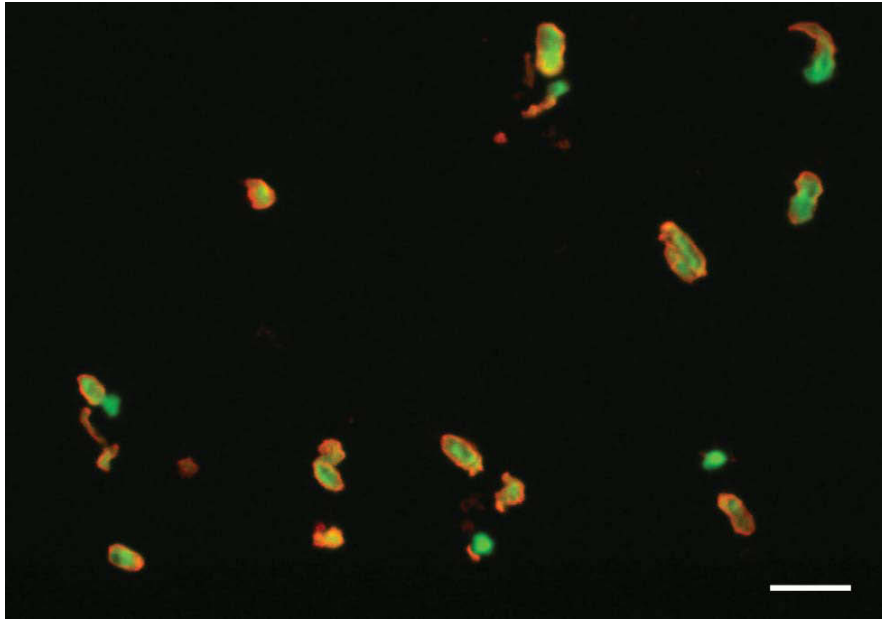
Figure 4.9: Representative image of *S. cerevisiae* cells collected from the ablation plume acquired with confocal microscope, reproduced from Ref. [113] with permission. Cell Mask orange plasma membrane stain was applied to the collected ablation plume in order to uniformly label the cell membranes. DRAQ5 DNA stain was applied to the collected ablation plume in order to stain DNA and nuclei of the cells. The scale bar represents $10\,\mu m$.

In order to test the viability of the *S. cerevisiae* cells following the PIRL ablation under DIVE condition, cells collected from the ablation plume were cultured on YEPD growth medium. The advanced colony development following $120\,h$ of incubation is shown in Fig. 4.10 (B). The representative light microscope image shows well developed colonies of S. cerevisiae cells which have expanded on the growth medium. A representative light microscope image of the intermediate state of colonization ($20\,h$ incubation) is shown in Fig. 4.10 (A). Therefore, *S. cerevisiae* cells collected directly from the ablation plume maintained not only their structural integrity but also their biological activity required to form and expand colonies. This observation indicates that the spatial gradients within the inhomogeneous distribution of water in the cells and the suspension generates gradients of forces on the length scale of the cells to wholly eject the cells from the suspension. Some cell rupture is however observed.
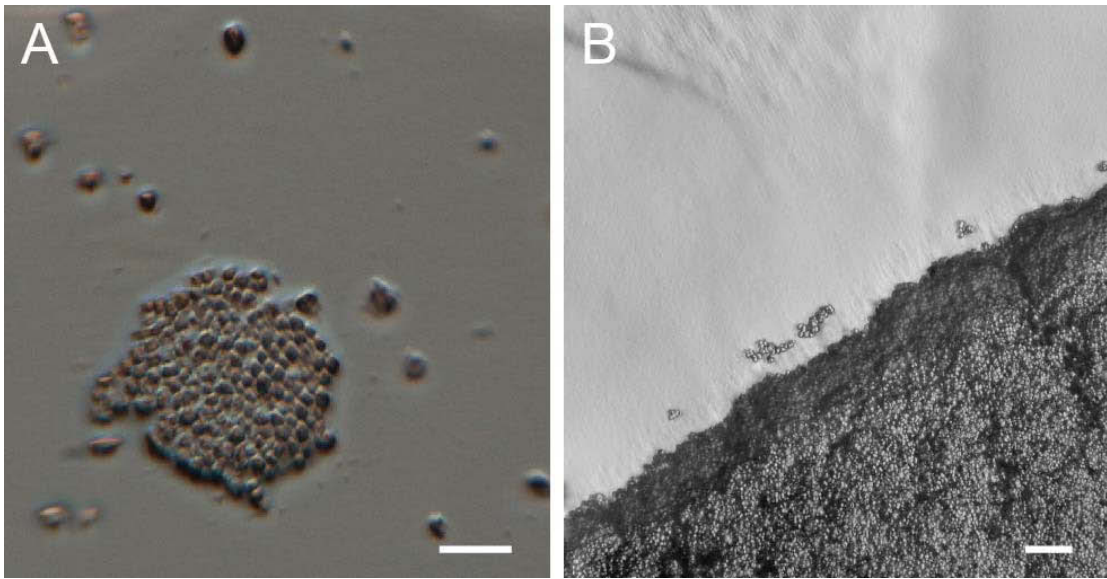
Figure 4.10: Colony development of *S. cerevisiae* cells collected directly from the ablation plume following 20 h (A) and 120 h (B) of incubation on YEPD growth medium, reproduced from Ref. [113] with permission. The scale bars represent 20 μm in (A) and 50 μm in (B).

Tyrolichus casei mites

Incomplete body parts of the *Tyrolichus casei* mites with the dimension of approximately 100 μm were observed in the ablation plume collected on the microscope glass slides. However, no complete *Tyrolichus casei* mites were observed in the collected ablation plume. In the un-ablated control sample, only a few *Tyrolichus casei* mites were dispersed in its matrix, a fraction of which were alive and in motion, and the rest were either not alive or even incomplete. The complete mites had a dimension of approximately 180 μm. The absence of complete *Tyrolichus casei* mites in the collected ablation plume can be attributed to two factors. One factor is the low occurrence of the *Tyrolichus casei* mites in the matrix obtained from the food-grade mite cheese. The other factor is the fact that the dimension of the complete *Tyrolichus casei* mites is larger than the transverse diameter of the PIRL beam and the spatial dimension of the forces generated within the inhomogeneous water distribution. Therefore, even if a complete *Tyrolichus casei* mite is irradiated by a pulse from the PIRL, due to the well confined deposition of the optical energy, it is likely that only the irradiated part of the *Tyrolichus casei* mite would be ablated and the unirradiated part remain in the suspension, leading to an incomplete *Tyrolichus casei* mite in the ablation plume. When it is necessary to apply the PIRL ablation to large

biological entities like the *Tyrolichus casei* mites, increasing the beam diameter and maintaining the optical density above the ablation threshold could be considered in order to obtain complete *Tyrolichus casei* mites in the ablation plume. However, the inhomogeneous water distribution within the organism will likely still lead to fragmentation of the organism.

4.3.2 Discussion

The structural integrity and function of several biological entities were shown to be retained through the PIRL ablation under DIVE condition.

The iron storage globular protein complex ferritin was used to examine the effect of the PIRL ablation under DIVE condition on protein structural integrity and oligomer adhesion. Ferritin complexes are composed of 24 subunits non-covalently bound to form a higher order structure capable of storing up to 4500 iron atoms in binding sites located near the center of the oligomer complex [121]. Intact ferritin complexes observed in TEM images of collected ablation plume were easily identified by their 6-sided toroidal structure, as shown in Fig. 4.3. The appearance and structural characteristics of the ablated protein complexes were nearly identical to the un-ablated control, with the average diameter of the collected ablated ferritin particles measured as 12.6 ± 0.6 nm, compared to 12.6 ± 0.8 nm measured for the un-ablated control. Ferritin, a large mass protein complex (approximately 440 kDa), maintained its morphological characteristics through the PIRL ablation, demonstrating the conservation of the individual protein structure. These results indicate that the DIVE-driven ablation is sufficiently gentle to maintain the protein-protein interactions indispensable for large protein oligomers to remain intact.

The fluorescence emission of rGFP was examined in order to determine the retention of protein function following the PIRL ablation. Comparison of the fluorescence emission spectra of rGFP collected from ablation plume and the un-ablated control, shown in Fig. 4.5 (A), provides an assessment of the rGFP structural integrity and functionality during and after the ablation process. Studies have shown that thermally or chemically denatured GFP is completely non-fluorescent [122]. GFP fluorescence is also sensitive to changes in the chromophore-protein interaction with mutations of a single amino acid at the chromophore binding site, causing significant shifts in the fluorescence emission spectra [123]. These findings demonstrate the fluorescence of GFP not only is strongly influenced by non-covalent interactions of the GFP chromophore with the protein interior, but also requires the intact protein structure. The fluorescence emission spectra of rGFP collected from the ablation

plume and the un-ablated control are virtually identical in form and emission maximum. This indicates that the GFP chromophore, a p-hydroxybenzylidene-imidazolinone [120], maintained its structure and binding coordination to the natively folded GFP protein throughout the ablation process. Thus, the PIRL ablation under DIVE condition of frozen rGFP solutions did not result in significant changes to the protein's structure and integrity, maintaining its chromophore binding capability required to fluoresce.

The western blot analysis of rGFP collected from the ablation plume, shown in Fig. 4.5 (B), demonstrates the absence of any observable fraction of protein degradation induced by the PIRL ablation under DIVE condition. The absence of laddering or smearing in the western blot indicates that the collected ablated rGFP were not cleaved or degraded and remained intact subsequent to the PIRL ablation under DIVE condition. Moreover, the protein's antibody binding motif remained chemically unaltered during the ablation process. The dimer complex [124, 125] was observed due to the brief denaturing conditions employed prior to electrophoresis and the resistance of rGFP to the denaturation induced by sodium dodecyl sulfate [126]. These results suggest that the PIRL ablation under DIVE condition would not lead to considerable alteration of the ablated protein's structure.

In addition to proteins and protein complexes, the effect of PIRL ablation for biological extraction was investigated on viruses using TMV as a viral model [127]. TEM imaging of the collected ablation plume, where the rod-like viral structure was resolved and identified, was used to compare the structural integrity of the viral particles following ablation with that of the un-ablated control. The TMV virions collected from the ablation plume maintained their morphological characteristics, as shown in Fig. 4.6. Further, the absence of an increase in the fraction of damaged or truncated virions observed in the TEM images of the collected ablated sample compared to the un-ablated control, 11 % and 12 %, respectively, confirms the ability of the PIRL ablation under DIVE condition to successfully extract intact viral particles. The collected ablated TMV samples showed a decrease in the number and maximum length of viral filaments which were formed from the stacking of individual virions [128], and an increase in the number of single isolated virions compared to the un-ablated control. Due to the lack of an increase in the number of damaged or truncated individual virions in the ablated sample, the smaller viral filaments and increased number of individual virions presumably originated from larger filaments which were separated at the stacking sites. Two factors possibly contributed to this effect. One factor is that the maximum length of the

viral filaments (2.4 μm) is on the order of the depth of the ablation volume of a single PIRL pulse (on the few micrometer scale). The other factor is the forces on the filaments during the plume collection. Although a number of long viral filaments were partially unstacked into short filaments or individual virions, no increase in damage was observed on the individual virions or viral particles following the ablation and collection process. This observation indicates that the complete genome was preserved for the virions with lengths equal to, or greater than, 300 nm [129], and is supported from the fact that these virions retained the ability to infect a host [127].

The biological activity of the virions collected from the ablation plume was evaluated by inoculating the leaves of *Nicotiana glutinosa* L. with the collected ablation plume of TMV. The lesions shown in Fig. 4.7 on the leaves of *Nicotiana glutinosa* L. after inoculation of TMV collected from the ablation plume verify that the TMV virions maintained their biological activity and were infectious following PIRL ablation process. TMV preserved its structural integrity and biological activity throughout the PIRL ablation under DIVE condition, indicating that it is an effective method for the extraction of intact, biologically active infectious agents. As a step further, the TMV extracted by the PIRL ablation from systematically infected tobacco leaves maintained the infectivity as shown in Fig. 4.8. Therefore, this simple, direct and effective extraction method with the PIRL ablation is applicable to biological entities not only in solutions but also in the natural environment.

Furthermore, living *S. cerevisiae* cells were used as a model to investigate the effect of the PIRL ablation under DIVE condition on the structural integrity and biological activity of complete cells. *S. cerevisiae* cells with intact cellular membranes and DNA well confined therein were observed in the confocal microscope images of the collected ablation plume, shown in Fig. 4.9, demonstrating that cells retain their structural integrity and remain intact following the PIRL ablation. *S. cerevisiae* cells with incomplete cell membranes and intracellular contents released were also observed in the confocal microscope images. A factor that might contribute to cellular damage is the large size of the cells (approximately 10 μm) compared to the ablation depth (approximately 1 μm to 10 μm range) which would result in damaged cells located at the borders of ablation volume. In addition, water excited within the cell may also be of sufficient force to cause rupture. Evidently, the much higher water content of the cell suspension in relation to the intracellular water helped to mitigate this to the point that intact cells could be observed in the ablation process. More of the absorbed energy would be in the water surrounding the cell and the spa-

tial gradient defining the ablation process extends over the dimensions of the cell to drive the cell into the gas phase intact. It is noticed that cellular damage might also occur during the plume collection. The intracellular contents released from the cells could potentially be used for downstream analysis.

The biological activity of *S. cerevisiae* cells following the PIRL ablation was assessed by the incubation of the ablation plume collected on YEPD growth medium. The viability of the *S. cerevisiae* cells was confirmed by their proliferation following the PIRL ablation with colonies forming and expanding over the incubation time, as shown in Fig. 4.10. Therefore, the cellular model system, *S. cerevisiae* cells, maintained its structural integrity and biological activity through the PIRL ablation and plume collection.

4.4 High potency of DIVE in biodiagnosis

The application of the PIRL ablation under DIVE condition to biological entities has been shown to be a simple, direct and effective method for their extraction. The results demonstrate that this technique is capable of extracting the biological entities, i.e. proteins, protein complexes, viruses and cells, with conserved biological characteristics, integrity, function and activity. The PIRL ablation under DIVE condition does not significantly induce thermal or mechanical damage to the biological entities examined. This advance minimizes time and effort required by conventional extraction methods and can potentially lead to novel high speed extraction processes without mechanical intervention.

While the conventional laser-based extraction methods typically excise a macroscopic region of interest to ensure sufficient quantity of intact material, the ablation plume from each PIRL pulse can be utilized directly for analysis and diagnosis of volumes approaching that of single cells. The intact nature of the plume composition and micrometer scale ablation depths minimize the amount of biological material required for extraction.

Given the successful use of the PIRL ablation in surgical applications with minimal collateral tissue damage [8, 11, 12, 14, 16, 17] and the results concerning the absence of degradation to proteins extracted from tissues for mass spectrometry [61], this novel laser extraction method has the potential to bring substantial advances to biological diagnosis. The minimized collateral tissue damage [8] associated with the PIRL ablation equips the technique specifically well for biopsies with reduced healing time and inflammatory response [8, 101, 102, 104].

In addition, the PIRL ablation offers a higher spatial resolution of biopsied

areas compared to conventional biopsy methods using fine needle aspiration. While the same ablation mechanism can in principle be utilized down to the diffraction limit of the focal spot around $3\,\mu m$, the focal diameter of the PIRL beam employed in this study (approximately $130\,\mu m$) is already significantly smaller than the inner diameter of the finest needle typically used (Gauge 25, $260\,\mu m$) [130]. Furthermore, the PIRL radiation is absorbed approximately within $1\,\mu m$ to $10\,\mu m$ under the present ablation conditions. This depth of resolution would permit increased precision in biopsy depth, down to the level of a single cell.

Laser extraction with the PIRL could also be applied to situations where there is currently no biopsy available or to areas that have strong reactions to mechanical biopsy, for example, viral, bacterial or parasitic infections in brain [131] and nerve [132], or amyloid plaque [133] sampling in the brain.

Future applications could extend the advantages of this technique to instantaneous analysis of intact and functional biological entities extracted by the PIRL ablation. An example would be the ablation plume of fluorescently labeled biological entities being analyzed instantaneously upon collection with fluorescence measurements for high speed sampling at kHz rates and higher, with higher laser repetition and beam rastering, as demonstrated by the experiment with rGFP. In the case of epidemic and pandemic characterizations, the PIRL ablation could be utilized to probe traces of contagious agents from hosts and the collected ablation plume could be used directly for examination and diagnosis.

Simply stated, the PIRL ablation under DIVE condition is a direct and simple method to extract biological entities with preservation of their biological integrity and activity. Not limited to its potential as an instantaneous tool with micrometer precision for biopsy, the PIRL ablation under DIVE condition will bring promising benefits to biological diagnosis and disease control.

5 Conclusions and outlook

New technologies are called for by two urging demands in medical practice amongst many others. One demand is precise surgery at the cellular level with preservation of tissue boundaries. The other demand is rapid large-volume analysis and diagnosis in health management. For these demands, the studies in this dissertation utilize the combination of fundamental physics research and laser technology with clinical and biophysical evaluation. This combination is directed to a technique optimized for the ablation of biological samples out of water rich environments with minimal damage to collateral tissues. The PIRL ablation under DIVE condition selectively excites the vibrational modes of the water molecule, which acts as a propellant. Thus, in water rich environments, the constituent biological complexes are propelled to the gas phase on the fastest impulsive limit for ablation. In this process, not only excessive thermal heating of the biomolecules is avoided, but also multiphoton ionization and degradation of the sample integrity are avoided by using strongly resonant 1-photon conditions. In this dissertation, the successful applications of the PIRL ablation in surgery, biological analysis, and diagnosis are demonstrated in three aspects. First, the PIRL ablation serves as a precise scalpel for various ocular tissues with minimal collateral damage. Second, chemical analytical methods, especially mass spectrometry, verify that proteins of various species and in large abundance can be extracted by the PIRL and that fragmentation and other chemical changes are absent in this process. Third, the PIRL ablation is capable of extracting structurally and functionally intact biological entities, including proteins, protein complexes, viruses and cells, directly from aqueous samples and the natural environment.

As a precise scalpel, the PIRL ablation delivers, for the first time, well-controlled and reproducible incisions at cornea, sclera, trabecular meshwork, iris, lens and retina. Examined with high resolution microscope imaging and histological analysis, the neat incisions performed by the PIRL exhibit well defined boundaries and preserved collagen fibrils neighboring the ablation site, with minimized thermal damage on the single cell level. Further characteriza-

tions of PIRL ablation at the cornea show that the relatively small temperature rise during the ablation does not exceed the physiological range, and that the ablation depth within the corneal stroma is proportional to the ablation time span. Thus, the PIRL ablation is demonstrated as a suitable tool for contact-free and applanation-free corneal trephination, which is advantageous compared to the commercialized laser solutions. Moreover, the successful incisions at cornea, normal and pathologically altered, and the other five types of ocular tissues, indicate the potential of the PIRL ablation as a versatile solution in various surgical scenarios of ophthalmology.

One step beyond the surgical application of the PIRL ablation is to better understand the constituent proteins in the ablation plume. Mass spectrometry and other chemical analyses are employed to examine the proteins ablated by the PIRL from tissues and solutions. Proteins, with masses from tens of kDa to hundreds of kDa, are present in significant amounts in the ablation plume of mouse muscle tissue. No sample specific requirement is imposed by the PIRL ablation. The comparison of mass spectra of the ablated RNase A and the un-ablated control verifies the absence of fragmentation and other chemical changes during the ablation process. In addition, mass spectra of the incubation results of the ablated trypsin and human plasma serum show that the enzymatic activities of the corresponding proteins are maintained following the ablation process. Therefore, the PIRL ablation can be utilized to introduce biological samples to analyses in mass spectrometry. The combination of the PIRL ablation, a soft ionization technique and a mass spectrometer can ensure the production of molecular ions and the absence of fragmentation. Since the DIVE process is compatible with *in situ* and *in vivo* conditions, such a combination can be applied to research in proteomics, for example tissue imaging, with the analytes including but not limited to proteins, peptides, drug metabolites and lipids.

As sample extraction is the first and essential step for many analytical procedures, the major innovation and first-time feature of this work is the demonstration of the conserved higher order structure and characteristic activity of the biological entities extracted by the PIRL ablation. The significant conclusion in this aspect, supported by high resolution microscope imaging down to single molecule and extensive biochemical analysis, is that biological complexes ablated with the PIRL under DIVE condition are structurally and functionally intact, with even TMV viruses and *S. cerevisiae* cells retaining the ability to infect and colonize. Therefore, this laser extraction method is suitable for various types of samples, from proteins like rGFP to cells like *S. cerevisiae*, and can be

applied to a wide range of analysis and evaluation techniques beyond those reported in Chap. 4. The minimal damage to molecular complexes in the ablation plume and surrounding tissue coupled with the micrometer precision of the laser ablation opens the door for the development of novel, high speed, non-contact extraction techniques with single cell precision. Not limited to biological samples in laboratorial or natural environments, this laser extraction technique is particularly timely due to its potential to transform chemical analysis, biodiagnosis and disease control.

The life cycle and the water cycle are one. As Jacques Cousteau warned, it is a fact not to be forgotten. Interestingly, this fact is also intertwined in the studies of this dissertation. Water is the central hub that connects the physical apparatus, the biological samples and the physics in the background. This inspiring fact will surely compel further research to better understand water, life and nature.

List of Figures

List of Tables

Bibliography

[1] I. N. Levine, *Molecular Spectroscopy*, John Wiley & Sons, Inc., USA (1975). 1, 62

[2] M. L. Cowan, B. D. Bruner, N. Huse, J. R. Dwyer, B. Chugh, E. T. J. Nibbering, T. Elsaesser, and R. J. D. Miller, *Ultrafast memory loss and energy redistribution in the hydrogen bond network of liquid H_2O*, Nature **434**, 199 (2005). 1, 8

[3] K. Franjic, M. L. Cowan, D. Kraemer, and R. J. D. Miller, *Laser selective cutting of biological tissues by impulsive heat deposition through ultrafast vibrational excitations*, Optics Express **17**, 22937 (2009). 1, 5, 7, 8, 59

[4] K. Franjic and R. J. D. Miller, *Vibrationally excited ultrafast thermodynamic phase transitions at the water/air interface*, Physical Chemistry Chemical Physics **12**, 5225 (2010). 1, 5, 8

[5] J. Lindner, P. Vöhringer, M. S. Pshenichnikov, D. Cringus, D. A. Wiersma, and M. Mostovoy, *Vibrational relaxation of pure liquid water*, Chemical Physics Letters **421**, 329 (2006). 1

[6] R. J. D. Miller, *Vibrational energy relaxation and structural dynamics of heme proteins*, Annu. Rev. Phys. Chem **42**, 581 (1991). 1

[7] K. L. Vodopyanov, *Saturation studies of H_2O and HDO near 3400 cm^{-1} using intense picosecond laser pulses*, The Journal of Chemical Physics **94**, 5389 (1991). 2

[8] S. Amini-Nik, D. Kraemer, M. L. Cowan, K. Gunaratne, P. Nadesan, B. A. Alman, R. J. D. Miller, and M. Polymenis, *Ultrafast mid-IR laser scalpel: protein signals of the fundamental limits to minimally invasive surgery*, PLOS ONE **5**, e13053 (2010). 3, 8, 62, 81

[9] A. Vogel and V. Venugopalan, *Mechanisms of Pulsed Laser Ablation of Biological Tissues*, Chemical Reviews **103**, 577 (2003). 3, 5, 6, 7, 27, 62

[10] G. M. Hale and M. R. Querry, *Optical Constants of Water in the $200 - nm$ to $200 - \mu m$ Wavelength Region*, Applied Optics **12**, 555 (1973). 3, 27, 62

[11] M. Hess, M. D. Hildebrandt, F. Müller, S. Kruber, P. Krötz, U. Schumacher, R. Reimer, M. Kammal, K. Püschel, W. Wöllmer, and R. J. D. Miller, *Picosecond infrared laser (PIRL): an ideal phonomicrosurgical laser?*, European Archives of Oto-Rhino-Laryngology **270**, 2927 (2013). 3, 16, 21, 81

[12] A. Böttcher, T. S. Clauditz, R. Knecht, S. Kucher, W. Wöllmer, W. Wilczak, P. Krötz, N. Jowett, C. V. Dalchow, A. Münscher, and R. J. D. Miller, *A novel tool in laryngeal surgery: Preliminary results of the picosecond infrared laser*, The Laryngoscope **123**, 2770 (2013). 3, 16, 21, 81

[13] A. Böttcher, S. Kucher, R. Knecht, N. Jowett, P. Krötz, R. Reimer, U. Schumacher, S. Anders, A. Münscher, C. V. Dalchow, and R. J. D. Miller, *Reduction of thermocoagulative injury via use of a picosecond infrared laser (PIRL) in laryngeal tissues*, European Archives of Oto-Rhino-Laryngology (2015). 3, 16, 21, 24

[14] N. Jowett, W. Wöllmer, A. M. Mlznarek, P. Wiseman, B. Segal, K. Franjic, P. Krötz, A. Böttcher, R. Knecht, and R. J. D. Miller, *Heat Generation During Ablation of Porcine Skin With Erbium:YAG Laser vs a Novel Picosecond Infrared Laser*, JAMA Otolaryngol Head Neck Surg. **139**, 828 (2013). 3, 16, 24, 81

[15] N. Jowett, W. Wollmer, R. Reimer, J. Zustin, U. Schumacher, P. W. Wiseman, A. M. Mlynarek, A. Bottcher, C. V. Dalchow, B. B. Lorincz, R. Knecht, and R. J. D. Miller, *Bone Ablation without Thermal or Acoustic Mechanical Injury via a Novel Picosecond Infrared Laser (PIRL)*, Otolaryngology – Head and Neck Surgery **150**, 385 (2014). 3, 16, 21, 24

[16] S. J. Linke, L. Ren, A. Frings, J. Steinberg, W. Wöllmer, T. Katz, R. Reimer, N.-O. Hansen, N. Jowett, G. Richard, and R. J. D. Miller, *Perspektiven der laserassistierten Keratoplastik: Eine aktuelle Übersicht und erste experimentelle Erfahrungen mit dem Pikosekundeninfrarotlaser ($\lambda = 3\mu m$)*, Der Ophthalmologe **111**, 523 (2014). 3, 9, 29, 81, 107

[17] S. J. Linke, A. Frings, L. Ren, A. Gomolka, U. Schumacher, R. Reimer, N.-O. Hansen, N. Jowett, G. Richard, R. J. D. Miller, and R. R. Mohan, *A New Technology for Applanation Free Corneal Trephination: The Picosecond Infrared Laser (PIRL)*, PLOS ONE **10**, e0120944 (2015). 3, 9, 29, 81, 107

[18] M. H. Niemz, *Laser-Tissue Interactions: Fundamentals and Applications*, Springer-Verlag Berlin Heidelberg, third, enlarged edn. (2003). 3, 4, 5, 6, 7, 9, 10, 11, 12, 13, 14, 16, 32

[19] J.-L. Boulnois, *Photophysical processes in recent medical laser developments: A review*, Lasers in Medical Science **1**, 47 (1986). 3, 5

[20] T. J. Dougherty, C. J. Gomer, B. W. Henderson, G. Jori, D. Kessel, M. Korbelik, J. Moan, and Q. Peng, *Photodynamic Therapy*, JNCI Journal of the National Cancer Institute **90**, 889 (1998). 4

[21] J. Moan, L. Ma, V. Iani, and A. Juzeniene, *Influence of Light Exposure on the Kinetics of Protoporphyrin IX Formation in Normal Skin of Hairless Mice After Application of 5-Aminolevulinic Acid Methyl Ester*, Journal of Investigative Dermatology **125**, 1039 (2005). 5

[22] A. Vogel, J. Noack, G. Hüttman, and G. Paltauf, *Mechanisms of femtosecond laser nanosurgery of cells and tissues*, Applied Physics B **81**, 1015 (2005). 6

[23] B. Girard, M. Cloutier, D. Wilson, C. Clokie, R. J. D. Miller, and B. Wilson, *Microtomographic analysis of healing of femtosecond laser bone calvarial wounds compared to mechanical instruments in mice with and without application of BMP-7*, Lasers in Surgery and Medicine **39**, 458 (2007). 7

[24] D. Kraemer, M. L. Cowan, A. Paarmann, N. Huse, E. T. J. Nibbering, T. Elsaesser, and R. J. D. Miller, *Temperature dependence of the two-dimensional infrared spectrum of liquid H_2O*, Proceedings of the National Academy of Sciences **105**, 437 (2008). 8

[25] H. S. Dua, L. A. Faraj, D. G. Said, T. Gray, and J. Lowe, *Human Corneal Anatomy Redefined*, Ophthalmology **120**, 1778 (2013). 9

[26] D. M. Maurice, *The Cornea and Sclera*, in H. Davson (ed.), *The Eye*, 1–158, Academic Press, New York and NY (1984). 10, 12, 27

[27] S. R. Waltman, *The Cornea*, in Moses R. A. (ed.), *Adler's Physiology of the Eye: Clinical Application*, 38–62, CV Mosby, St. Louis (1981). 10

[28] J. M. Krauss, C. A. Puliafito, and R. F. Steinert, *Laser interactions with the cornea*, Survey of Ophthalmology **31**, 37 (1986). 10, 11

[29] B. Seitz, A. Langenbucher, M. M. Kus, M. Küchle, and G. O. Naumann, *Nonmechanical corneal trephination with the excimer laser improves outcome after penetrating keratoplasty*, Ophthalmology **106**, 1156 (1999). 10, 28, 29

[30] M. Farid and R. F. Steinert, *Femtosecond laser-assisted corneal surgery*, Current Opinion in Ophthalmology **21**, 288 (2010). 10

[31] F. Birnbaum, P. Maier, and T. Reinhard, *Perspectives of femtosecond laser-assisted keratoplasty*, Der Ophthalmologe **108**, 807 (2011). 10, 28

[32] C. Crotti, F. Deloison, F. Alahyane, F. Aptel, L. Kowalczuk, J.-M. Legeais, D. A. Peyrot, M. Savoldelli, and K. Plamann, *Wavelength Optimization in Femtosecond Laser Corneal Surgery*, Investigative Ophthalmology & Visual Science **54**, 3340 (2013). 11, 28, 29

[33] J. Marshall and D. H. Sliney, *Endoexcimer laser intraocular ablative photodecomposition*, American Journal of Ophthalmology **101**, 130 (1986). 11

[34] S. L. Trokel, R. Srinivasan, and B. Braren, *Excimer laser surgery of the cornea*, American Journal of Ophthalmology **96**, 710 (1983). 11

[35] J. Marshall, S. Trokel, S. Rothery, and R. R. Krueger, *A comparative study of corneal incisions induced by diamond and steel knives and two ultraviolet radiations from an excimer laser*, British Journal of Ophthalmology **70**, 482 (1986). 11

[36] M. Kerr-Muir, S. L. Trokel, J. Marshall, and S. Rothery, *Ultrastructural comparison of conventional surgical and argon fluoride excimer laser keratectomy*, American Journal of Ophthalmology **103**, 448 (1987). 11

[37] S. Tuft, R. W. Zabel, and J. Marshall, *Corneal Repair following Kerotectomy: Comparison between Conventional Surgery and Laser Photoablation*, Investigative Ophthalmology & Visual Science **30**, 1769 (1989). 11

[38] T. Møller-Pedersen, H. D. Cavanagh, W. M. Petroll, and J. V. Jester, *Stromal wound healing explains refractive instability and haze development after photorefractive keratectomy: A 1-year confocal microscopic study*, Ophthalmology **107**, 1235 (2000). 11

[39] M. Vengris, E. Gabryte, A. Aleknavicius, M. Barkauskas, O. Ruksenas, A. Vaiceliunaite, and R. Danielius, *Corneal shaping and ablation of transparent media by femtosecond pulses in deep ultraviolet range*, Journal of Cataract & Refractive Surgery **36**, 1579 (2010). 11, 12

[40] P. P. van Saarloos and J. Rodger, *Histological changes and unscheduled DNA synthesis in the rabbit cornea following 213-nm, 193-nm, and 266-nm irradiation*, Journal of Refractive Surgery **23**, 477 (2007). 11, 12

[41] X. H. Hu and T. Juhasz, *Study of corneal ablation with picosecond laser pulses at 211 nm and 263 nm*, Lasers in Surgery and Medicine **18**, 373 (1996). 12

[42] D. P. Piñero, R. J. Pérez-Cambrodí, A. Gómez-Hurtado, F. J. Blanes-Mompó, and A. Alzamora-Rodríguez, *Results of laser in situ keratomileusis performed using solid-state laser technology*, Journal of Cataract & Refractive Surgery **38**, 437 (2012). 12

[43] H. A. Quigley, *Open-angle glaucoma*, New England Journal of Medicine **328**, 1097 (1993). 12

[44] W. F. March, T. Gherezghiher, M. C. Koss, R. P. Shaver, W. D. Heath, and R. D. Nordquist, *Histologic Study of a Neodymium-YAG Laser Sclerostomy*, Archives of Ophthalmology **103**, 860 (1985). 12

[45] J. Marshall and A. C. Bird, *A comparative histopathological study of argon and krypton laser irradiations of the human retina*, British Journal of Ophthalmology **63**, 657 (1979). 13

[46] World Medical Association, *Declaration of Helsinki*. 17

[47] R. Hibst and U. Keller, *Experimental studies of the application of the Er:YAG laser on dental hard substances: I. Measurement of the ablation rate*, Lasers in Surgery and Medicine **9**, 338 (1989). 27

[48] Z.-Z. Li, J. E. Code, and W. P. van de Merwe, *Er:YAG laser ablation of enamel and dentin of human teeth: Determination of ablation rates at various fluences and pulse repetition rates*, Lasers in Surgery and Medicine **12**, 625 (1992). 27

[49] B. N. Chichkov, C. Momma, S. Nolte, F. Alvensleben, and A. Tünnermann, *Femtosecond, picosecond and nanosecond laser ablation of solids*, Applied Physics A Materials Science & Processing **63**, 109 (1996). 27

[50] B. Jean, *Three years of biomedical FEL use in medicine and surgery How far have we come?* Nuclear Instruments and Methods in Physics Research Section A: Accelerators, Spectrometers, Detectors and Associated Equipment **393**, 540 (1997). 27

[51] H. D. Downing and D. Williams, *Optical constants of water in the infrared*, Journal of Geophysical Research **80**, 1656 (1975). 27

[52] G. K. Lang, E. Schroeder, J. W. Koch, M. Yanoff, and G. O. Naumann, *Excimer laser keratoplasty part 1: basic concepts*, Ophthalmic Surgery **20**, 262 (1989). 28

[53] R. F. Steinert, T. S. Ignacio, and M. A. Sarayba, *"Top Hat"–Shaped Penetrating Keratoplasty Using the Femtosecond Laser*, American Journal of Ophthalmology **143**, 689 (2007). 28

[54] K. Plamann, F. Aptel, C. L. Arnold, A. Courjaud, C. Crotti, F. Deloison, F. Druon, P. Georges, M. Hanna, J.-M. Legeais, F. Morin, É. Mottay, V. Nuzzo, D. A. Peyrot, and M. Savoldelli, *Ultrashort pulse laser surgery of the cornea and the sclera*, Journal of Optics **12**, 084002 (2010). 28, 29

[55] F. Birnbaum, A. Wiggermann, P. C. Maier, D. Böhringer, and T. Reinhard, *Clinical results of 123 femtosecond laser-assisted penetrating keratoplasties*, Graefe's Archive for Clinical and Experimental Ophthalmology **251**, 95 (2013). 28, 29

[56] H. K. Soong and J. B. Malta, *Femtosecond Lasers in Ophthalmology*, American Journal of Ophthalmology **147**, 189 (2009). 29

[57] M. Ostertag, R. Walker, T. Bende, and B. J. Jean, *Optimizing photoablation parameters in the mid IR: predictive model for the description of experimental data*, in S. L. Jacques (ed.), *Proceedings of SPIE*, vol. 2391, 138–149 (1995). 30

[58] R. Walker, M. Ostertag, A. F. G. van der Meer, T. Bende, K. C. Schmiedt, and B. J. Jean, *Photoablation with the free-electron laser between 10 and 15 um in biological soft tissue (cornea)*, Journal of Biomedical Optics **2**, 204 (1997). 30

[59] K. M. Joos, G. S. Edwards, J.-H. Shen, D. J. Shetlar, R. D. Robinson, and D. M. O'Day, *Free electron laser (FEL) laser-tissue interaction with human cornea and optic nerve*, in J.-M. A. Parel, K. M. Joos, and P. O. Rol (eds.), *Proceedings of SPIE*, vol. 2673, 89–92 (1996). 30

[60] J. T. Watson and O. D. Sparkman, *Introduction to Mass Spectrometry: Instrumentation, Applications and Strategies for Data Interpretation*, John Wiley & Sons, Inc., 4 edn. (2008). 35, 36, 37, 38, 39, 40, 41, 42, 43, 44, 45

[61] M. Kwiatkowski, M. Wurlitzer, M. Omide, L. Ren, S. Kruber, R. Nimer, W. D. Robertson, A. Horst, R. J. D. Miller, and H. Schlüter, *Ultrafast ex-*

traction of proteins from tissues using desorption by impulsive vibrational excitation, Angewandte Chemie International Edition **54**, 285 (2015). 35, 52, 55, 56, 81, 107

[62] H. Schlüter, *Mass Spectrometric Proteomics*, lecture series at University Medical Center Hamburg-Eppendorf, Hamburg, Germany (2012). 36, 38, 39, 40, 41, 42, 43, 44, 45

[63] S. E. Van Bramer, *An introduction to mass spectrometry*, last access on July 6th 2015 at `http://science.widener.edu/svb/massspec/massspec.pdf` (1997). 36, 37, 38, 39, 40, 41, 43, 44, 45

[64] D. C. Harris, *Quantitative Chemical Analysis*, W. H. Freeman and Company, New York and NY, 8 edn. (2010). 36

[65] L. He (ed.), *Mass Spectrometry Imaging of Small Molecules*, Humana Press, Ebook (2015). 36

[66] M. Barkovich, *High performance liquid chromatography*, last access on July 6th 2015 at `http://chemwiki.ucdavis.edu/Analytical_Chemistry/Instrumental_Analysis/Chromatography/High_performance_liquid_chromatography`. 37

[67] Waters GmbH, *How Does High Performance Liquid Chromatography Work?* last access on July 6th 2015 at `http://www.waters.com/waters/de_DE/How-Does-High-Performance-Liquid-Chromatography-Work%3F/nav.htm?cid=10049055&locale=de_DE`. 37

[68] J. J. Pitt, *Principles and Applications of Liquid Chromatography-Mass Spectrometry in Clinical Biochemistry*, Clinical Biochemist Reviews **30**, 19 (2009). 37

[69] H. Hauser, *Some aspects of the phase behaviour of charged lipids*, Biochimica et Biophysica Acta (BBA) - Biomembranes **772**, 37 (1984). 37

[70] A. Abe and J. A. Shayman, *The role of negatively charged lipids in lysosomal phospholipase A2 function*, Journal of Lipid Research **50**, 2027 (2009). 37

[71] R. E. Banks, M. J. Dunn, D. F. Hochstrasser, J.-C. Sanchez, W. Blackstock, D. J. Pappin, and P. J. Selby, *Proteomics: new perspectives, new biomedical opportunities*, The Lancet **356**, 1749 (2000). 45

[72] R. Aebersold, *A mass spectrometric journey into protein and proteome research*, Journal of the American Society for Mass Spectrometry **14**, 685 (2003). 45

[73] R. Aebersold and M. Mann, *Mass spectrometry-based proteomics*, Nature **422**, 198 (2003). 45

[74] N. Dyballa and S. Metzger, *Fast and Sensitive Colloidal Coomassie G-250 Staining for Proteins in Polyacrylamide Gels*, Journal of Visualized Experiments (2009). 49

[75] A. Quaas, A. S. Bahar, K. v. Loga, A. S. Seddiqi, J. M. Singer, M. Omidi, O. Kraus, M. Kwiatkowski, M. Trusch, S. Minner, E. Burandt, P. Stahl, W. Wilczak, M. Wurlitzer, R. Simon, G. Sauter, A. Marx, and H. Schlüter, *MALDI imaging on large–scale tissue microarrays identifies molecular features associated with tumour phenotype in oesophageal cancer*, Histopathology **63**, 455 (2013). 49

[76] K. K. Murray, R. K. Boyd, M. N. Eberlin, G. J. Langley, L. Li, and Y. Naito, *Definitions of terms relating to mass spectrometry (IUPAC Recommendations 2013)*, Pure and Applied Chemistry **85** (2013). 52, 55

[77] D. Hildebrand, P. Merkel, L. F. Eggers, and H. Schlüter, *Proteolytic Processing of Angiotensin-I in Human Blood Plasma*, PLOS ONE **8**, e64027 (2013). 55

[78] P. Nemes, A. A. Barton, Y. Li, and A. Vertes, *Ambient molecular imaging and depth profiling of live tissue by infrared laser ablation electrospray ionization mass spectrometry*, Analytical Chemistry **80**, 4575 (2008). 58, 59

[79] R. G. Cooks, Z. Ouyang, Z. Takáts, and J. M. Wiseman, *Ambient Mass Spectrometry*, Science **311**, 1566 (2006). 58

[80] L. S. Eberlin, I. Norton, D. Orringer, I. F. Dunn, X. Liu, J. L. Ide, A. K. Jarmusch, K. L. Ligon, F. A. Jolesz, A. J. Golby, S. Santagata, N. Y. R. Agar, and R. G. Cooks, *Ambient mass spectrometry for the intraoperative molecular diagnosis of human brain tumors*, Proceedings of the National Academy of Sciences **110**, 1611 (2013). 58, 59

[81] C. E. v. Seggern and R. J. Cotter, *Study of peptide–sugar non-covalent complexes by infrared atmospheric pressure matrix-assisted laser desorption/ionization*, Journal of Mass Spectrometry **39**, 736 (2004). 58

[82] Y. Li, B. Shrestha, and A. Vertes, *Atmospheric Pressure Molecular Imaging by Infrared MALDI Mass Spectrometry*, Analytical Chemistry **79**, 523 (2007). 58

[83] V. V. Laiko, N. I. Taranenko, V. D. Berkout, M. A. Yakshin, C. R. Prasad, H. S. Lee, and V. M. Doroshenko, *Desorption/ionization of biomolecules from aqueous solutions at atmospheric pressure using an infrared laser at $3\mu m$*, Journal of the American Society for Mass Spectrometry **13**, 354 (2002). 58

[84] P. Nemes and A. Vertes, *Laser ablation electrospray ionization for atmospheric pressure, in vivo, and imaging mass spectrometry*, Analytical Chemistry **79**, 8098 (2007). 58

[85] B. Shrestha, P. Nemes, J. Nazarian, Y. Hathout, E. P. Hoffman, and A. Vertes, *Direct analysis of lipids and small metabolites in mouse brain tissue by AP IR-MALDI and reactive LAESI mass spectrometry*, The Analyst **135**, 751 (2010). 58

[86] C. H. Stephens, B. Shrestha, H. R. Morris, M. E. Bier, P. M. Whitmore, and A. Vertes, *Minimally invasive monitoring of cellulose degradation by desorption electrospray ionization and laser ablation electrospray ionization mass spectrometry*, The Analyst **135**, 2434 (2010). 58

[87] P. Nemes, H. Huang, and A. Vertes, *Internal energy deposition and ion fragmentation in atmospheric-pressure mid-infrared laser ablation electrospray ionization*, Physical Chemistry Chemical Physics **14**, 2501 (2012). 58

[88] P. Nemes and A. Vertes, *Ambient mass spectrometry for in vivo local analysis and in situ molecular tissue imaging*, TrAC Trends in Analytical Chemistry **34**, 22 (2012). 58, 59

[89] D. S. Cornett, M. L. Reyzer, P. Chaurand, and R. M. Caprioli, *MALDI imaging mass spectrometry: molecular snapshots of biochemical systems*, Nature Methods **4**, 828 (2007). 59

[90] J. D. Watrous and P. C. Dorrestein, *Imaging mass spectrometry in microbiology*, Nature Reviews Microbiology **9**, 683 (2011). 59

[91] R. L. Caldwell and R. M. Caprioli, *Tissue profiling by mass spectrometry: a review of methodology and applications*, Molecular & Cellular Proteomics **4**, 394 (2005). 59

[92] G. Robichaud, J. A. Barry, K. P. Garrard, and D. C. Muddiman, *Infrared matrix-assisted laser desorption electrospray ionization (IR-MALDESI) imaging source coupled to a FT-ICR mass spectrometer*, Journal of The American Society for Mass Spectrometry **24**, 92 (2013). 59

[93] S. Steurer, C. Borkowski, S. Odinga, M. Buchholz, C. Koop, H. Huland, M. Becker, M. Witt, D. Trede, M. Omidi, O. Kraus, A. S. Bahar, A. S. Seddiqi, J. M. Singer, M. Kwiatkowski, M. Trusch, R. Simon, M. Wurlitzer, S. Minner, T. Schlomm, G. Sauter, and H. Schlüter, *MALDI mass spectrometric imaging based identification of clinically relevant signals in prostate cancer using large-scale tissue microarrays*, International Journal of Cancer **133**, 920 (2013). 60

[94] S. S. Iqbal, M. W. Mayo, J. G. Bruno, B. V. Bronk, C. A. Batt, and J. P. Chambers, *A review of molecular recognition technologies for detection of biological threat agents*, Biosensors and Bioelectronics **15**, 549 (2000). 61

[95] V. A. Petrenko and I. B. Sorokulova, *Detection of biological threats. A challenge for directed molecular evolution*, Journal of Microbiological Methods **58**, 147 (2004). 61

[96] R. Aggarwal, D. Kini, S. Sofat, S. R. Naik, and K. Krawczynski, *Duration of viraemia and faecal viral excretion in acute hepatitis E*, The Lancet **356**, 1081 (2000). 61

[97] H. Lee, J. Burczak, S. Muldoon, G. Leckie, M. Chernesky, J. Schachter, W. Andrews, and W. Stamm, *Diagnosis of Chlamydia trachomatis genitourinary infection in women by ligase chain reaction assay of urine*, The Lancet **345**, 213 (1995). 61

[98] A. Asselin and M. Zaitlin, *Characterization of a second protein associated with virions of tobacco mosaic virus*, Virology **91**, 173 (1978). 61

[99] A. Asselin and J. Grenier, *Detection of tobamoviruses from purified or crude extracts after agarose gel electrophoresis*, Canadian Journal of Plant Pathology **7**, 223 (1985). 61

[100] A. Stals, L. Baert, E. van Coillie, and M. Uyttendaele, *Extraction of foodborne viruses from food samples: A review*, International Journal of Food Microbiology **153**, 1 (2012). 61

[101] D. O'Toole, L. Palazzo, R. Arotçarena, A. Dancour, A. Aubert, P. Hammel, J. Amaris, and P. Ruszniewski, *Assessment of complications of EUS-guided fine-needle aspiration*, Gastrointestinal Endoscopy **53**, 470 (2001). 61, 81

[102] R. Winokur, B. Pua, B. Sullivan, and D. Madoff, *Percutaneous Lung Biopsy: Technique, Efficacy, and Complications*, Seminars in Interventional Radiology **30**, 121 (2013). 61, 81

[103] N. Hjortholm, E. Jaddini, K. Hałaburda, and E. Snarski, *Strategies of pain reduction during the bone marrow biopsy*, Annals of Hematology **92**, 145 (2013). 61

[104] A. J. Nemeth, *Faster Healing and Less Pain in Skin Biopsy Sites Treated With an Occlusive Dressing*, Archives of Dermatology **127**, 1679 (1991). 61, 81

[105] M. W. Berns, *A history of laser scissors (microbeams)*, in M. W. Berns and K. O. Greulich (eds.), *Methods Cell Biology, Laser Manipulation of Cells and Tissues*, vol. 82, 1–58, Academic Press (2007). 61

[106] M. Montag, K. van der Ven, C. Dorn, and H. van der Ven, *Outcome of laser-assisted polar body biopsy and aneuploidy testing*, Reproductive BioMedicine Online **9**, 425 (2004). 61

[107] S. Houlard, F. Perrotin, F. Fourquet, H. Marret, J. Lansac, and G. Body, *Risk factors for cervical stenosis after laser cone biopsy*, European Journal of Obstetrics & Gynecology and Reproductive Biology **104**, 144 (2002). 61

[108] G. Peretti, J. Cappiello, P. Nicolai, C. Smussi, and A. R. Antonelli, *Endoscopic Laser Excisional Biopsy for Selected Glottic Carcinomas*, The Laryngoscope **104**, 1276 (1994). 61, 62

[109] M. R. Emmert-Buck, R. F. Bonner, P. D. Smith, R. F. Chuaqui, Z. Zhuang, S. R. Goldstein, R. A. Weiss, and L. A. Liotta, *Laser Capture Microdissection*, Science **274**, 998 (1996). 61, 62

[110] G. I. Murray, *An overview of laser microdissection technologies*, Acta Histochemica **109**, 171 (2007). 62

[111] A. Vogel, V. Horneffer, K. Lorenz, N. Linz, G. Hüttman, and A. Gebert, *Principles of Laser Microdissection and Catapulting of Histologic Specimens and Live Cells*, in M. W. Berns and K. O. Greulich (eds.), *Methods Cell Biology, Laser Manipulation of Cells and Tissues*, vol. 82, 153–205, Academic Press (2007). 62

[112] I. Vilaseca-González, M. Bernal-Sprekelsen, J.-L. Blanch-Alejandro, and M. Moragas-Lluis, *Complications in transoral CO2 laser surgery for carcinoma of the larynx and hypopharynx*, Head & Neck **25**, 382 (2003). 62

[113] L. Ren, W. D. Robertson, R. Reimer, C. Heinze, C. Schneider, D. Eggert, P. Truschow, N.-O. Hansen, P. Kroetz, J. Zou, and R. J. D. Miller, *Towards instantaneous cellular level bio diagnosis: laser extraction and imaging of biological entities with conserved integrity and activity*, Nanotechnology **26**, e284001 (2015). 63, 70, 71, 72, 73, 74, 75, 76, 77, 107

[114] K. Franjic, *Studies of laser ablation of liquid water under conditions of impulsive heat deposition through vibrational excitations*, Ph.D. thesis, University of Toronto (2010). 63, 64

[115] J. Zou, Ph.D. thesis, University of Toronto, Canada (2015). 64, 107

[116] B. Letschert, G. Adam, D.-E. Lesemann, P. Willingmann, and C. Heinze, *Detection and differentiation of serologically cross-reacting tobamoviruses of economical importance by RT-PCR and RT-PCR-RFLP*, Journal of Virological Methods **106**, 1 (2002). 65

[117] G. V. Gooding and T. T. Hebert, *A simple technique for purification of tobacco mosaic virus in large quantities*, Phytopathology **57**, 1285 (1967). 65

[118] M. K. Brakke, *Density-gradient centrifugation*, in K. Maramorosch and H. Koprowski (eds.), *Methods in Virology*, vol. 2, 93–118, Academic Press, New York and NY (1967). 67

[119] *Yeast extract-peptone-dextrose growth medium (YEPD)*, Cold Spring Harbor Protocols **2010**, pdb.rec12161 (2010). 68

[120] R. Y. Tsien, *The green fluorescence protein*, Annual Review of Biochemistry **67**, 509 (1998). 71, 79

[121] E. C. Theil, *Ferritin: Structure, gene regulation, and cellular function in animals, plants and microorganisms*, Annual Review of Biochemistry **56**, 289 (1987). 78

[122] C. W. Cody, D. C. Prasher, W. M. Westler, F. G. Prendergast, and W. W. Ward, *Chemical structure of the hexapeptide chromophore of the Aequorea green-fluorescent protein*, Biochemistry **32**, 1212 (1993). 78

[123] D. A. Zacharias and R. Y. Tsien, *Molecular biology and mutation of green fluorescent protein*, in M. Chalfie and S. R. Kain (eds.), *Methods of Biochemical Analysis, Green Fluorescent Protein: Properties, Applications and Protocols*, vol. 47, 83–120, John Wiley & Sons, Inc. (2006). 78

[124] F. Yang, L. G. Moss, and G. N. Phillips, *The molecular structure of green fluorescent protein*, Nature Biotechnology **14**, 1246 (1996). 79

[125] G. N. Phillips, *Structure and dynamics of green fluorescent protein*, Current Opinion in Structural Biology **7**, 821 (1997). 79

[126] M. J. J. Moreau, I. Morin, and P. M. Schaeffer, *Quantitative determination of protein stability and ligand binding using a green fluorescent protein reporter system*, Molecular BioSystems **6**, 1285 (2010). 79

[127] R. N. Beachy and M. Zaitlin, *Characterization and in vitro translation of the RNAs from less-than-full-length, virus-related, nucleoprotein rods present in tobacco mosaic virus preparations*, Virology **81**, 160 (1977). 79, 80

[128] Y. F. Drygin, O. A. Bordunova, M. O. Gallyamov, and I. V. Yaminsky, *Atomic force microscopy examination of tobacco mosaic virus and virion RNA*, FEBS Letters **425**, 217 (1998). 79

[129] B. D. Harrison and T. M. A. Wilson, *Milestones in research on tobacco mosaic virus*, Philosophical Transactions of the Royal Society B: Biological Sciences **354**, 521 (1999). 80

[130] R. A. Erickson, *EUS-guided FNA*, Gastrointestinal Endoscopy **60**, 267 (2004). 82

[131] J. D. Warren, J. M. Schott, N. C. Fox, M. Thom, T. Revesz, J. L. Holton, F. Scaravilli, D. G. T. Thomas, G. T. Plant, P. Rudge, and M. N. Rossor, *Brain biopsy in dementia*, Brain **128**, 2016 (2005). 82

[132] A. Ruth, F. J. Schulmeyer, M. Roesch, C. Woertgen, and A. Brawanski, *Diagnostic and therapeutic value due to suspected diagnosis, long-term complications, and indication for sural nerve biopsy*, Clinical Neurology and Neurosurgery **107**, 214 (2005). 82

[133] P. Seeman and N. Seeman, *Alzheimer's disease: β-amyloid plaque formation in human brain*, Synapse **65**, 1289 (2011). 82

Publications

The following publications have been generated in the course of this dissertation.

Journal papers

- **L. Ren**, W. D. Robertson, R. Reimer, C. Heinze, C. Schneider, D. Eggert, P. Truschow, N.-O. Hansen, P. Kroetz, J. Zou, and R. J. D. Miller, *Towards instantaneous cellular level bio diagnosis: laser extraction and imaging of biological entities with conserved integrity and activity*. Nanotechnology **26**, e284001 (2015).

- S. J. Linke, A. Frings, **L. Ren**, A. Gomolka, U. Schumacher, R. Reimer, N.-O. Hansen, N. Jowett, G. Richard, and R. J. D. Miller, *A new technology for applanation free corneal trephination: the Picosecond Infrared Laser (PIRL)*. PLOS ONE **10**, e0120944 (2015).

- M. Kwiatkowski, M. Wurlitzer, M. Omide, **L. Ren**, S. Kruber, R. Nimer, W. D. Robertson, A. Horst, R. J. D. Miller, and H. Schlüter, *Ultrafast extraction of proteins from tissues using desorption by impulsive vibrational excitation*. Angewandte Chemie International Edition **54**, 285-288 (2015).

- S. J. Linke, **L. Ren**, A. Frings, J. Steinberg, W. Wöllmer, T. Katz, R. Reimer, N.-O. Hansen, N. Jowett, G. Richard, and R. J. D. Miller, *Perspektiven der laserassistierten Keratoplastik: Eine aktuelle Übersicht und erste experimentelle Erfahrungen mit dem Pikosekundeninfrarotlaser ($\lambda = 3~\mu m$)*. Der Ophthalmologe **111**, 523-530 (2014).

Conference talk

- **L. Ren**, R. Reimer, C. Heinze, C. Schneider, D. Eggert, P. Truschow, N.-O. Hansen, W. D. Robertson, and R. J. D. Miller, *Ultrafast desorption of intact proteins to viruses by impulsive vibrational excitation for rapid high throughput*

biodiagnosis. Pittsburgh Conference on Analytical Chemistry and Applied Spectroscopy (PittCon), abstract number 2510-6, New Orleans, March 2015.

Conference posters

- **L. Ren**, S. Linke, A. Frings, E. W. de Jong, M. Kwiatkowski, M. Wurlitzer, N.-O. Hansen, H. Schlüter, and R. J. D. Miller, *Ultrafast desorption by impulse vibrational excitation, ophtalmology and mass spectrometry*. Modern Concepts of Continuous Wave and Pulsed High Power Lasers (540 Wilhelm und Else Heraeus Seminar), Bad Honnef, July 2013.

- *Star Trek Laser-Chirurgie mit minimaler Narbenbildung und Präsizion auf Einzelzell-Niveau*. EU-Forschungsförderung in Hamburg, Europawoche Hamburg, April 2013.

- M. Hess, D. Hildebrandt, P. Krötz, F. Müller, K. Franjic, W. Wöllmer, **L. Ren**, M. Kammal, and R. J. D. Miller, *Picosecond infrared laser (PIRL) scalpel - a quantum jump towards trauma-free cutting in phonomicrosurgery?* European Laryngological Society Scientific Congress, Helsinki, June 2012.

Acknowledgement

Over the last three and a half years of doctoral work, I am most grateful for the guidance from my supervisor Prof. R. J. Dwayne Miller and my co-supervisor Prof. Franz X. Kärtner. Your supervision and precious advice navigated me all the way through the voyage in the fantastic world of cutting-edge science.

I would also like to give my sincerely thanks to Dr. Nils-Owe Hansen, Kresmir Franjic PhD, Dr. Dongfang Zhang, Dr. Stephanie Manz, Wesley Robertson PhD, Dr. Günther Kassier, and all other postdoctoral scientists, currently and previously working in the Miller Group. I benefitted greatly through the doctoral work from the inspiring discussions and the technical support from you.

Appreciation and acknowledgment are due to the collaborators on the UKE campus. Prof. Hartmut Schlüter and his group members provided significant support for the work on mass spectrometry. I really enjoyed the work on ophthalmologic applications with Dr. Stephan Linke, Dr. Andreas Frings and Amadeus Gomolka. I felt very lucky to have the opportunity to work with Dr. Rudolph Reimer, Dr. Dennis Eggert, Carola Schneider and Pavel Truschow, who provided substantial technical support in microscopy imaging and biochemical analyses. Dr. Wolfgang Wöllmer and Dr. Nathan Jowett facilitated a platform convenient for interdisciplinary collaborations on the UKE campus.

I would like to give a hearty Thank You to Dr. Cornelia Heinze, who kindly supported the work using TMV.

Prof. Nils Huse and Prof. Arwen Pearson, I gained further scientific understanding and insight through the interesting discussions with you. Thanks so much. Prof. Ludwig Mathey and Prof. Henning Moritz, I sincerely appreciate your efforts as members of the committee for my disputation.

Carsten Meklenburg provided sound support in mechanics. Jing Zou at the University of Toronto oftentimes lent a hand in scientific discussion and technical support. I am grateful for all types of help from the whole Miller group.

Genuine appreciation is also delivered to Nadja Badenheuer, Christine Berbe, Anja Bleidorn, Dr. Sonia Utermann, Tania Hartin, Ulrike Krieger, Dr. Ralf Köhn, Gisbert Mantei, Dr. Diana Hoppe, and all the other administrative personnel, whose work in the background upheld the research.

My doctoral fellows brought so much fun and joy in both science and free time. Dr. Anne-Laure Calendron, Alessandra Picchiotti, Peter Krötz, Lourie Pieterse, Nele Müller, Stephanie Besztejan, Jan Malte Slowik, Clemens Weninger, Martina Pola, Ara choudhuri, Julian Hirscht, Eliza and Albert Casandruc, I was